The Pennsylvania State University

The Graduate School

OPTICAL CHARACTERIZATION OF RELIABILITY IN CAPACITOR MATERIALS

A Thesis in

Materials Science and Engineering

by

Michael David Biegalski

Submitted in Partial Fulfillment
of the Requirements
for the Degree of

Master of Science

December 2001

I grant The Pennsylvania State University the nonexclusive right to use this work for the University's own purposes and to make single copies of the work available to the public on a not-for-profit basis if copies are not otherwise available.

Michael David Biegalski

We approve the thesis of Michael David Biegalski.

Date of Signature

Susan Trolier-McKinstry Associate Professor of Ceramic Science and Engineering Thesis Advisor	9-19-01
Clive A. Randall Professor of Materials Science and Engineering	17 Sept 01
William B. White Professor of Geosciences	Sept 21 2001
Long-Qing Chen Associate Professor of Materials Science and Engineering Coordinator of Graduate Programming, Department of Materials Science and Engineering.	9-19-01

ABSTRACT

One of the important failure mechanisms in multilayer capacitors (MLCs) is degradation of the dielectric material under dc electric fields. The failure of $BaTiO_3$ based MLCs have been traced to the electromigration of oxygen vacancies. MLCs with Ni electrodes are processed in a reducing atmosphere; this increases the oxygen vacancy concentration and decreases the reliability. To investigate this phenomenon, spectroscopic ellipsometry (SE) was used. SE is a nondestructive tool that can monitor the accumulation of damage in $BaTiO_3$ by measuring the changes in the optical properties of the material.

In this study, samples of $BaTiO_3$ and $SrTiO_3$ were examined in the reduced and oxidized states, to determine their reference optical properties. With the reference optical data, the sensitivity to layers of reduced material was calculated. From the modeling it was found that SE could detect a 4Å layer of reduced $BaTiO_3$ on oxidized $BaTiO_3$. Similarly SE could detect a 8Å layer of reduced iron doped $SrTiO_3$. When an error function was used to describe a concentration gradient of reduced material on an oxidized bulk, it was found that SE was able to detect concentration gradients. Concentration gradients with an average diffusion depth ($\sqrt{Dt}$) as low as 8Å for $BaTiO_3$ and 12Å for iron doped $SrTiO_3$, for ideally smooth surfaces, were resolvable.

The changes during DC electric field induced degradation of $BaTiO_3$ and Iron doped $SrTiO_3$ were also investigated experimentally. The changes due to degradation

were found to be detectable by ellipsometry in the optical frequency range. However, detection is complicated by the presence of surface roughness and by damage associated with electrode removal.

TABLE OF CONTENTS

LIST OF FIGURES

LIST OF TABLES

ACKNOWLEDGMENTS

I would like to first thank my advisor, Dr. Susan Trolier McKinstry. She has given me priceless guidance and shown immense patience though the course of this work and was always there to answer my questions. I wold also like to thank Dr. Randall for his guidance in the early parts of this work and for his time. I also need to thank Dr. White for serving on my committee.

I need to thank my friends and co-workers. They have been quick to offer help and advice, even when not needed. They have made this work much more enjoyable and have proved to be invaluable. I would also like to thank my whole family, especially my parents. I appreciate the help and support and never could have made it this far without it.

Finally I would like to thank the Center for Dielectric studies for their generous support of this project and input.

Chapter 1

INTRODUCTION

Ferroelectric materials based on the perovskite structure are used in industry for devices such as multilayer capacitors (MLC), piezoelectric transducers and more recently in non-volatile memory devices. A major problem with these devices is the reliability of the materials under exposure to dc electric fields. The failure mode of $BaTiO_3$ based MLC capacitors has been traced to the electromigration of oxygen vacancies.[1-13] When Ni or Cu electrodes are used, instead of expensive noble metal electrodes, the MLCs must be processed in a reducing atmosphere to prevent oxidation of the Ni or Cu. This increases the number of oxygen vacancies in the material, increasing the electrical conductivity and decreasing the reliability on long term dc field exposure. While dopants to minimize this problem have been developed empirically for $BaTiO_3$, a better understanding of the degradation mechanism may enable further increase in their reliability. This is increasingly important since many perovskite materials are being integrated into miniaturized components and thin films where field levels can be high. An insight into the increase in reliability of $BaTiO_3$ will have a far-reaching effect on the lifetimes of many perovskite microelectronic devices.

1.1 Introduction to Problem

Long term degradation in perovskite oxide ferroelectric materials under dc electric field is generally regarded as an electromigration phenomenon. [1-13] The only carriers that are considered to be mobile in the perovskite material at nominal operating temperatures are electrons, holes, and oxygen vacancies [$V_O^{\bullet\bullet}$]. The most widely accepted model of dielectric degradation in barium titanate entails diffusion of oxygen vacancies. These oxygen vacancies have a positive charge and, as a result will migrate to the cathode. As time progresses, the oxygen vacancies build up at the cathode. The exact manner in which charge is injected into the material is still debated. The build up of these oxygen vacancies causes an increase in electron concentration in the cathode region. As a result, material near the cathode becomes n-type. The corresponding deficiency of oxygen vacancies at the anode makes this region p-type. This concentrates the field in the insulating region. Failure occurs when the field in the remaining insulating regions grows large enough to cause the material to breakdown, or when the resistance is lowered to unacceptable levels.

When a field is applied across the barium titanate sample, the material near the cathode changes from tan to blue.[1] In iron doped strontium titanate the cathode area changes from red-brown to clear and the area near the anode becomes dark brown.[2] These colored areas also exhibit different light absorption profiles. The reason for the coloration is attributed to different ionization states of the transition metals. [1,2] This allows for the optical examination of the degradation.

In this work, Spectroscopic Ellipsometry (SE) was used to study degradation in $BaTiO_3$ and iron doped $SrTiO_3$. Spectroscopic ellipsometry is a light reflection tool that enables the optical properties of samples to be depth profiled on an angstrom scale. It also allows analysis of a material without the use of probes that induce localized changes in the material. Fundamentally, SE measures the relative change in the polarization state of light reflected from a material as a function of wavelength. Optical measurements will be used to follow the accumulation of damage in $BaTiO_3$ and iron doped $SrTiO_3$ during the degradation process.

1.2 Thesis Objectives

In this thesis spectroscopic ellipsometry was used to examine the changes in $BaTiO_3$ and iron doped $SrTiO_3$ during degradation. Spectroscopic ellipsometry was utilized because of its ability to depth profile on an angstrom scale and its ability to be utilized *in-situ* in real time. The first objective was to determine the reference dielectric properties for oxidized and reduced $BaTiO_3$ and iron doped $SrTiO_3$. The second objective was to use this reference data to model field induced changes in $BaTiO_3$ and iron doped $SrTiO_3$. Models were constructed to determine the sensitivity of spectroscopic ellipsometry to a thin surface layer of degraded material. The final objective is to follow degradation in bulk materials under dc electric fields.

Chapter 2

BACKGROUND

Barium titanate ($BaTiO_3$) is a ferroelectric ceramic oxide that is useful in capacitor applications. Below 1460°C $BaTiO_3$ barium titanate adopts the perovskite crystal structure.[3] This structure is of the form ABO_3 and can be viewed as a simple cubic structure of BO_6 octahedra, with a barium atom in the interstitial site (*Figure. 2–1*).[3] This

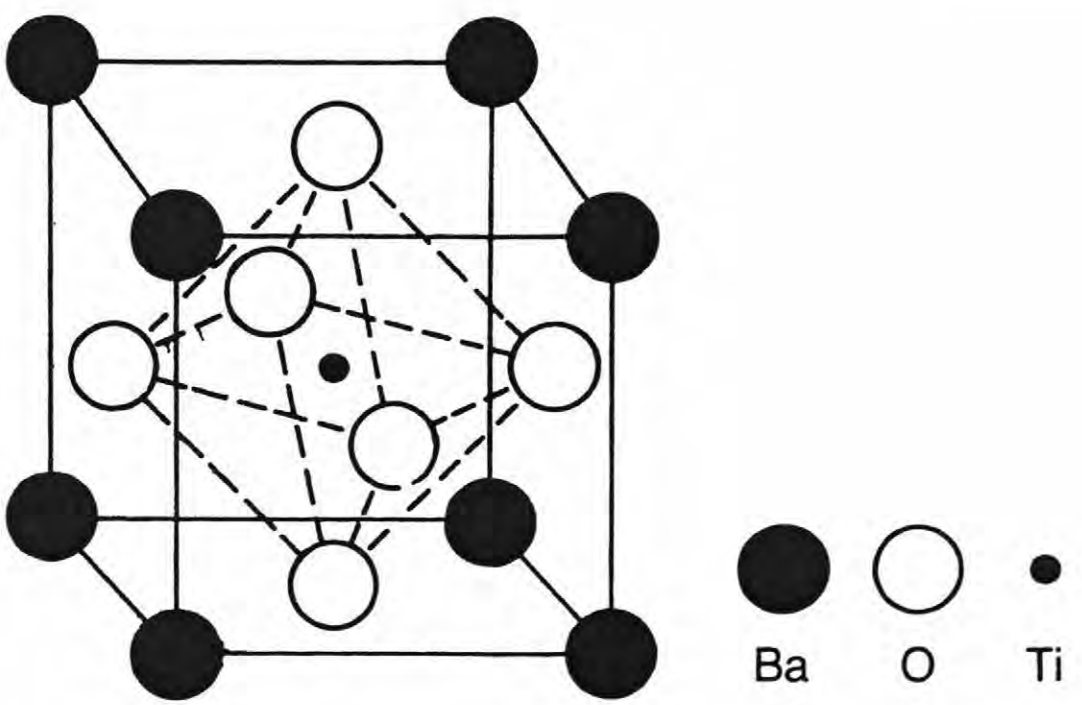

Figure 2–1: Schematic of perovskite structure of $BaTiO_3$.[3]

structure can also be viewed as a Ti ion sitting in the center of a cubic lattice with Ba ions on the corners of the cube and oxygen ions on each face.[3]

For the pure material at room temperature, the structure distorts into a tetragonal structure, with the Ti ion undergoing a displacement along one of the <100> directions, producing an electrical dipole that can be aligned under an applied electric field. Above 130°C the material has the cubic prototype structure. Strontium titanate ($SrTiO_3$) also has the perovskite structure. However, it is cubic down to room temperature.[3]

2.1 Defect Reactions

$BaTiO_3$ has a large ionic component to its bonding. Because of this bonding, most defects will be ionic.[3] The literature describing the point defect chemistry of $BaTiO_3$ is based mainly on measurements of electrical conduction as a function of oxygen partial pressure. The work is summarized in this section, using the defect notation of Kroger and Vink.[25]

The intrinsic reaction and equilibrium constant are as follows: nil is the standard state, k is Boltzmann's constant, T is the temperature, K_i is the equilibrium constant for equation *i* and the band gap is E_g (approximately 3.5eV):[26,28]

$$nil \Leftrightarrow e^{'} + h^{\circ} \qquad (2.1)$$

$$K_i = n \cdot p = K_0 \exp\left(-\frac{E_g}{kT}\right) \qquad (2.2)$$

Another primary defect reaction is the Schottky defect:[4]

$$nil \Leftrightarrow 3V_O^{\circ\circ} + V_{Ba}^{''} + V_{Ti}^{''''} \quad (2.3)$$

$$K_3 = \left[V_O^{\circ\circ}\right]^3 \left[V_{Ba}^{''}\right]\left[V_{Ti}^{''''}\right] \quad (2.4)$$

When oxygen is removed from the lattice, oxygen vacancies are created: [4]

$$O_O^X \Leftrightarrow \frac{1}{2} O_2 + V_O^{\circ\circ} + 2e' \quad (2.5)$$

$$K_5 = n^2 \left[V_O^{\circ\circ}\right] P_{O_2}^{\frac{1}{2}} \quad (2.6)$$

If oxygen is absorbed onto the lattice, cation vacancies are formed: [4]

$$\frac{3}{2} O_2 \Leftrightarrow 3O_O^X + V_{Ba}^{''} + V_{Ti}^{''''} + 6h^{\circ} \quad (2.7)$$

$$K_7 = p^6 \left[V_{Ba}^{''}\right]\left[V_{Ti}^{''''}\right] P_{O_2}^{-\frac{3}{2}} \quad (2.8)$$

Due to the constraints of stoichiometry, the concentration of barium vacancies and concentration of titanium vacancies must be equal. However, if the oxygen absorption is accommodated by vacancy annihilation, equations 2.7 and 2.8 become: [4]

$$V_O^{\circ\circ} + \frac{1}{2} O_2 \Leftrightarrow O_O^X + 2h^{\circ} \quad (2.9)$$

$$K_9 = P_{O_2}^{-\frac{1}{2}} \left[V_O^{\circ\circ}\right]^{-1} p^2 \quad (2.10)$$

Because the perovskite lattice is densely packed, interstitial point defects are not likely. The electroneutrality condition then becomes:[26]

$$n + 2\left[V_{Ba}^{''}\right] + 4\left[V_{Ti}^{''''}\right] \Leftrightarrow p + 2\left[V_{O}^{\circ\circ}\right] \qquad (2.11)$$

The defect chemistry is dependent on the oxygen partial pressure. This is often treated by separating the data into different regions. The dominant defects in the lower P_{O_2} region are oxygen vacancies. Under extremely reducing conditions, the oxygen vacancies are compensated by electrons. The electroneutrality condition in this regime is:[2]

$$n = 2\left[V_{O}^{\circ\circ}\right] \qquad (2.12)$$

The defect concentration as a function of P_{O_2} can be determined by combining equations 2.1 through 2.11.[4]

$$n = 2\left[V_{O}^{\circ\circ}\right] = \left(2K_5\right)^{\frac{1}{3}} P_{O_2}^{-\frac{1}{6}} \qquad (2.13)$$

$$p = K_1\left(2K_5\right)^{-\frac{1}{3}} P_{O_2}^{\frac{1}{6}} \qquad (2.14)$$

$$\left[V_{Ba}^{''}\right] = \left[V_{Ti}^{''''}\right] = \left(2K_3\right)^{\frac{1}{2}} 2\left(K_5\right)^{-\frac{1}{2}} P_{O_2}^{\frac{1}{4}} \qquad (2.15)$$

Thus, increasing P_{O_2} causes the concentration of electrons and oxygen vacancies to decrease. On the other hand, the concentration of holes and cation vacancies increase

with increasing P_{O_2}. It can be seen in *Figure 2–2* the conductivity shows the 1/6 dependence on P_{O_2} for the highly reducing condition. This occurs because the electronic defects dominate the electrical conductivity.

Under more moderate reducing conditions, electronic defects do not dominate and ionic defects must be take into account. [14] Within this region [$V_O^{\bullet\bullet}$] is fixed through various defects. The exact model for the way in which the oxygen vacancies are accommodated has been explained with several models. One model assumes the cation sublattice is fully stoichiometric and the ionic defects are created though Schottky defects. With this defect, the electroneutrality condition becomes:[14]

$$\left[V_O^{\circ\circ}\right] = \left[V_{Ba}''\right] + 2\left[V_{Ti}''''\right] \qquad (2.16)$$

With this electroneutrality condition, the dependence of the electronic carries on oxygen partial pressure can be determined. [14]

$$n = \left(K_5\right)^{\frac{1}{2}}\left(9K_3\right)^{-\frac{1}{10}} P_{O_2}^{-\frac{1}{4}} \qquad (2.17)$$

$$p = \left(K_9\right)^{-\frac{1}{2}}\left(9K_3\right)^{\frac{1}{5}} P_{O_2}^{\frac{1}{4}} \qquad (2.18)$$

Another model suggests that there is inherent non-stoichiometry. With this condition the [$V_O^{\bullet\bullet}$] is fixed through the cation vacancies as defined by equation 2.19:[15]

$$\left[V_O^{\circ\circ}\right] = \left[V_{Ba}''\right] = \Delta \text{ (Constant)} \qquad (2.19)$$

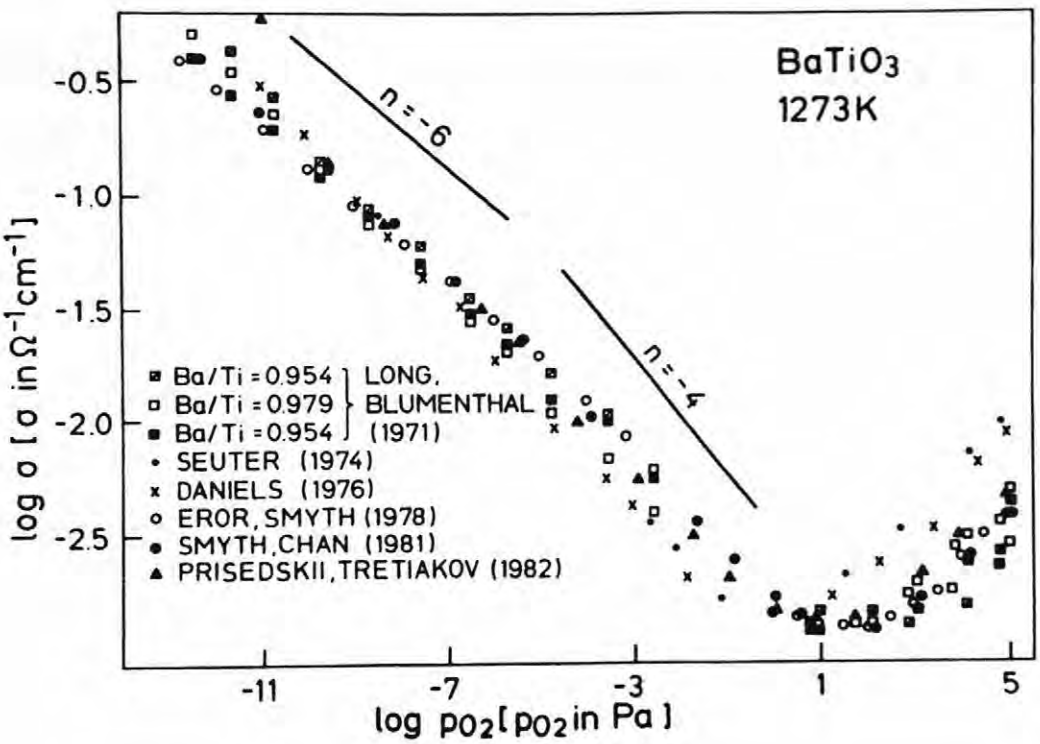

A

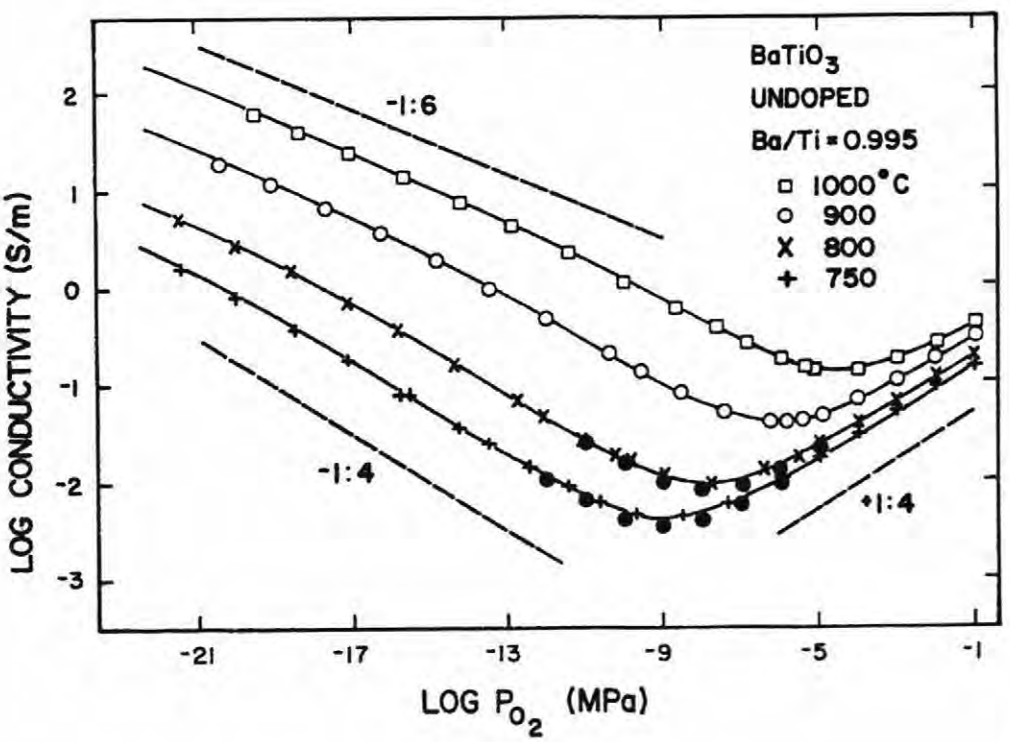

B

Figure 2–2: Conductivity as a function of oxygen partial pressure for barium titanate. (A) Data from multiple sources demonstrating the different dependence of the slope on oxygen partial pressure. n is of the form 1/n. (B) Conductivity as a function of oxygen partial pressure for various temperatures.

Incorporation equations 2.3-2.9 and equation 2.19, the dependence of the conductivity on the oxygen partial pressure can be determined. [15]

$$n = (K_5)^{-\frac{1}{2}} \Delta^{-\frac{1}{2}} P_{O_2}^{-\frac{1}{4}} \quad (2.20)$$

$$p = (K_9)^{\frac{1}{2}} \Delta^{\frac{1}{2}} P_{O_2}^{\frac{1}{4}} \quad (2.21)$$

Acceptor type defects $[A']$ from impurities or dopants can also be the predominant defects in $BaTiO_3$.[16] In these cases, the acceptor concentration will fix the oxygen vacancy concentration, as described by the electroneutrality condition: [17]

$$2[V_O^{\circ\circ}] = [A'] \quad (2.22)$$

This leads to the following dependence on oxygen partial pressure. [14]

$$n = (K_5)^{\frac{1}{2}} \left[\tfrac{1}{2} A'\right]^{-\frac{1}{2}} P_{O_2}^{-\frac{1}{4}} \quad (2.23)$$

$$p = (K_9)^{\frac{1}{2}} \left[\tfrac{1}{2} A'\right]^{\frac{1}{2}} P_{O_2}^{\frac{1}{4}} \quad (2.24)$$

All of these models describe the 1/4 dependence on the Po_2 as seen in *Figure 2–2*. It is possible that all these mechanisms are present and contribute to the Po_2 dependence. [17]

It is important to note that these models are only applicable to high temperatures. At lower temperatures, the Schottky defects and metal vacancies form very slowly and thus are fixed once the material is cooled to lower temperatures. [17] Another important

aspect of these models is that they show that there is an intrinsic oxygen vacancy concentration in the material after being exposed to high temperatures. This is due either to acceptors, or to frozen in metal vacancies. [17]

Adding iron or other acceptors to the ABO_3 perovskite causes an increase in the oxygen vacancy concentration, assuming Fe acts an acceptor, as described by: [5]

$$Fe_2O_3 \Leftrightarrow 2Fe'_{Ti} + 3O_O^X + V_O^{\circ\circ} \qquad (2.25)$$

$$K_{25} = \left[Fe'_{Ti}\right]^2 \left[V_O^{\circ\circ}\right] \qquad (2.26)$$

Omitting Ti vacancies the electroneutrality condition is: [5]

$$2\left[V_O^{\circ\circ}\right] + p = \left[Fe'_{Ti}\right] + n \qquad (2.27)$$

Through combining equations 2.5, 2.6, 2.25 through 2.27, the equations for electronically compensated oxygen absorption can be reached: [5]

$$n - p = 2\left[V_O^{\circ\circ}\right] - \left(\frac{K_{25}}{\left[V_O^{\circ\circ}\right]}\right)^{\frac{1}{2}} \qquad (2.28)$$

$$np = \left(K_5 K_9\right)^{1/2} \qquad (2.29)$$

According to these equations if [$V_o^{\bullet\bullet}$] is very large, n will be large and p will be small. Conversely, in regions where [$V_o^{\bullet\bullet}$] is very small, n is also very small and p is large. [5]

2.2 Electrical Degradation

Mobile ionic species are an important part of the conduction in barium titanate. These species are especially important in the time dependent conductivity of the material, otherwise referred to as electrical degradation. [1,4,6, 7,10,11,24]

Glower and Henkman studied charge transport mechanisms in barium titanate single crystals and ceramics using an oxygen concentration cell. They found that pure single crystals exhibited electronic conduction from 100 to 535°C. Single crystals doped with 0.1% iron showed electronic conduction at 600°C and ionic conduction at 100°C. The ceramic samples were found to be predominantly ionic conductors from 100 to 300°C, but above 500°C they were primarily an electronic conductor.[6]

Lehovic and Shrine investigated degradation in calcium zirconate doped barium titanate. They examined the leakage current and potential distributions as a function of time. The leakage current was found to go through an initial rise, followed by a drop in current, followed by a renewed rise in current as time progressed *(Figure 2–3)*. The final stage is associated with the degradation of the sample. The single crystal samples showed much smaller time-dependence in the leakage current for comparable fields. The potential distribution was also examined by probing the surface of the sample between the electrodes (). They found that as time progressed the voltage drop was higher in the middle of the sample accompanied by a region near the electrodes showing a smaller voltage drop. This tendency was exacerbated with increasing time under field, until there was no voltage drop at the cathode and only a small drop near the anode. They recognized that these potential distribution changes have

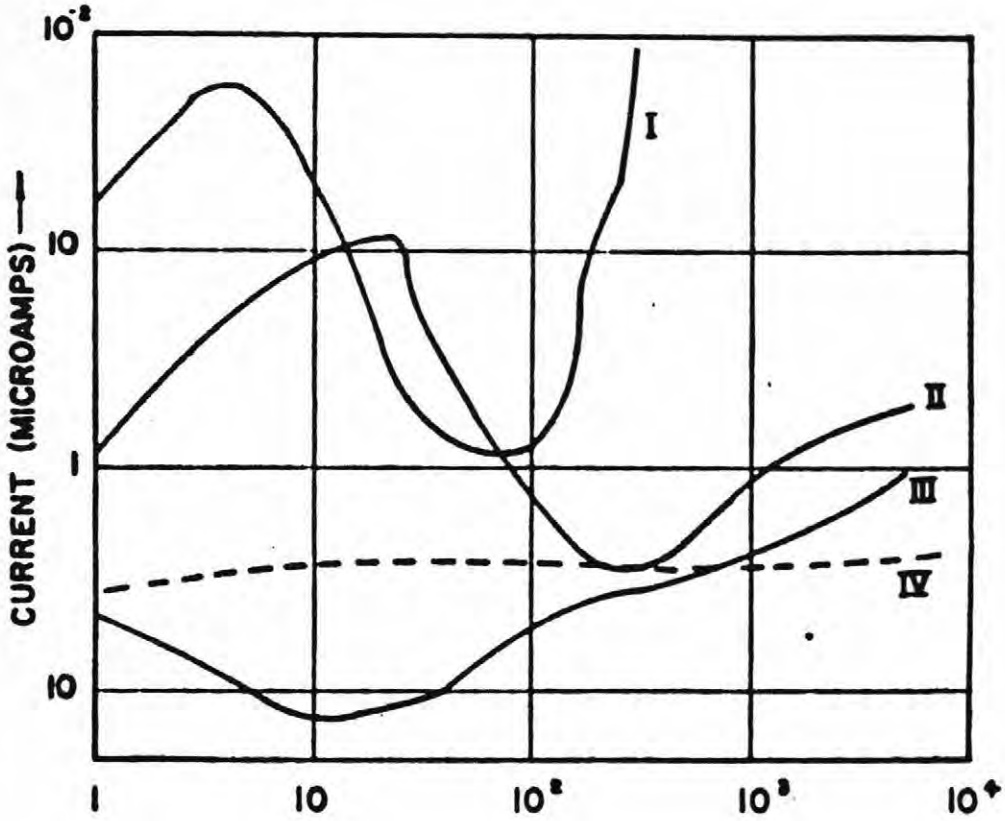

Figure 2–3: Leakage current of $BaTiO_3$ at 300°C.[1]

I: Polycrystalline ceramic under 6000 V/cm.

II: Polycrystalline ceramic under 4000 V/cm.

III: Polycrystalline ceramic under 2000 V/cm.

IV: Single crystal under 6000 V/cm.

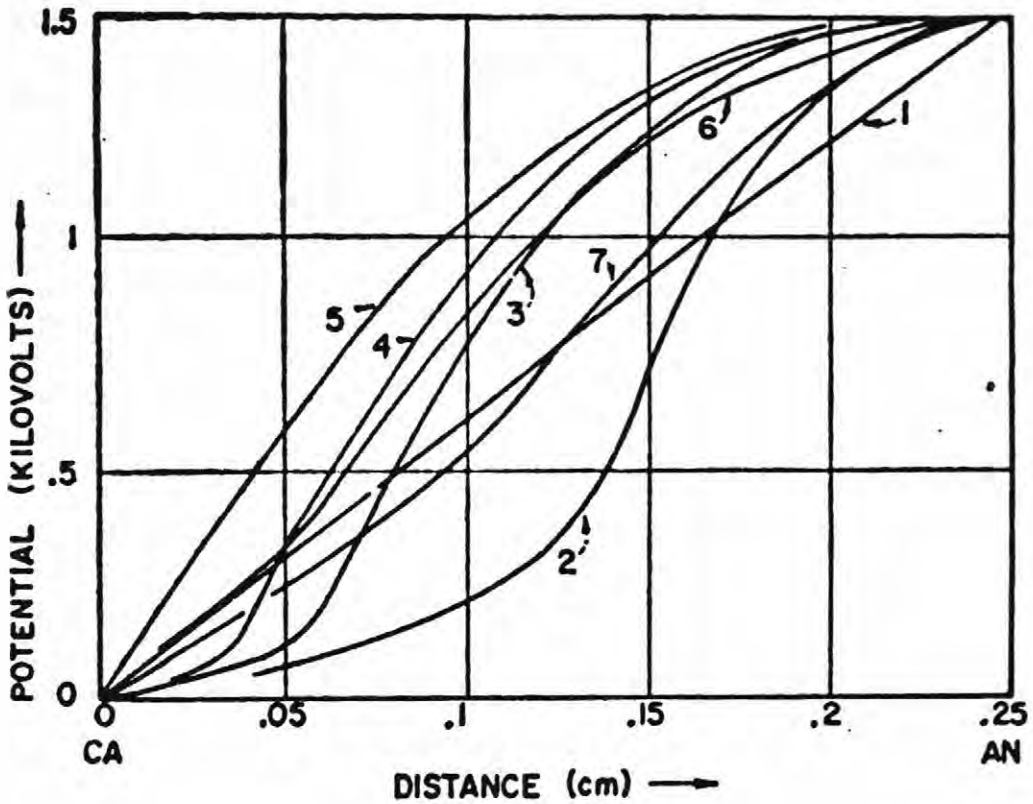

Figure 2–4: Potential distributions in polycrystalline $BaTiO_3$ tested at 300°C and 6000V/cm at various times where CA is the cathode and AN is the anode. (1) 0, (2) 14, (3) 52, (4) 79, (5) 117, (6) 135, and (7) 195 min.[1]

two limiting cases. If the anion vacancy concentration is homogeneous, the different potential distributions are a result of the space charge limited current. However, if there is no space charge, the potential distribution must be attributed to oxygen vacancy migration because these are the only mobile species at low temperatures. Lehovic and Shrine concluded that electron injection and a slower process, like oxygen vacancy

diffusion, were important part of the initial current rise.[1] It is important to note that the initial current rise was not found for the single crystals and was not found by other researchers. Consequently, there is some question of its origin.

Several investigators have studied the role of $V_O^{\bullet\bullet}$ in degradation. Schaffrin found that a completely degraded sample could be recovered by heating above 750°C in air.[7] He also found that the concentration of oxygen vacancies was directly related to the conduction in the sample. Buessem was one of the first to show that increasing the anion vacancy concentration increases conduction in the samples and expedited degradation.[8,9]

To study degradation in barium titanate, Gotto and Kachi observed the distribution of the electric field using the Kerr effect with a resolution of 0.1mm.[11] They showed that immediately after an electric field was applied, the distribution of field was homogeneous. Over time, the field at the anode became much higher, while at the cathode the field was reduced (*Figure 2–5)*. Using Poisson's equation, the space charge density at various times was determined (*Figure 2–6).* A negative space charge was observed to form near the anode and moved toward the cathode with time. Gotta and grain boundaries were a barrier to the $V_O^{\bullet\bullet}$ migration and served as the rate-limiting step Kachi theorized these results were due to injection of electrons and holes at the electrodes, and migration of anion vacancies in the bulk.[11] Triebwasser performed similar experiments, but showed that the field drops at the cathode was much higher than the field drop at the anode. Triebwasser suggested that these are the result of space charge surface layers.[11]

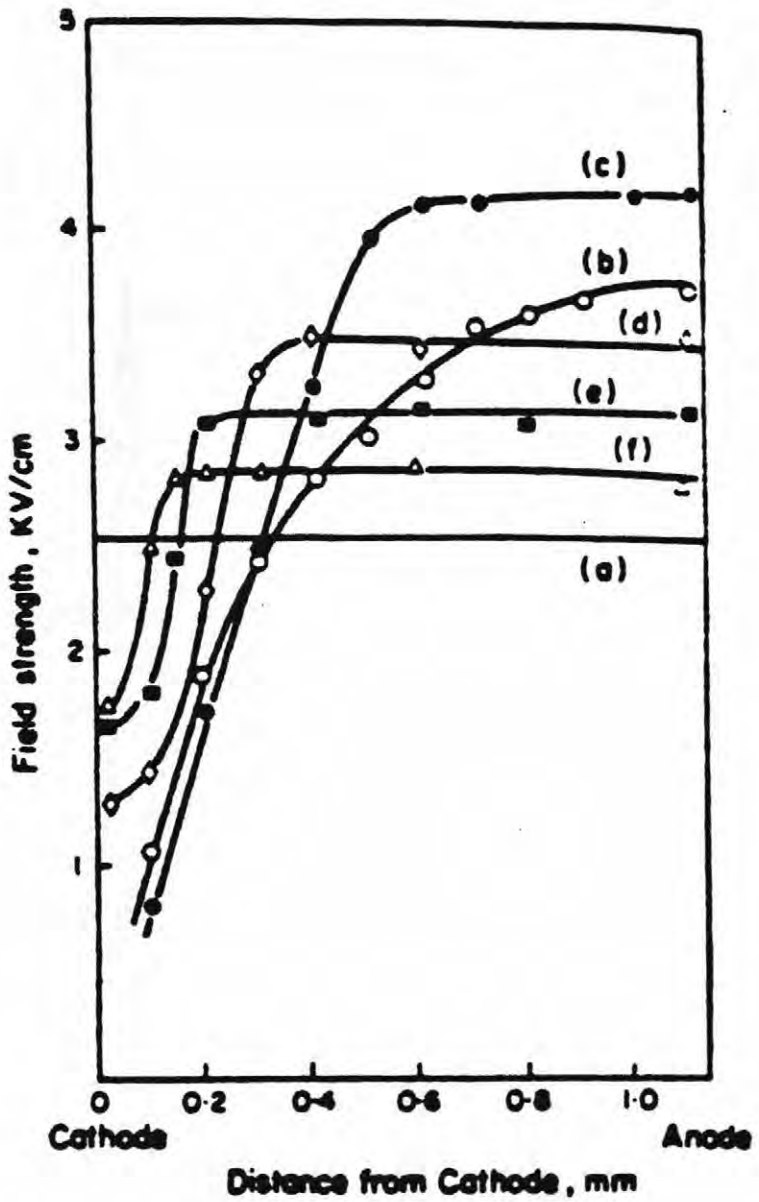

Figure 2–5: Electric field as a function of distance from the cathode at various times with an applied field of 2.7 kV/cm at 85°C (a) 10 sec., (b) 1.5hrs, (c) 7.5hrs, (d) 10hrs, (e) 18hrs, and (f) 24hrs.[10]

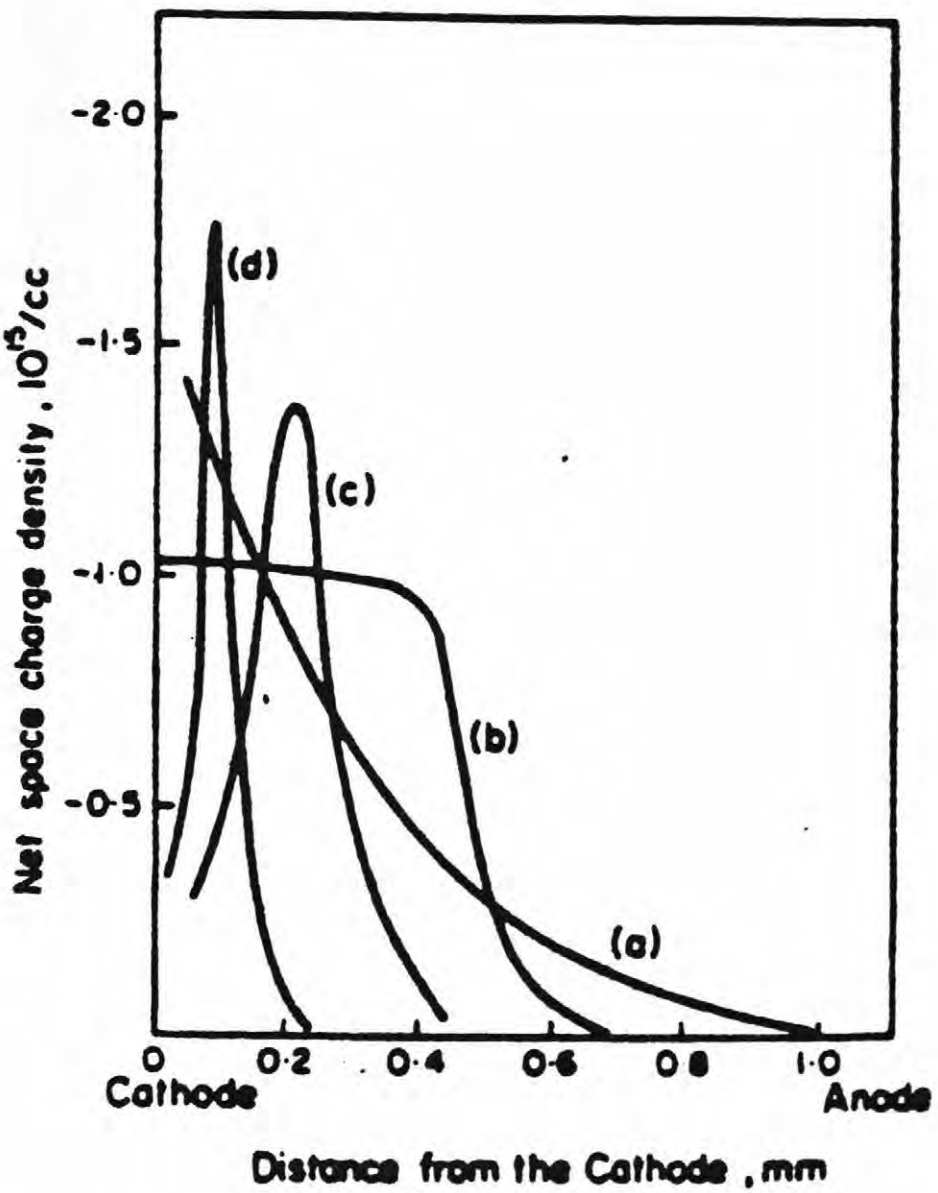

Figure 2–6: Calculated net space charge distribution, in ceramic $BaTiO_3$, for various times under a dc electric field of 2.7 kV/cm at 85°C. (a) 1.5hrs, (b) 7.5hrs, (c) 10hrs and (d) 24hrs times with an applied field of 2.7 kV/cm at 85°C. [10]

Waser et al. found that "there is a significant and unequivocal correlation between the $V_O^{\circ\circ}$ concentration and degradation" in titanate perovskites.[2] This was extracted from a comparison of the degradation rates of Al and La doped $SrTiO_3$ (*Figure 2–7)*. The acceptor-doped titanates are compensated by oxygen vacancies, while the donor doped titanates are compensated by cation vacancies. Al is an acceptor on the B site and the La acts as a donor on the A site. Rapid degradation in the Al doped samples, as compared to the La doped samples, show that the oxygen vacancies are an important part of the degradation.[2]

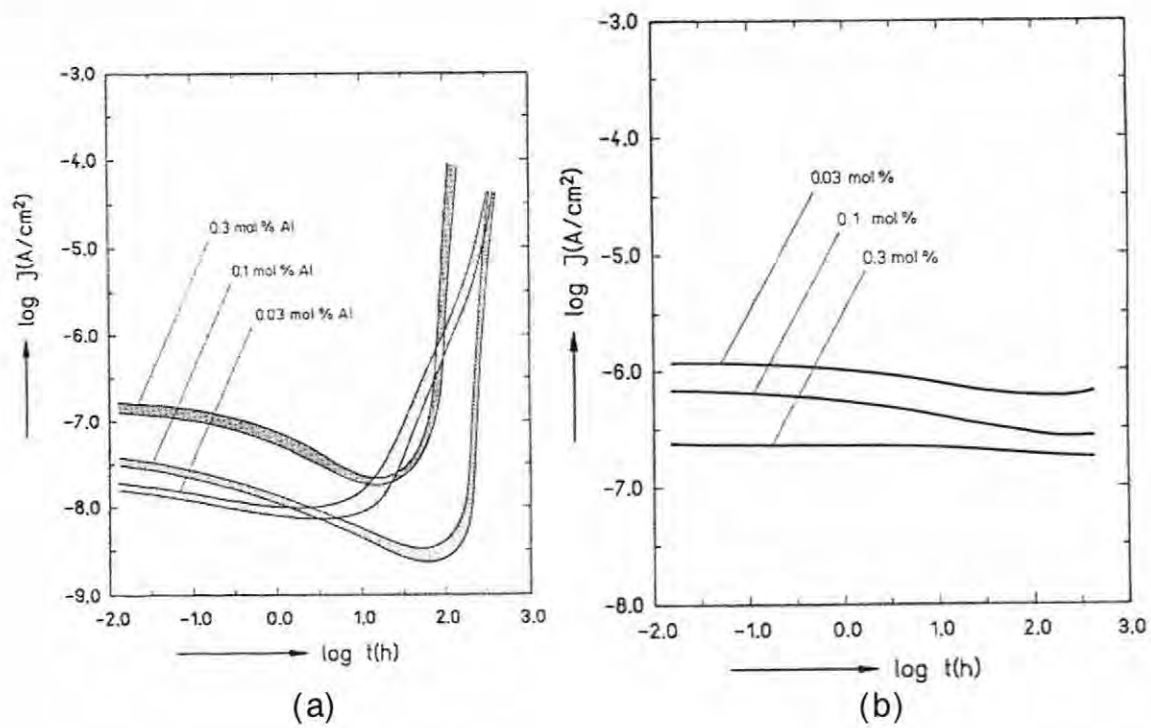

Figure 2–7: Current density, J vs. time, t, at a temperature of 543K and an electric field of 2.0kV/cm for (A) Al and (B) La doped $SrTiO_3$ ceramic disks.[2]

Waser et al. suggests a reduction model with electromigration of $V_O^{\cdot\cdot}$ as the essential mechanism for the degradation. In the reduction model, the $V_O^{\cdot\cdot}$ migrate towards the cathode, depleting the $V_O^{\cdot\cdot}$ concentration at the anode and increasing the $V_O^{\cdot\cdot}$ concentration at the cathode. This ionic demixing causes the concentration of electronic defects to increase. This theory is supported by the fact that the time for degradation (as defined by the point of a rapid increase in the leakage current) is proportional to the thickness of the sample. They also found that in ceramic samples the for degradation in ceramics. [2]

Baiatu performed computer simulations of Waser's degradation data. The reduction model was found to fit the data if the electrodes were blocking or at least partially blocking, meaning they did not allow gas to penetrate the electrode. This model used a finite difference algorithm and was able to reproduce the current-time characteristics of dc degradation assuming the degradation model suggested by Waser.[13]

Benguigui also examined conduction and potential distribution in barium titanate (*Figure 2–8*). At low voltage, the samples were ohmic and the potential was evenly distributed. With increasing voltage, the leakage current increased. At higher leakage, the current was not proportional to the voltage but increased as V^2 or V^3 at even higher voltages. The V^2 and V^3 region had separate voltage distributions. The V^2 region showed the deviation from homogeneous voltage distribution, it shows comparatively faster voltage drop near the anode (*Figure 2–8*B). Benguigui suggested that region was due to a net negative charge in the sample. As the voltage was increased, the V^3 region is reached. This region has a voltage distribution that has concave up and down regions (*Figure*

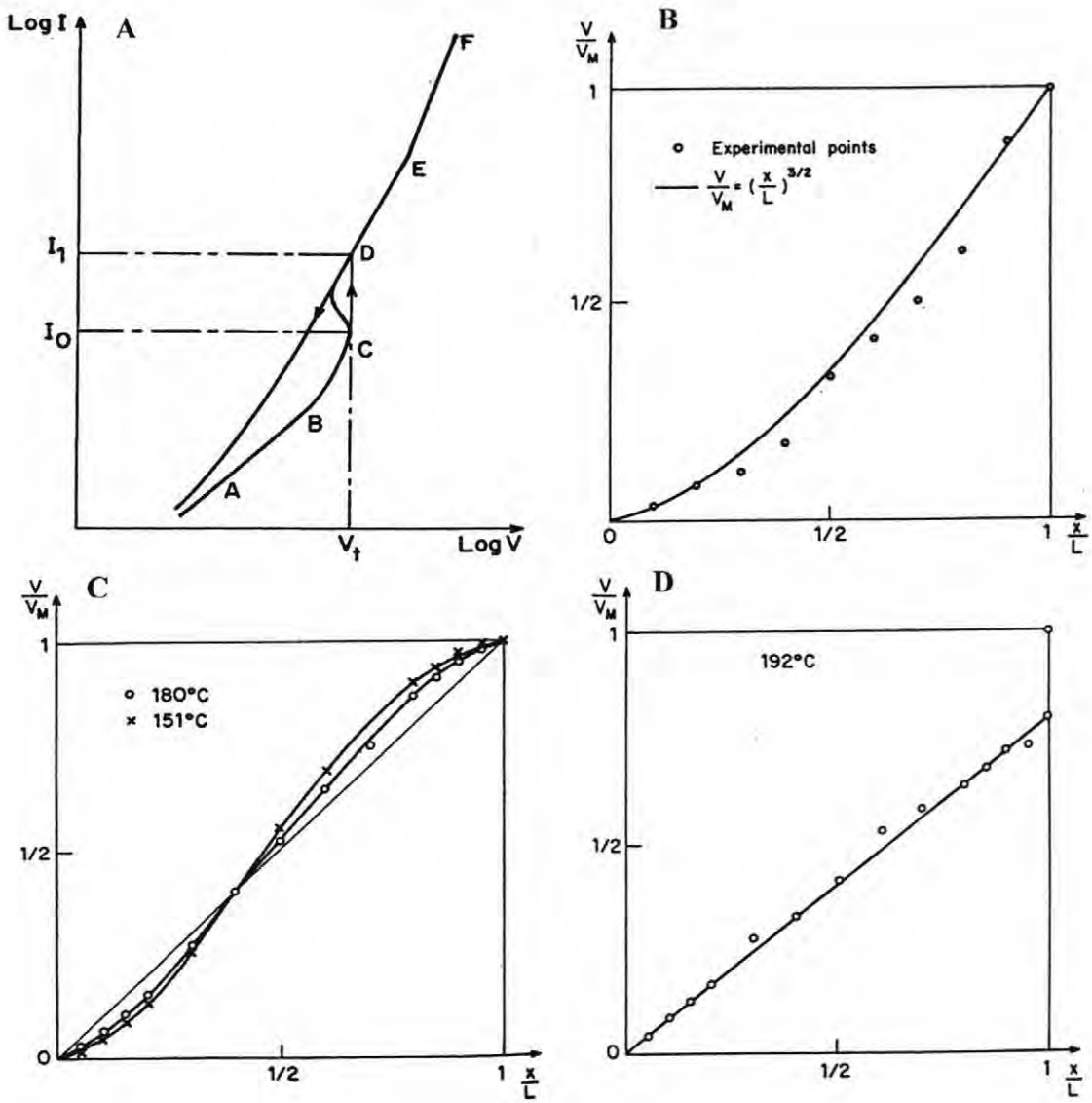

Figure 2–8: Potential distribution curves from Benguigui.[15] V is the voltage, V_M is the maximum voltage, L=10mm and x is the distance from the cathode.

A: Schematic of I-V behavior describing the AB- Ohmic region, BC- V^2 region, current increase, and DEF- high conductivity state.

B: Potential distribution of V^2 part of the low conductivity state at 150°C

C: Potential distribution of V^3 part of the high conductivity state at 150°C

D: Potential distribution for sample with blocking anode.

*2–8*C). This suggested that in this region there was double charge injection. Benguigui found the onset of coloration near the anode was accompanied by the onset of the V^2 relationship. In the V^2 range, applying the field in the opposite direction reversed the potential distribution. However, once a sample was taken past the ohmic region conductivity was irreversibly increased. These samples could be restored to the original conductivity condition by heating them above 400°C in air.[24]

Benguigui also investigated the effect of a blocking anode. If the anode was sealed with a thin coating of silicon dioxide, a uniform potential was obtained for voltages greater than V_t (*Figure 2–8)*.[15]

Sheng and coworkers also studied blocking Pt electrodes on iron doped TiO_2 ceramics. They also supported the reduction model and found that the platinum electrodes blocked oxygen transfer. In this experiment, samples with spot electrodes were cleaved through the electrodes, to leave partial electrodes that were on the fracture edge (*Figure 2–9)*. These electrodes were then tested under a dc electric field, at 200-350°C. These results showed a p-n junction I-V behavior developed after 60 min under an electrical stress of 10^5 V/m. The development of p-n junction behavior confirms the creation of a p and n type semiconducting regions. The data on the partial electrodes demonstrated that the current density saturates at a lower current density than a normal electrode. Sheng and coworkers suggested that at the fracture edge oxygen was absorbed. Thus, if the electrodes were on the fracture edge, the sample could absorb oxygen from the exposed area at the electrode. The adsorption would suppress the

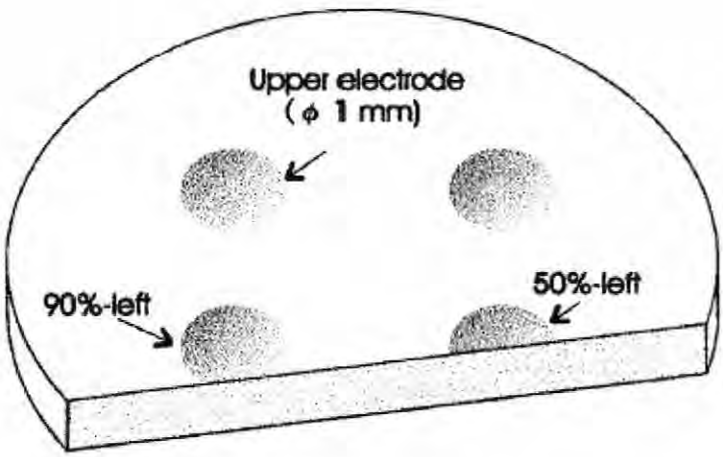

Figure 2–9: Schematic of cathode placement from work by Sheng.[5]

---

accumulation of oxygen vacancies at the cathode, causing a rapid saturation of current density (*Figure 2–10*).[5]

The electrodes utilized also affect the conduction and degradation of the material. Tredgold and Cox studied conductivity in $CaTiO_3$ and $SrTiO_3$ single crystals.[17] When gold or silver electrodes were used, a large increase in conductivity was observed as a function of time under dc field. However, when chromium, aluminum, zinc or cadmium was used, there was not a large increase in conductivity. They concluded that the rise in conductivity was not due to gaseous diffusion but maybe diffusion of the electrode. The mechanism is not specified but it seems likely that diffusion along or near the surface could be responsible, because diffusion though a close packed structure is very difficult. If the material below the electrode was removed, the initial conductivity could be

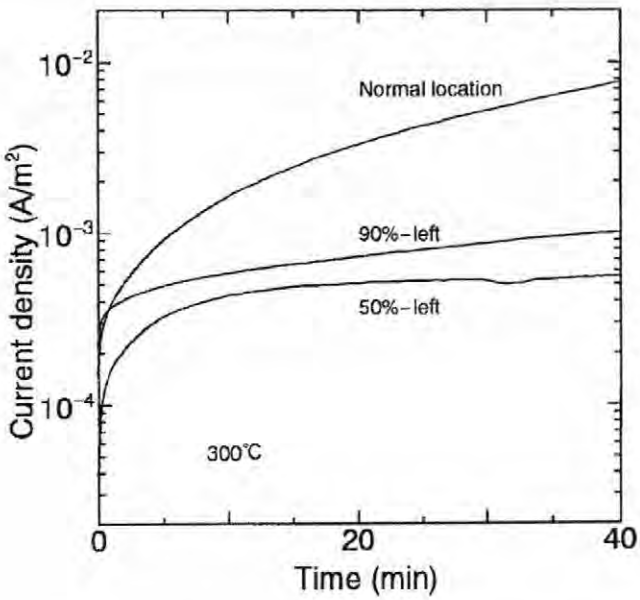

Figure 2–10: Comparison of time dependence of current density between samples with different cathode placements from Sheng.[5] The percentages refer to the amount of electrode remaining (see *Figure 2–9*).

restored, suggesting a problem with the surface layer. Cox and Triedgold also found that as the work function of the electrode increases, the apparent conductivity also increases.[19] This is consistent with recent work on leakage current density in $(Ba,Sr)TiO_3$.[16]

Studies by Buessem found electrode effects on the electrical properties of $BaTiO_3$. They found that the electrodes at the anode were oxidized after long term exposure to dc fields and that the potential distributions were affected. They suggested that the differences were due to the differences in the charge injection and annihilation of charge carriers, especially oxygen vacancies, at the electrodes.[8]

2.3 Electro-coloration in ABO_3 Perovskites

Coloration has also been observed in ceramic titanates when DC voltage is applied. Blanc and Staebler observed color changes in transition metal doped-strontium titanate single crystals, where the cathode took on the color of the reduced form of the transition metal dopant, such as blue for Mo^{5+}. As time increased, these colored regions moved towards each other. If the direction of the applied field was reversed, the colored regions receded, disappeared and reappeared corresponding to the new field direction. They interpreted their results as two conducting regions separated by a higher resistance region. To support this theory, the activation energies for conduction in strongly reduced and oxidized samples were measured. The activation energies were lower in the strongly reduced and oxidized specimens than in the untreated samples. [17]

Waser also studied electrocoloration in strontium titanate single crystals and found similar results to Blanc and Staebler. In iron doped strontium titanate, it was found that the area near the anode became red-brown, corresponding to Fe^{4+}. This Fe^{4+} has been found to exist in a similar perovskite structured material, $SrFeO_3$.[22] The area near the cathode became colorless, associated with Fe^{3+}. These results supported their theory of oxygen vacancy migration in which there is a reduced area at the cathode and an oxidized area at the anode. [12]

Kunin, Tsinkin and Shtrbina looked at coloration in strontium titanate single crystals. They found that the defects from electrical degradation are the same as those created from reduction. They found that a dark brown region would appear near the anode and move towards the cathode. With the appearance of this coloration they found

extra absorption peaks in the optical absorption spectra. As the leakage current increased the magnitude of the peaks would increase. When the samples were heated in a vacuum the same optical absorption spectra was formed.[23]

Lehovic and Shrine also studied the coloration, leakage currents and potential distributions in barium titanate doped with calcium zirconate. When an electric field was applied the area near the cathode became blue with a white halo and the area near the anode would become dark brown (*Figure 2–11*). As time increases the white halo and dark brown area increased in size. When the white halo and brown area touched, the leaked current increased by several orders of magnitude. [1] They suggested this halo was due to the point contact used to apply the field since it did not appear with a planar electrode configuration. They also found that the same coloration was present after exposure to x-rays. However, the latter coloration bleaches after 30min exposure to white light.

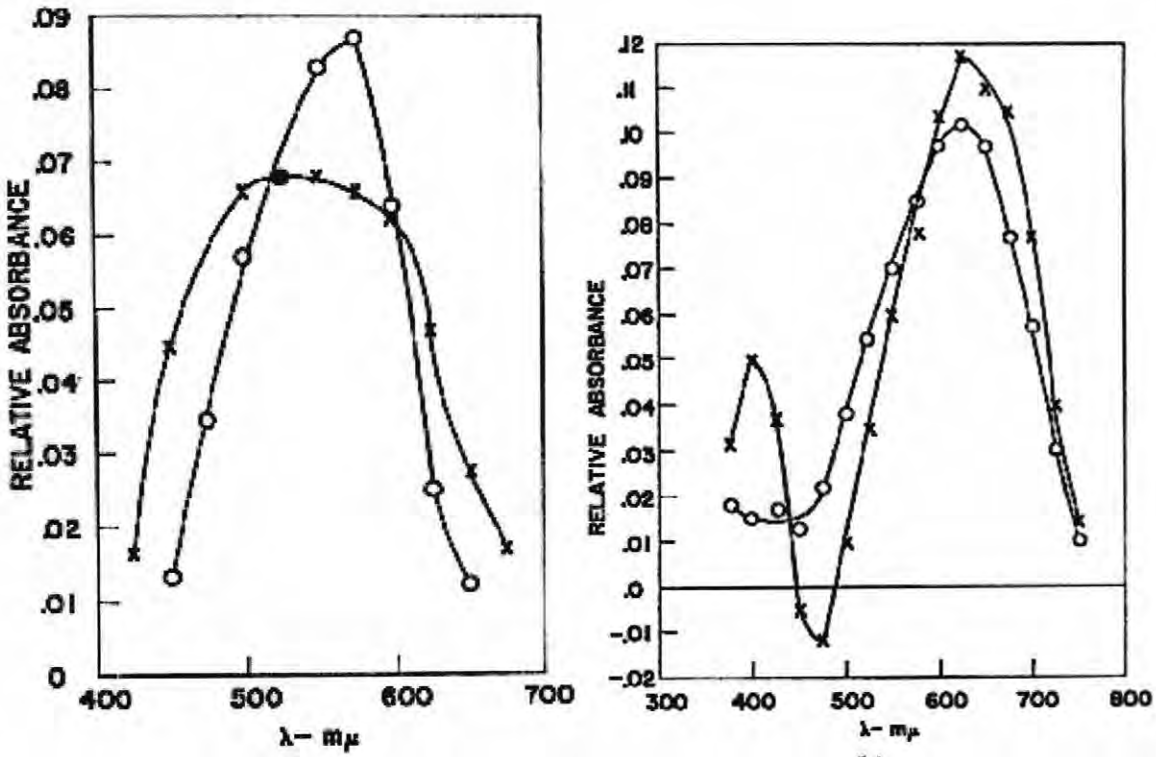

Figure 2–11: Relative absorption (with respect to an untreated sample) as a function of wavelength for ceramic $BaTiO_3$ sample for blue and brown regions. (a) Relative absorption spectrum for blue region emerging from the cathode relative to an untreated sample. (b) Relative absorption of dark brown regions in $BaTiO_3$. O-data for coloration by electrical field. X - coloration by x-ray irradiation.[1]

Chapter 3

EXPERIMENTAL PROCEDURE

In this thesis barium titanate and iron doped strontium titanate were examined. These materials were selected because of their use as dielectrics (see chapter one). Where possible, single crystals were examined to avoid complications associated with grain boundaries and density variations. Due to the limited availability of single crystals, ceramic $BaTiO_3$ was employed. Strontium titanate single crystals were also used because of their availability. Iron doped strontium titanate was chosen, over pure strontium titanate, both because it was investigated previously by Waser, and because it exhibited larger changes in optical properties during degradation in the spectral region examined.[2]

3.1 Sample Preparation

Ceramic $BaTiO_3$ was processed from TAM $BaTiO_3$ powder. The powder was thoroughly mixed with acryloid binder and then dried. The dried powder was ground in a mortar and pestle until it passed through a 100 mesh. This powder was then uniaxially pressed at 20ksi using a 0.5" die. The material was then heated at 3°/min to 600°C and held at 600°C for 5hr to burn out the binder. The material was sintered at 1300°C for 3hrs with a heating rate of 5°C/min. The processing yielded a ceramic $BaTiO_3$ pellet with, approximately, 95% of theoretical density.

Single crystals of strontium titanate doped with 0.15 mol% Fe were purchased from Commercial Crystals Labs Inc. in Naples, Fl. These crystals were <100> oriented and were diced to 10x10x0.5mm. As received, these crystals were epitaxially polished on one side.

For ellipsometric measurements, a smooth surface was required to minimize non-specular scattering due to surface roughness. This was achieved using the polishing procedure outlined in *Table 3–1*. The samples were polished using the 12μm Al_2O_3 grit until the surface was flat. Successively finer grits of Al_2O_3 powder were used for 20 min each. To improve the surface finish, diamond paste was used for 20 min to obtain a mirror finish on the samples. Subsequently, the samples were finished using colloidal silica for 20 min.

Table 3–1: Polishing procedure

Polishing Media	Substrate
12μm Al_2O_3	Glass
5μm Al_2O_3	Glass
3μm Al_2O_3	Glass
1μm Diamond Paste	Paper on glass
1μm Diamond Slurry	Brass Wheel with Beuhler Mastermet polishing pad
0.25μm Diamond Slurry	Brass Wheel with Beuhler Mastermet polishing pad
0.05μm Colloidal Silica	Brass Wheel with Beuhler Mastermet polishing pad

All samples examined in the course of this thesis were transparent in the visible spectrum. This can be a problem in ellipsometric measurements, where it is usually assumed that only the light reflected from the front surface will contribute to the signal. With transparent materials, it is possible for light to be reflected from the back surface.. In order to alleviate the problem, the back surface was roughened with 52μm SiC powder on glass and painted flat black. This eliminated a coherent reflection from the back surface.

3.2 Introduction to Spectroscopic Ellipsometry

Spectroscopic ellipsometry is a non-destructive technique used to examine the optical properties of materials. In this technique, a light beam of known intensity and polarization is reflected off a material and the relative change in phase and amplitude of the parallel (p) and perpendicular (s) components of the light are measured (*Figure 3–1*). The changes are related to the depth profile of the sample's dielectric function. The light reflected is generally elliptically polarized. In the instrument used in this thesis, the analyzer angle was rotated through 360° while the intensity is measured to get a complete description of the polarization state. For spectroscopic ellipsometry, this measurement is made for different wavelengths to determine the depth profile of the dielectric function. [21]

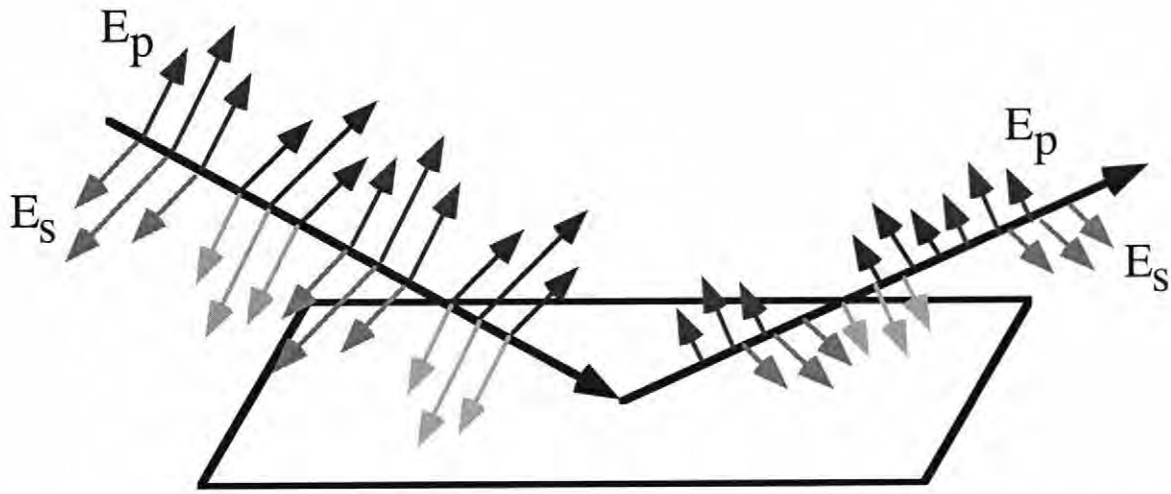

Figure 3–1: Reflection of light beam from a surface where p and s denote in plane and perpendicular polarization components, respectively. E is the electric field vector of the light.

The Fresnel coefficients describe the way in which light reflects from an interface. For a reflection at a single interface, some of the light is reflected and some is transmitted. The Fresnel coefficient is the ratio of the amplitudes of the reflected and incident waves. These reflection coefficients are dependent on the index of refraction and the incident angle as described in equation 3.1: [23]

$$r^s = \frac{N_1 \cos(\emptyset_1) - N_2 \cos(\emptyset_2)}{N_1 \cos(\emptyset_1) + N_2 \cos(\emptyset_2)}$$

$$r^p = \frac{N_2 \cos(\emptyset_1) - N_1 \cos(\emptyset_2)}{N_2 \cos(\emptyset_1) + N_1 \cos(\emptyset_2)} \qquad (3.1)$$

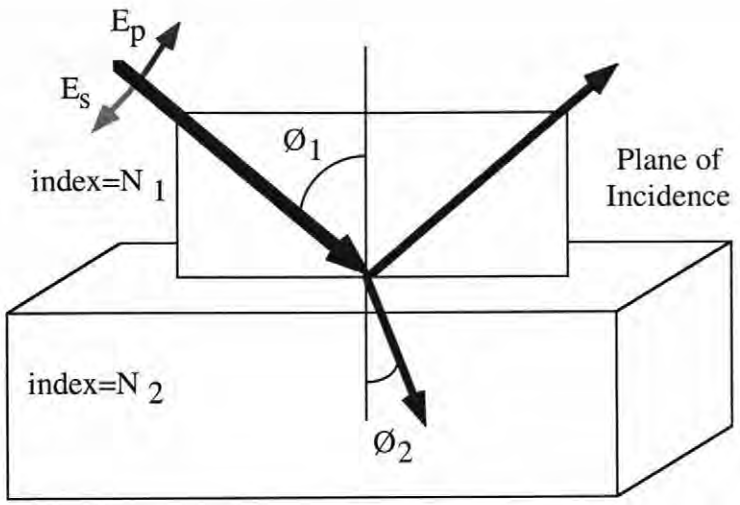

Figure 3–2: Schematic of light beam incident on a single interface.

where N is the complex index of refraction and ø is the angle as described in Figure *3–2*. Most samples have more complex depth profiles, where there are multiple interfaces within the sample (*Figure 3–3)*. The reflected wave contains information on reflections from more than one interface. This can be described by the total reflection coefficients.[23]

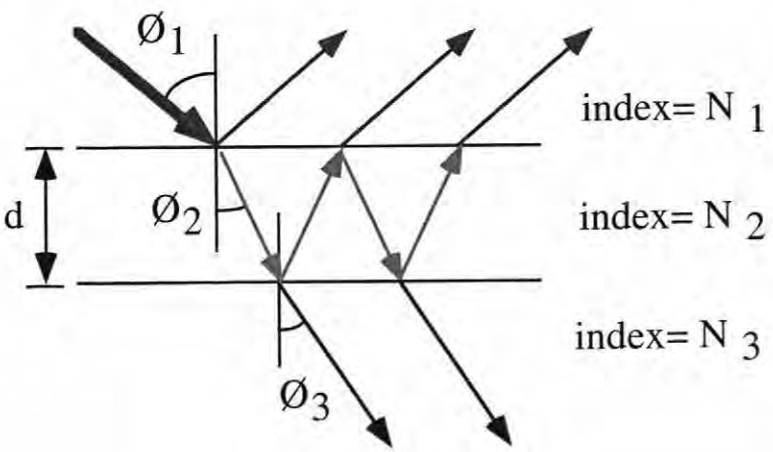

Figure 3–3: Schematic of reflection from multiple interfaces

$$r^s = \frac{r_{12}^s + r_{23}^s \ \exp(-j\,2\beta)}{1 + r_{12}^s r_{23}^s \ \exp(-j\,2\beta)}$$
$$r^P = \frac{r_{12}^p + r_{23}^p \ \exp(-j\,2\beta)}{1 + r_{12}^p r_{23}^p \ \exp(-j\,2\beta)} \qquad (3.2)$$

where r_{ij} denotes the individual reflection coefficients and ß is defined in equation 3.3.

$$\beta = 2\pi\left(\frac{d}{\lambda}\right) N_2 \cos \varnothing_2 \qquad (3.3)$$

This process can be treated iteratively to describe still more complicated depth profiles.

Delta (Δ) and psi (Ψ) are the fundamental parameters determined by ellipsometry. Δ is defined as the change in phase on reflection. [23]

$$\Delta = \delta_I - \delta_R \qquad (3.4)$$

where δ is the phase difference between the p and s components of the wave and I and R denote the incident and reflected waves.

Ψ is the ratio of the relative changes in amplitude for the parallel and perpendicular components, (r^P and r^S) as defined in equation 3.2. Thus, Ψ is the ratio of the amplitudes of the total reflection coefficients as in equation 3.5. [24]

$$\tan\Psi = \frac{|r^p|}{|r^s|} \qquad (3.5)$$

With this, the ellipsometric parameters Δ and Ψ can be related to the complex ratio of the total reflection coefficients:

$$\tan\Psi \; e^{j\Delta} = \frac{r^p}{r^s} \qquad (3.6)$$

Thus, the absolute intensities of the light are not required to determine Δ and Ψ, only the relative changes are necessary. In order to determine the depth profile of the material the wavelength and angle of incidence must be known. The actual determination of the depth profile will be discussed later with the modeling procedure in section 3.5.

The determination Δ and Ψ are different depending on the ellipsometer used. In this study, the instrument is configured with a rotating analyzer and a phototmultipler tube as a detector. The operation and calibration of the ellipsometer will be described in the following sections.

3.3 Rotating Analyzer Ellipsometer

The *ex-situ* ellipsometer is shown in figure *3–4*. In this configuration, the polarization state of the light incident on the sample was fixed and the polarization of the reflected beam was determined by rotating the analyzer. A computer was used to control the photomultiplier tube, determine the timing of data acquisition, step the monochromator, control the shutter, insert filters, and convert the intensities measured by the photomultiper tube (PMT) to Δ and Ψ. To allow accurate comparisons between

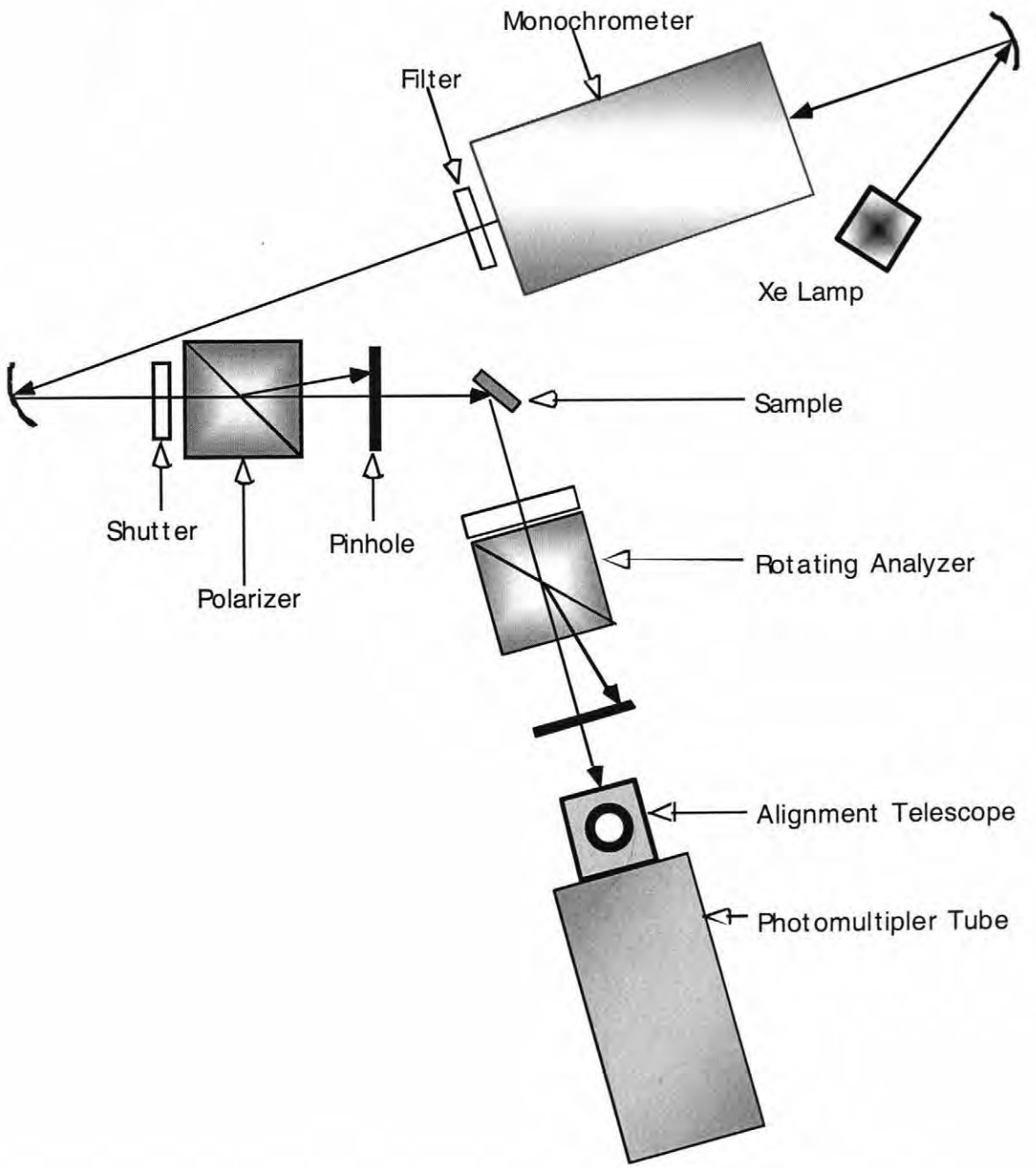

Figure 3–4: A schematic of the rotating polarizer ellipsometer used in this work.

different wavelengths, a feedback loop was employed, where the gain on the PMT was adjusted to make the average output signal the same for all incident energy levels. [22]

A Xe lamp was used to provide the incident light. The light was then passed through a double Czerny-Turner monochromator. Two filters were used to eliminate higher order diffracted beam that pass through the monochromator. A filter with a cutoff of 380nm was inserted at 400nm and a filter with a cutoff of 620nm is inserted at 650nm. The light was then polarized by a quartz rochon prism and passed through a pinhole. The light strikes the sample and is reflected. The light then passed through the rotating analyzer, which is also a quartz rochon prism. The intensity of the light was measured by the PMT.

The simplest way to describe the ellipsometer is though the Jones matrix representation (*Figure 3–5)*. In this configuration the following matrices can describe the ellipsometer: [24]

$$\begin{bmatrix} E_U \\ E_V \end{bmatrix} = \begin{bmatrix} 1 & 0 \\ 0 & 0 \end{bmatrix} \begin{bmatrix} \cos A & \sin A \\ -\sin A & \cos A \end{bmatrix} \begin{bmatrix} r_p & 0 \\ 0 & r_s \end{bmatrix} \begin{bmatrix} \cos P & \sin P \\ -\sin P & \cos P \end{bmatrix} \begin{bmatrix} 1 \\ 0 \end{bmatrix} E_0 \qquad (3.7)$$

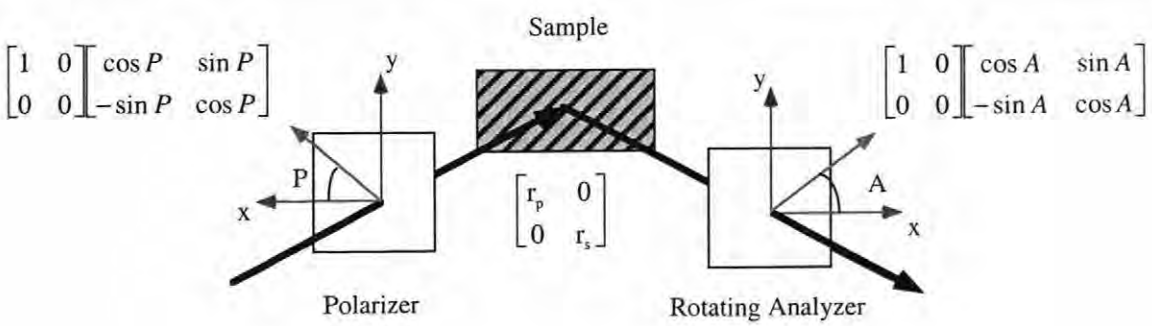

Figure 3–5: The Jones matrix representation of an ellipsometer describing the light detected at the photomultiplier tube.

where E_O is the incident electrical field, E_U and E_V are the components of the electrical field at the detector, P and A are the angles that the polarizer and analyzer make with respect to the laboratory frame as described in figure *3–5*.

In an ideal ellipsometer signal at the detector is given by equation 3.8. [24]

$$I = I_O[1 + \alpha \cos(2A) + \beta \sin(2A)] \qquad (3.8)$$

where α and β are the normalized Fourier coefficients determined from the analysis of reflected intensity as a function analyzer angle. By combining equation 3.8 and equation 3.6, Δ and Ψ are obtained from the Fourier coefficients: [24]

$$\tan \Psi = \left[\frac{1 + \alpha}{1 - \alpha}\right]^{\frac{1}{2}} \tan P \qquad (3.9)$$

$$\cos \Delta = \frac{\beta}{\sqrt{1 - \alpha^2}} \qquad (3.10)$$

This assumes that the system has perfect optics and ideal electronics. Calibration is required to account for imperfections and non-ideality the system. These will be discussed in the next section.

3.3.1 Alignment and Calibration of the Rotating Analyzer Ellipsometer

There are three main steps in calibrating the instrument for data collection. First, the system must be aligned. Then a residual calibration is performed to find the reference

polarizer and analyzer angles. Finally the eta calibration is performed to account for different gains of the ac and dc components of light.

The system alignment was done by mounting a HeNe laser in the position of the photomultiplier tube. The laser beam was then traced back to the source. The components were moved so they were centered in the beam. The photomultiplier tube is remounted and final adjustments were made to the mirror positions to maximize the intensity and reduce the differences between analyzer positions 180° apart.

A residual calibration was performed to correct for the non-idealities in the optics and detector. This procedure was first used by Aspnes.[27] Ideally the system is described by the Jones matrix in equation 3.7. However, a more accurate description is: [26]

$$\begin{bmatrix} E_U \\ E_V \end{bmatrix} = \begin{bmatrix} 1 & j\gamma_A \\ 0 & 0 \end{bmatrix} \begin{bmatrix} \cos(A - A_S) & \sin(A - A_S) \\ -\sin(A - A_S) & \cos(A - A_S) \end{bmatrix} \begin{bmatrix} r_p & 0 \\ 0 & r_s \end{bmatrix} \begin{bmatrix} \cos(P - P_S) & \sin(P - P_S) \\ -\sin(P - P_S) & \cos(P - P_S) \end{bmatrix} \begin{bmatrix} 1 \\ j\gamma_P \end{bmatrix} E_0 \quad (3.11)$$

where P_S (and A_S) are calibrations to adjust for the difference between the azimuth of the polarizer (or analyzer) and the azimuth of the laboratory frame. γ_A and γ_P are the optical activity coefficients for the analyzer and polarizer. These values are related to the system components and need to be determined before Δ and Ψ can be calculated.

To calibrate the system a gold sample was mounted on the ellipsometer. When a linearly polarized light beam is incident on the sample, it will reflect linearly polarized light if the incident beam is polarized either parallel or perpendicular to the plane of incidence.[22] This reflected light beam is then 100% modulated so that the minimum of the ac component of the amplitude is equal to the dc background. When the polarized state of the light is not parallel or perpendicular to the plane of incidence, the reflected

light is elliptically polarized and the light is not fully modulated. In addition, optically active polarizers and analyzers will cause the position of 100% modulation to be shifted from P_S to another angle P_1. P_1 can be determined by a residual function:

$$R(P) = 1 - \alpha^2 - \beta^2 \qquad (3.12)$$

Data were collected on the gold sample around the 0 and 90° positions of the polarizer. The polarizer is stepped from 5° degrees below (0 or 90°) to 5° above. The Fourier coefficients were then fitted to equation 3.12. The minimum of this equation yields P_1, i.e. $R(P_1)$ is the lowest R(P). P_S and A_S can then be calculated from:[27]

$$P_S = P_1 - \left(\frac{\gamma_A \tan \Psi + \gamma_P \cos \Delta}{\sin \Delta} \right) \qquad (3.13)$$

Once P_S is known, A_S can then be calculated: [27]

$$A_S = A_1 - \left(\frac{\gamma_P \tan \Psi + \gamma_A \cos \Delta}{\sin \Delta} \right) \qquad (3.14)$$

where:

$$A_1 = \frac{1}{2} \tan^{-1}\left(\frac{\beta}{\alpha} \right) \qquad (3.15)$$

The values obtained at 0° and 90° positions of the polarizer were averaged to get more accurate values.

A more realistic description of the measured intensity than that given by equation 3.8 incorporates an eta correction:[24]

$$I = I_o[1 + \eta\alpha \cos(2A) + \eta\beta \sin(2A)] \qquad (3.16)$$

Eta (η) is the difference in the gain of the photomultiplier tube and electronics for static and dynamic components of the intensity. Eta is also dependent on the voltage of the photomultiplier tube. Fortunately, for the system used in this thesis, η had a linear dependence on the voltage.[22]

The values for eta were measured by placing a circularly graded neutral density filter in the beam path with the system in the straight through configuration. The α and β were calculated for the different photomultiplier tube voltages (corresponding to different incoming intensities) and converted to eta by equation 3.17.[23]

$$\eta = \frac{1}{\sqrt{\alpha^2 + \beta^2}} \qquad (3.17)$$

The photomultiplier tube voltages were changed by rotating the neutral density filter. Measurements of eta were made for PMT voltages of 550-1000V. The eta values were then fit to a linear function in voltage to allow calculation of eta at different photomultiplier tube voltages. During measurements, the eta values were used to correct the values of Δ and Ψ.[23]

3.3.2 Collection of Ellipsometric Data

After all the calibrations are completed, the sample can be mounted. This was done with a vacuum chuck or silver paint if the hot stage is being used. The angle of

incidence was set to 70 or 80°, depending on the sample. The sample was then aligned to reflect the beam to the detector. Alignment was assisted by redirecting the beam into a telescope to center the reflected beam. Final adjustments were made to minimize the difference between optical cycles of the analyzer.

With the alignment of the sample completed, the monochromator was set to 250nm. The computer was programmed to take data every 5nm. For each wavelength, data were averaged over 50 mechanical cycles of the analyzer. At each wavelength, the beam was blocked using a shutter and a background I(A) was measured with the PMT voltage fixed to the value used for the wavelength. This background was subtracted from the measured intensity before calculating Δ and Ψ.

The ellipsometer could also be fitted with a hot stage that allowed the temperature to be adjusted up to 700°C (*Figure 3–6*). In this hot stage the sample was mounted vertically to the holder using silver paint. The temperature was regulated using three cartridge heaters connected to a temperature controller. The temperature was measured using a thermocouple inserted from the top of the hot stage and placed next to the surface of the sample. To prevent the optics on the ellipsometer from being heated, the hot stage was equipped with a water-cooled jacket. The beam entered and exited the hot stage through holes aligned for 70° and 80° angle of incidence. Adjustments to the sample alignment were made possible by the two-way adjustable sample mount (in addition to translation and rotation not built into the stage).

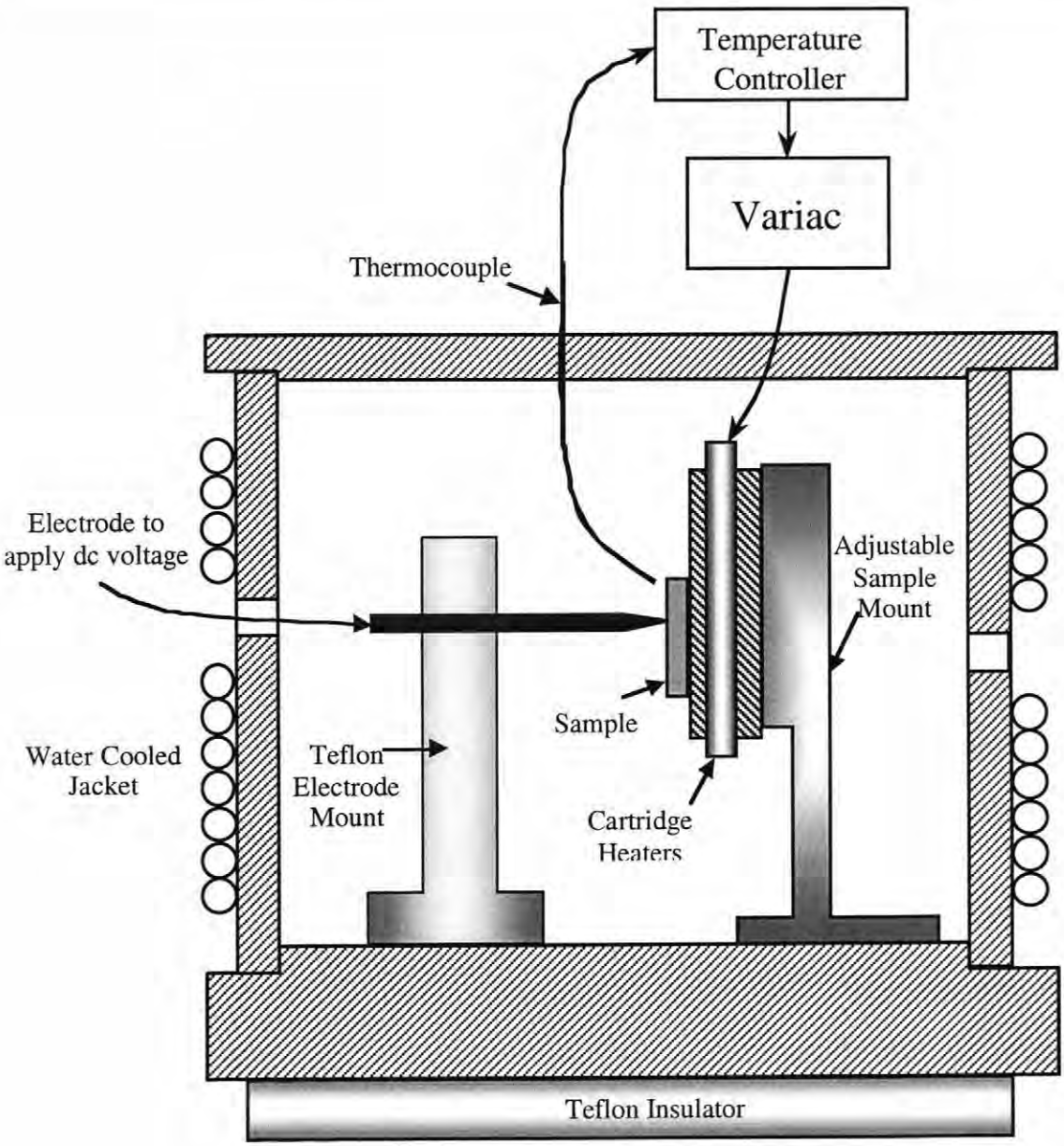

Figure 3–6: Schematic of hot stage for ellipsometer

This hot stage was modified to apply a voltage to a sample. A teflon mount was fabricated to hold and insulate an electrode. The teflon limited the hot stage to temperatures less than 250°C in this configuration. The electrode was threaded and could be moved in and out by turning via a hole in the cooling jacket. The electrode could be positioned just above the beam so that it did not interfere with the measurements. It could also be positioned in the beam path so that a measurement could be made exactly where the electrode contacts the sample by retracting the electrode.

3.3.3 Transparent Materials

The measurements of Δ near 0 or 180° are inherently inaccurate in a standard fixed polarizer-rotating analyzer ellipsometer.[23] This is because the phase change of polarized light on reflection from a transparent material is near 0 or 180° and the error in the measurement of Δ is proportional to $\frac{1}{\sin\Delta}$.[29] This problem can be overcome by inserting an achromatic compensator into the system after the polarizer and before the sample. A three-reflection quarter waveplate compensator was used (*Figure 3–7*). The internal reflections cause a phase change of approximately 90°. This additional phase shift of 90° allows the measurement of Δ to be made near 90° where small changes in ellipticity can be measured accurately. Because the compensator was made of vitreous silica, which does not have any optical activity, recalibration of A_S and P_S was not necessary when using the compensator.[23]

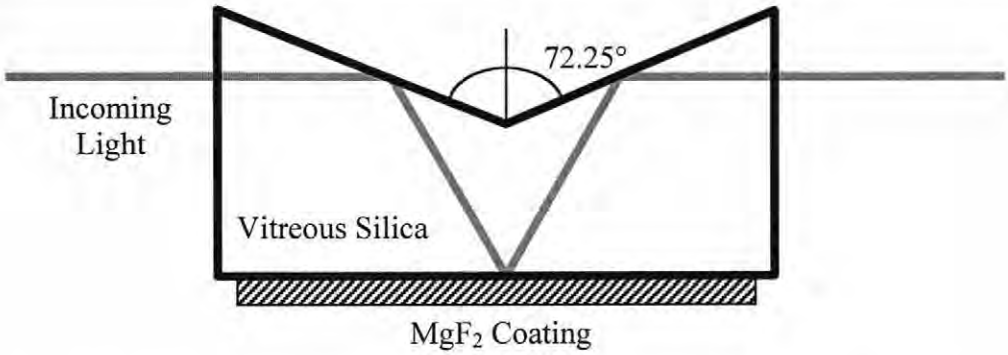

Figure 3–7: Schematic of three-reflection quarter waveplate compensator used on rotating analyzer ellipsometer

To analyze a transparent material, two measurements were made. This was done to provide an effective source calibration. The first data set was measured in the 'straight through' position, where the angle of incidence was 90° and there was no sample in place. Thus, the beam could travel directly from the compensator to the analyzer. This allowed the determination of the phase shift due to the compensator as a function of wavelength. The sample was then mounted, the angle of incidence adjusted, and the sample aligned. The second set of data collected contained the information on the sample and the phase shift from the compensator. The phase shift from the sample was determined by the equation:[23]

$$\tan \Psi \quad e^{j\,\Delta} = \frac{\tan \Psi_2 \quad e^{j\Delta_2}}{\tan \Psi_1 \quad e^{j\Delta_1}} \qquad (3.18)$$

where the subscript 1 denotes the straight through data set measuring only the compensator and 2 denotes the measurement made on the sample with the compensator. This allowed the removal of the phase change introduced by the compensator.

3.4 Modeling of Spectroscopic Ellipsometry Data

Direct inversion of ellipsometry data to determine the optical properties of samples with unknown depth profiles can lead to large errors. Therefore, in most cases SE data are modeled to determine the optical properties. For an unknown material the dielectric function and its depth profile can be determined. To model SE data, a realistic geometry must be postulated. This is done by separating the sample into discrete layers parallel to the surface, each with homogenous optical properties. Reference data are used for the optical properties of these layers if available. If the optical properties are unknown, a Sellmeier dispersion equation can be used to describe the optical properties of dielectric materials:[24]

$$N^2(\lambda) = A + B\frac{\lambda^2}{\lambda^2 - \lambda_O^2} \qquad (3.19)$$

where A is a constant, B is the oscillator strength, λ is the wavelength and λ_O is related to the position of the optical band gap. The optical properties of mixed phase layers were determined utilizing Bruggeman effective medium theory.[22,25,26,29] For each proposed geometry, the program calculated the best fit for the thickness of the layers and the

optical properties of each material. When Δ was low the values of Δ and Ψ for the models were calculated and compared to the experimental values using the unbiased estimator of fit, σ:[22]

$$\sigma = \frac{1}{\sqrt{m-p+1}}\left[\sum_{i=1}^{m}\left\{\left(\Delta_{i,\exp}-\Delta_{i,cal}\right)^2+\left(\Psi_{i,\exp}-\Psi_{i,cal}\right)^2\right\}^{\frac{1}{2}}\right] \quad (3.20)$$

Here $\Delta_{i,cal}$ and $\psi_{i,cal}$ are the calculated values from the proposed model; $\Delta_{i,exp}$ and $\psi_{i,exp}$ are the measured ellipsometric data; m is the number of wavelengths at which data were collected; p is the number of unknown parameters. For samples that were not transparent, cos(Δ) and tan(Ψ) were used instead of Δ and Ψ for calculation of σ. The use of Δ and Ψ weights the data to amplify the importance of small Δ values and help fit data for transparent materials.[23] The unknown variables were adjusted to minimize the unbiased estimator of fit. This was first done by use of a grid search over parameter space. Then a linear regression analysis algorithm was used to iterate around the best values determined by the grid search. For each sample several different geometries were examined. The best fit model was chosen based on five criteria: 1) physically realistic values for the unknown variables; 2) low values of σ; 3) low values of 90% confidence limits; 4) good agreement between experimental and modeled data; 5) low values of cross correlation coefficients between variables.[22]

Ellipsometry data can be used to construct depth profiles on an angstrom scale. For samples where the composition was graded, this can be treated by creating a model with many layers (*Figure 3–8)*. In this thesis, concentration gradients were treated by

approximating an erf function with a step function of layers with uniform concentration: [29]

$$c(x,t) = \frac{C_s}{2}\left[1 + erf\left(\frac{x}{2\sqrt{Dt}}\right)\right] \qquad (3.21)$$

where c(x,t) is the concentration at time t and a distance x from the surface, C_S is the surface concentration, and D is the diffusion coefficient. The model of a concentration gradient is broken into a specified number of layers. These steps were determined by dividing the surface concentration C_S by the number of layers to get the concentrations difference between steps:[29]

$$C(x_i) = \left[1 - \sum_{i=1}^{m} \frac{i-1}{m}\right] C_S \qquad (3.22)$$

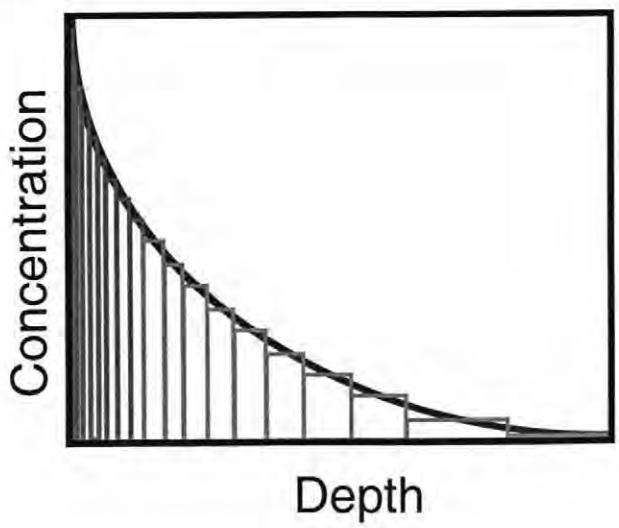

Figure 3–8: Schematic of depth profile following an erf function, with multiple layers of varying composition and thickness

where m is the number of layers and i denotes the i^{th} layer. This determines the concentration of each of the steps allowing for the use of thin layers where the concentration is rapidly changing and larger layers where the concentration slowly changing. The depths (x_i) of the steps were back calculated from equation 3.21 using a specified C_S and $\sqrt{Dt}$ (effective diffusion thickness). The thickness (b) of the layers could then be calculated:

$$b_i = \left(\frac{x_i - x_{i-1}}{2} \right) - \text{thickness of previous layers} \qquad (3.23)$$

The differences between these depths wee divided between adjacent layers to create the step widths (*Figure 3–9*). The computer iterated this process for many $\sqrt{Dt}$ and C_S possibilities and uses the linear regression analysis to optimize the values of $\sqrt{Dt}$ and

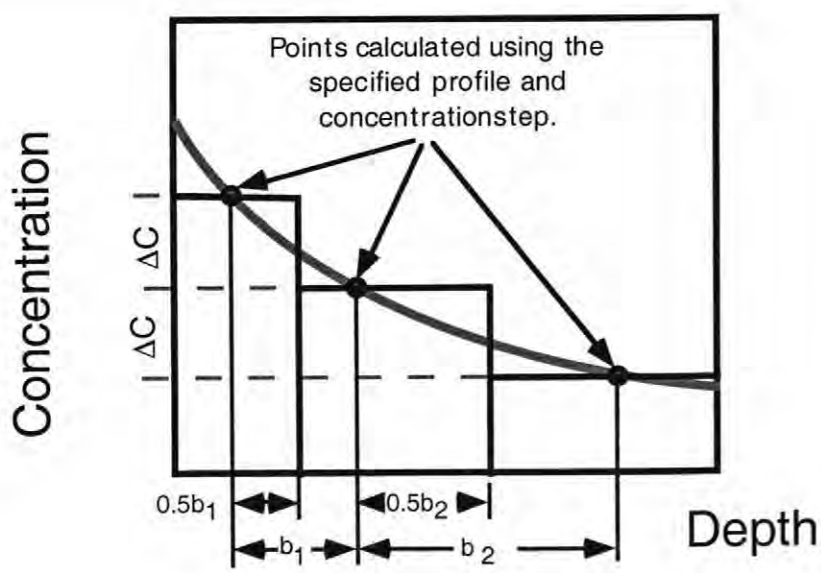

Figure 3–9: Schematic of method by which widths of the steps are calculated.

C_S.[26] For this thesis the model used two reference states, oxidized and reduced material, and C_S was a mole percentage of this the reduced material at the surface.

3.5 Degradation of Samples

Samples were degraded under dc fields. This was performed at elevated temperatures to expedite the degradation time scale to hours. This was done in two different setups. The first was *in-situ,* this used the hot stage that was retrofitted with a retractable electrode (*Figure 3–6*). The sample was mounted to the vertical sample holder with silver paint to allow for grounding of the back of the sample. A voltage of 1.25 to 1.35kVwas applied using the electrode and a PS350 Princeton power supply. To expedite degradation, samples were heated to 130-150°C, regulated by an Extec 48VTR temperature controller. SE data were collected at 15min intervals until the current reached 4.0mA.

In the second set of experiments the samples were degraded *ex-situ*. The samples were degraded on a hotplate at 130-150°C. Electrical contact was made to the back of the sample using an aluminum sheet and silver paint.(*Figure 3–10*) A microprobe was employed to make contact with the top of the sample. An Extec 48VTR temperature controller, with a thermocouple, was used to regulate the temperature of the hotplate. The samples were removed after degradation and measured on the ellipsometer after the electrodes were removed. (See chapter 5 for details on electrode) This was repeated for several different times.

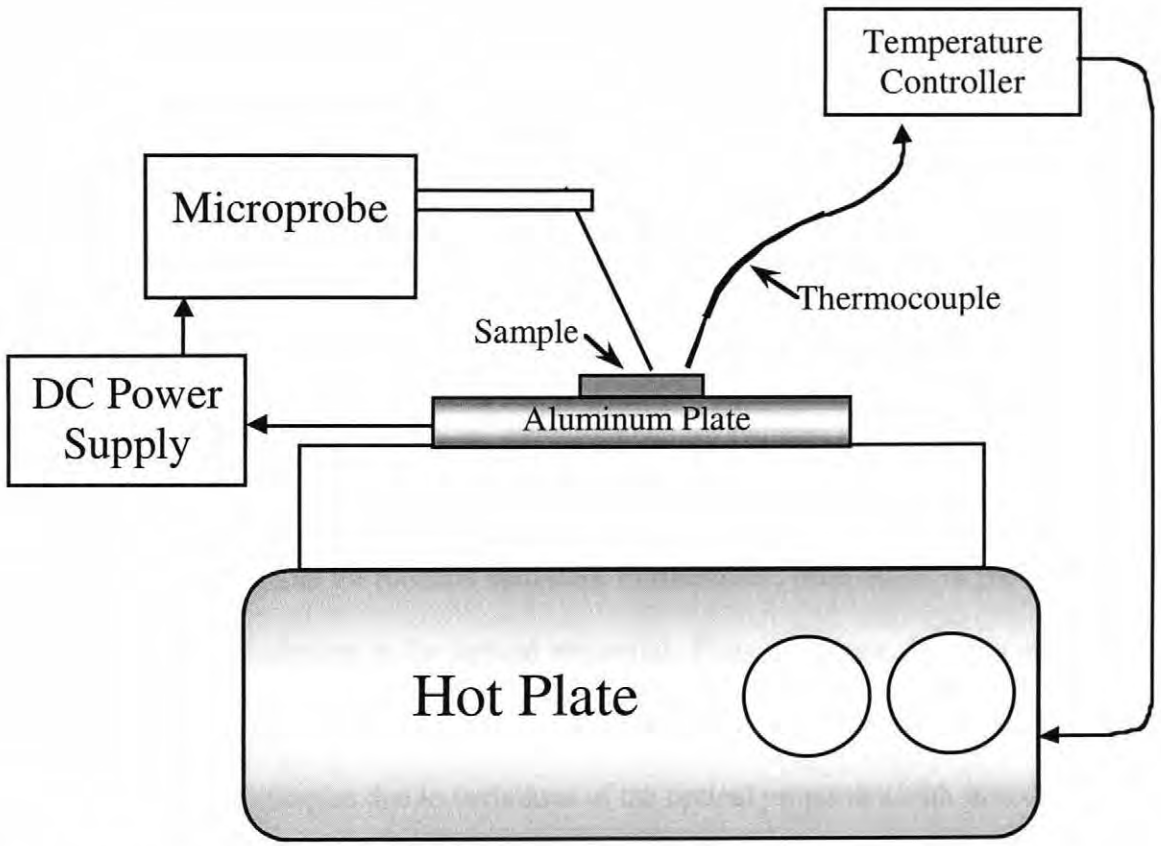

Figure 3–10: Schematic of ex-situ experimental setup.

Chapter 4

SENSITIVITY OF SPECTROSCOPIC ELLIPSOMETRY TO DEGRADED LAYERS

Reference dielectric functions were obtained for reduced and oxidized $BaTiO_3$ and iron-doped $SrTiO_3$. Reference data from the literature could not be used because there was little available for reduced materials. Furthermore, differences in processing of ceramics leads to variations in the optical properties. Thus, reference data was needed for the ceramics used here. Reference data for the iron doped strontium titanate needed to be determined for the samples due to variations of the optical properties with iron doping.

The reference data were used to model the changes in the optical properties of these materials that occur during degradation. The sensitivity of ellipsometry to the presence of discrete or graded layers of reduced material was investigated. Also, delta-psi trajectories corresponding to various degraded surface layers were also examined. In this section, data were modeled for an angle of incidence (AOI) of 70° or 80°.

4.1 Reference Dielectric Function Determination

Barium titanate ceramics were polished to produce a mirror finish by using successively finer powders on a glass plate, a series of diamond slurries, and finally colloidal silica (See Chapter 3 for sample preparation details). Then SE data were

collected between 250 and 750nm for virgin and reduced barium titanate samples at an 80° angle of incidence (AOI). A model was constructed to allow for the extraction of optical properties. The data set fit was 400 to 675nm, in order to be able to describe the optical properties with an oscillator (i.e. data near the absorption edge were not used in the initial model). This best fit model entailed a 222±27Å low index layer (treated as a mixture of air and barium titanate), to account for surface roughness and any polishing induced surface damage, on top of bulk barium titanate (*Figure 4–1*a). This model fit the experimental data very well with a σ of 0.05° (*Figure 4–1*b).

With the microstructure fixed from the long wavelength data (where the oscillator model can be used to describe the optical properties of $BaTiO_3$) the short wavelength data were directly inverted. The resulting optical properties are seen in *Figure 4–1*c where $\varepsilon_1 + \varepsilon_2 = \left(\tilde{N}\right)^2$. These properties are similar to the reference data determined by DiDomenico and Wemple[30], and Cardona[31] (*Figure 4–2*). The reference data from DiDomenico and Wemple is only available for wavelengths longer than 350nm because it was obtained from transmission measurements and $BaTiO_3$ is not very transparent below this wavelength. The data determined here show good agreement to the reference data away from the absorption edge. Much of the residual difference is probably due to the density difference between the ceramic and the single crystal, smoother surfaces and impurtities. The ceramic samples are approximately 96% dense. When the data were modeled using the reference data set, the best fit converged to a bulk density of 95±3% for the ceramic.

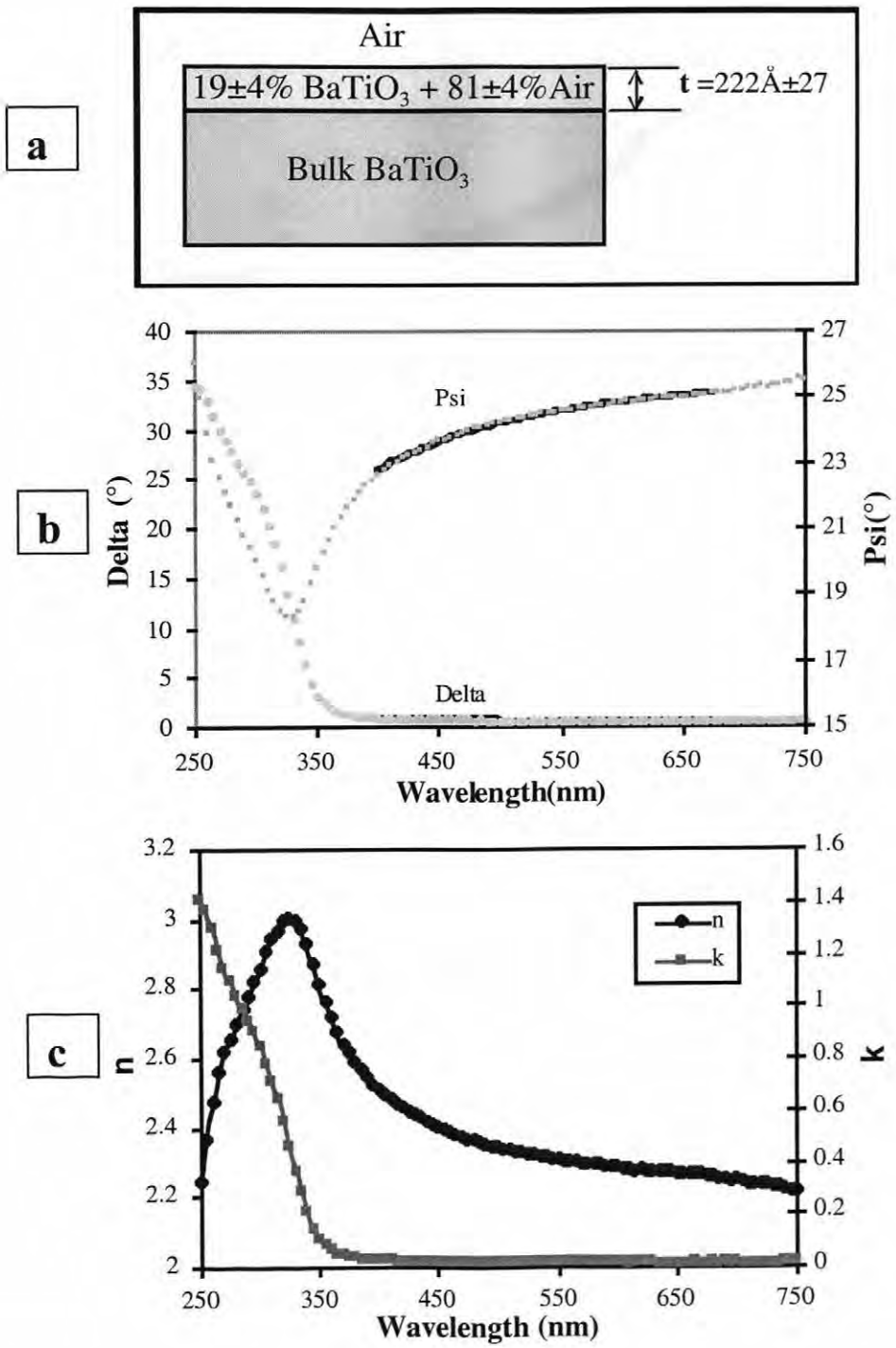

Figure 4–1: Modeling to determine the reference dielectric functions for ceramic $BaTiO_3$. (a) Best fit sample depth profile (b) Plot of modeled data and experimental data showing good agreement. Symbols correspond to the experimental data, and the lines are modeled data (c) Optical properties determined from data.

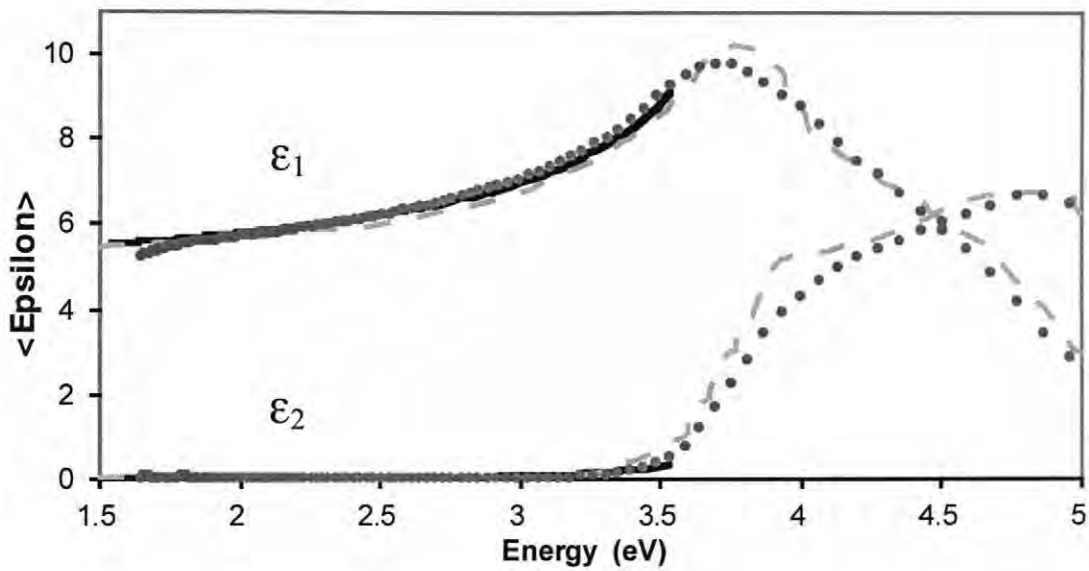

Figure 4–2: The complex dielectric function for reference data determined by DiDomenico and Wemple (line), Cardona (dashed line) and data collected for $BaTiO_3$ samples (●).

The ceramic samples were then reduced in an atmosphere of nitrogen and hydrogen with an oxygen partial pressure of 10^{-13} atm for 24 hrs at 900°C and repolished. Just as with the virgin $BaTiO_3$, a model was constructed for the long wavelength data with a low index layer (to account for roughness and surface damage) and bulk reduced $BaTiO_3$ (*Figure 4–3a*). This model also had a good fit to the experimentally measured data between 400 to 650nm with a σ of 0.06° (*Figure 4–3b*). With this depth profile the optical properties for the reference data set were determined (*Figure 4–3c*). The optical data for the reduced samples show that the absorption edge shifted several

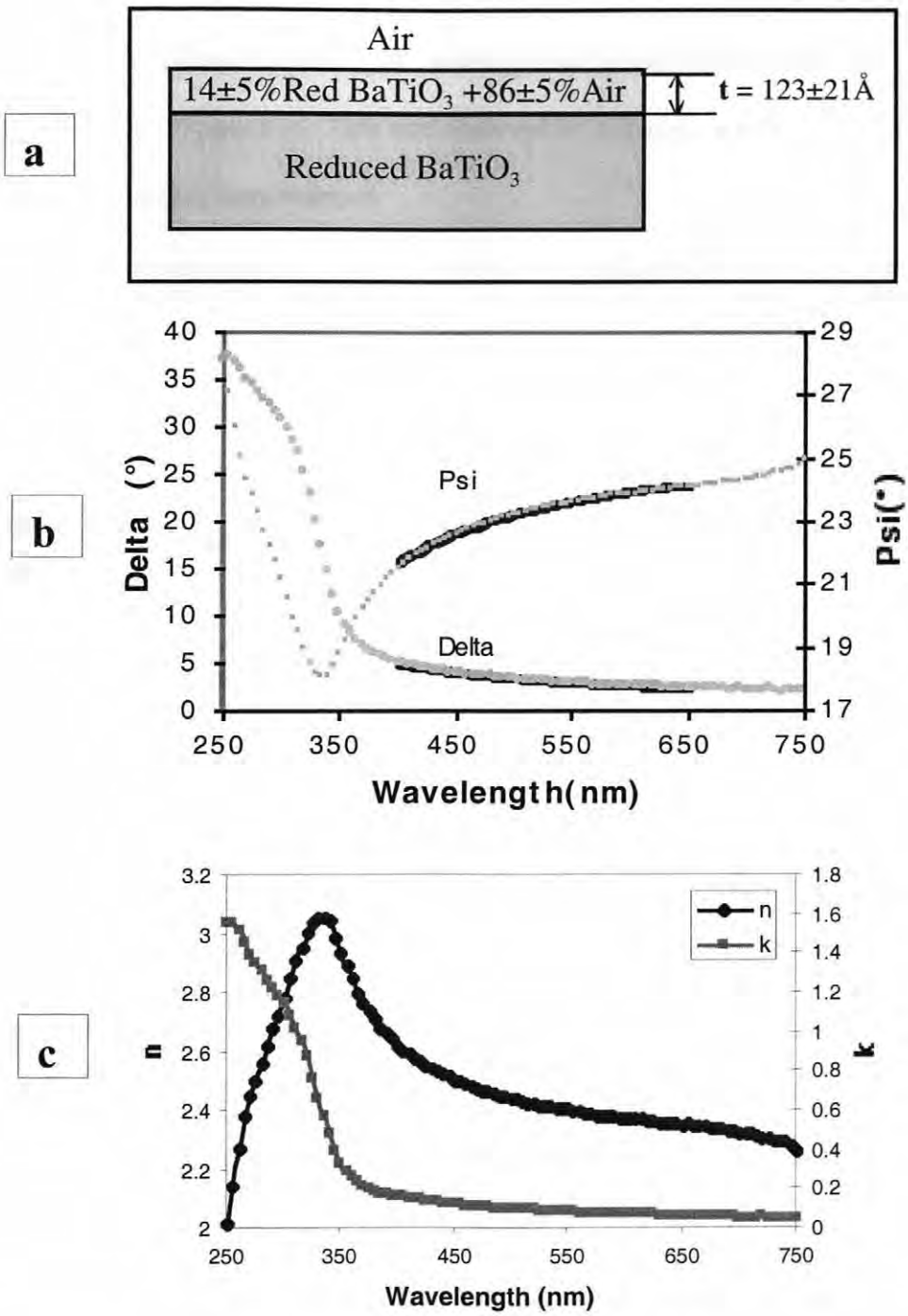

Figure 4–3: Modeling to determine the reference dielectric functions for reduced ceramic $BaTiO_3$. (a) Best fit sample depth profile (b) Plot of modeled data, for fit in (a), and experimental data showing good agreement. Symbols correspond to the experimental data, and the lines are modeled data (c) Optical properties determined from data.

nanometers to longer wavelengths, accompanied by an increase in the absorption across the spectrum (*Figure 4–4).* This was observed by a change in color from tan to blue-gray when the samples were reduced.

The same procedure was performed on $SrTiO_3$ single crystals doped with 0.15 mole% iron. An iron doped $SrTiO_3$ single crystal was polished to produce a mirror finish as described in Chapter 3. SE data were collected for virgin (oxidized) and reduced $SrTiO_3$ samples. The samples were reduced in an atmosphere of nitrogen and hydrogen with an oxygen partial pressure of 10^{-13} atm at 1200°C for 24 hrs and repolished. The reduction caused a change in the color of the sample from red-brown to clear.

The ellipsometry data for the virgin and reduced iron doped $SrTiO_3$ were used to determine reference data sets. Just as with the barium titanate, a model of the depth profile was constructed with a low index layer of roughness, with mixed bulk and air, and bulk material (*Figure 4–5a, 4–6a).* These models have a roughness layer with the volume fraction of iron doped $SrTiO_3$ fixed at 50%. This was done because the roughness layer of the substrates is very low and varying the volume fraction resulted in large correlation between variables. These models fit the experimentally measured data between 450 and 650nm with a σ of 0.05° and 0.03° for the virgin and reduced materials (*Figure 4–5b, 4–6b).* The optical properties of the samples were obtained by direct inversion of ellipsometric data with these depth profile models (*Figure 4–5c, 4–6c).*

The SE data for these samples show that on reduction the absorption peak shifted a few nanometers, accompanied by a reduction in the absorption across the spectrum (*Figure 4-5*). However, this shift is smaller than the shift for the $BaTiO_3$.

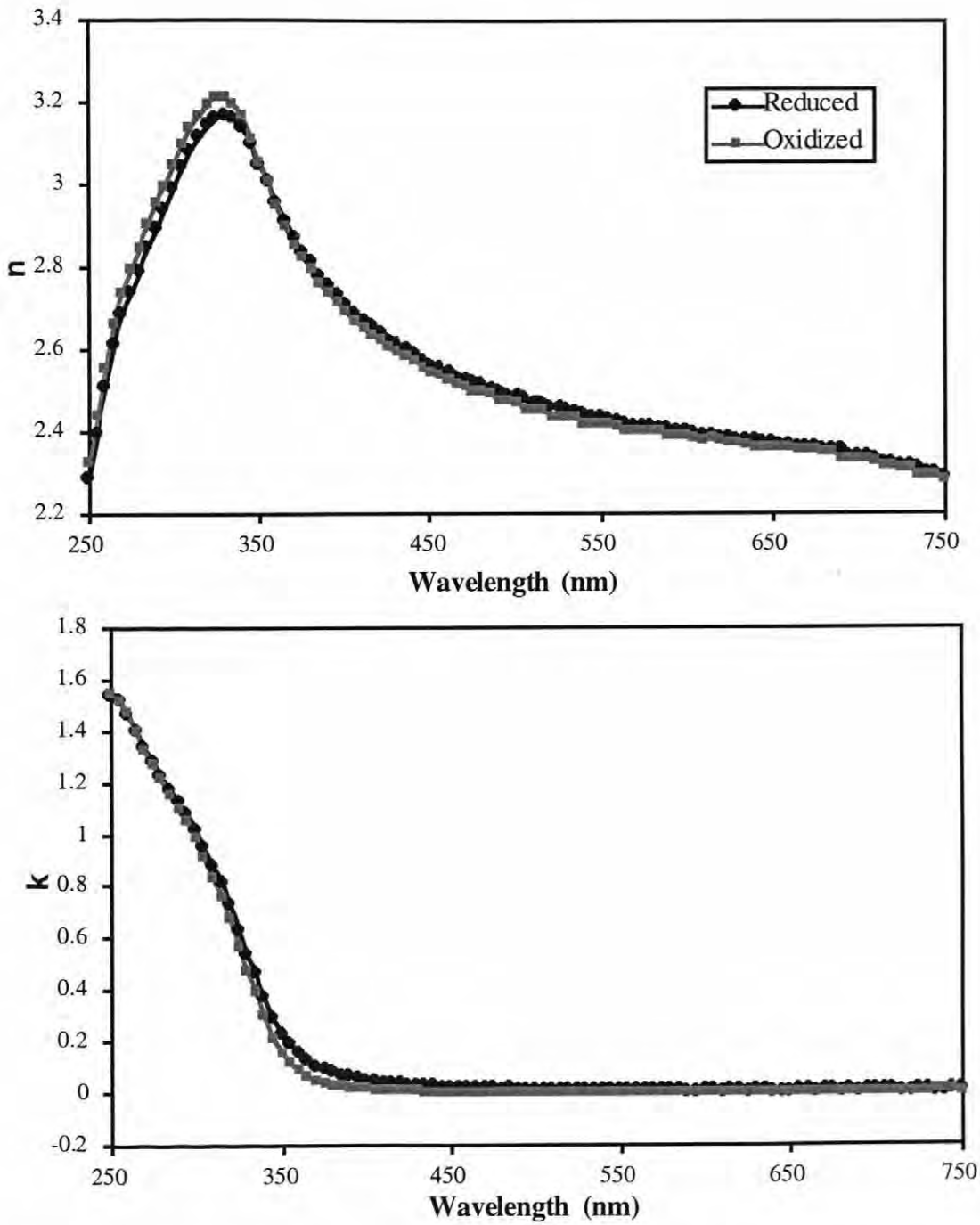

Figure 4–4: Optical data for reduced and oxidized ceramic $BaTiO_3$ determined from ellipsometry.

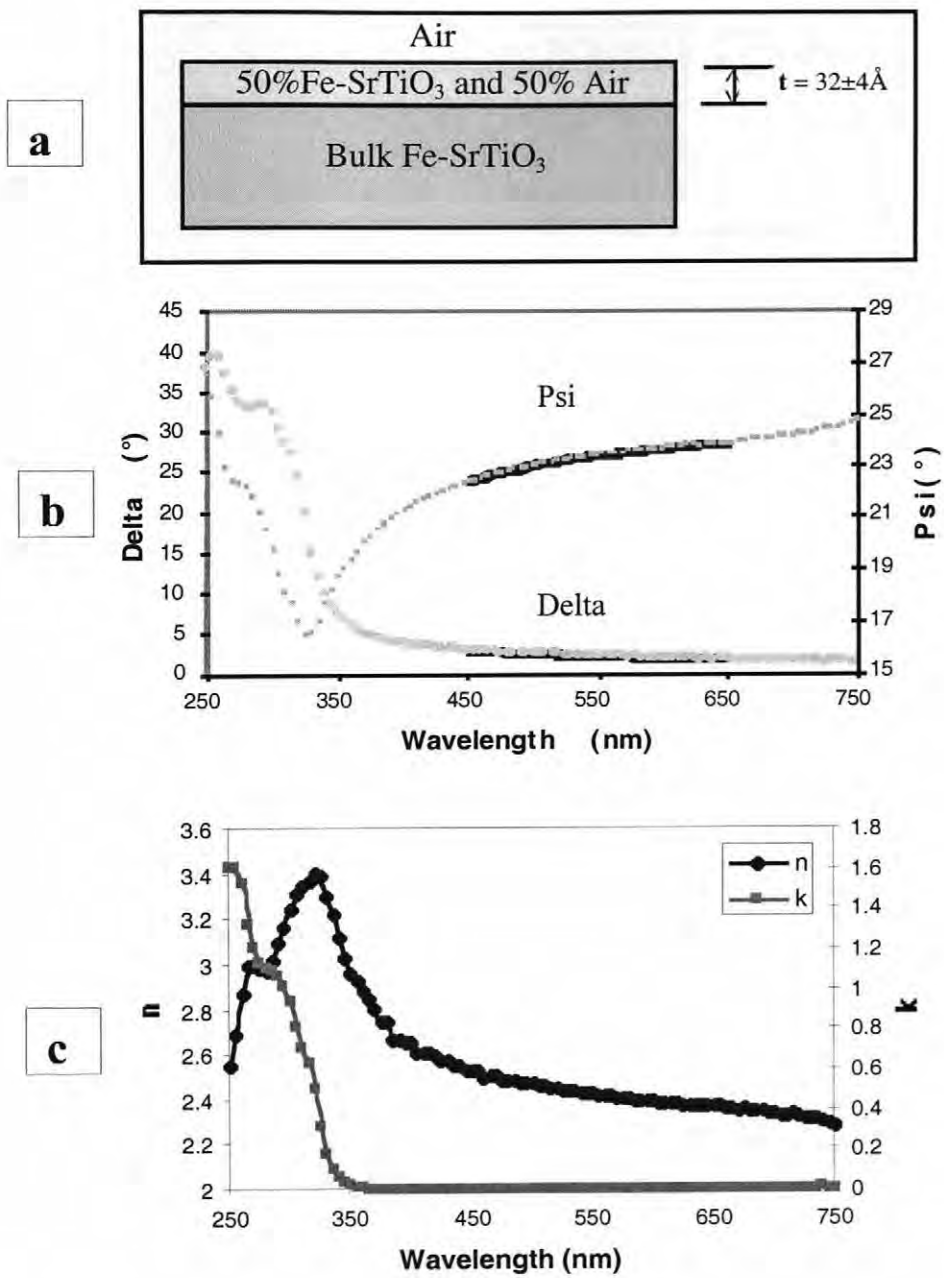

Figure 4–5: Modeling to determine the reference dielectric function for iron doped $SrTiO_3$ single crystals. (a) Fitted sample depth profile (b) Plot of modeled data, for fit in (a), and experimental data showing good agreement. Symbols correspond to the experimental data, and the lines are modeled data (c) Optical properties determined from data.

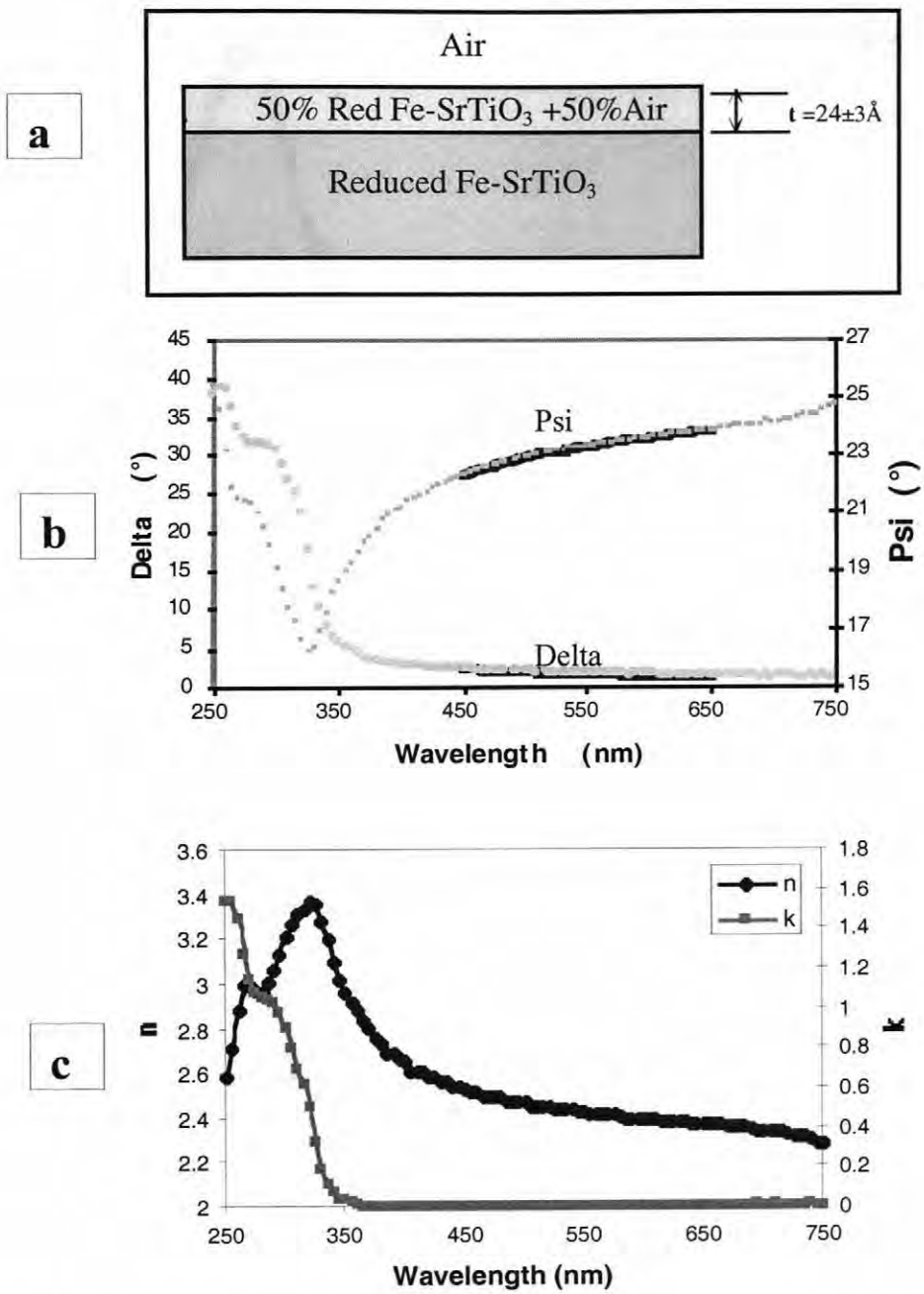

Figure 4–6: Modeling to determine the reference function for reduced iron doped $SrTiO_3$ single crystals. (a) Fitted sample depth profile. (b) Plot of modeled data, for fit in (a), and experimental data showing good agreement. Symbols correspond to the experimental data, and the lines are modeled data. (c) Optical properties determined from data.

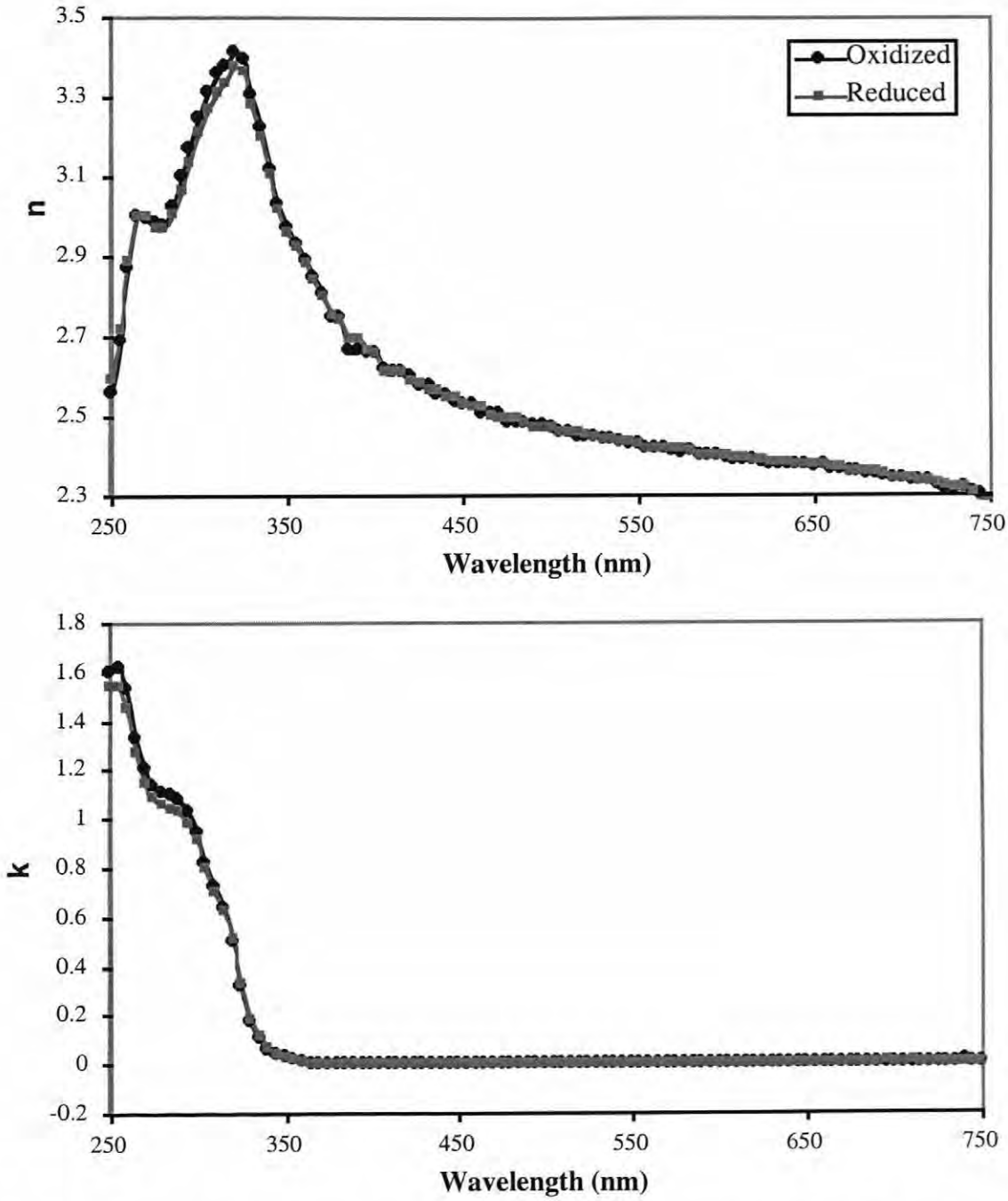

Figure 4–7: Optical property data for reduced and oxidized iron doped $SrTiO_3$ single crystal.

The optical data determined for iron doped $SrTiO_3$ were compared to reference data for $SrTiO_3$ from Cardona.[29] Since there are no reference data for iron doped $SrTiO_3$ the dielectric function of pure $SrTiO_3$ was used to ensure the data looked appropriate (*Figure 4–8*). This comparison shows the dielectric functions converge at low energies. The structure of the spectra is very similar, thus they have similar electronic structures even with the iron doping.

Throughout the remainder of the thesis, it was assumed that the impact of oxygen vacancies on the optical properties of the samples could be treated as a layer of reduced material. This is consistent with the reduction model of degradation, as described in Chapter 2.

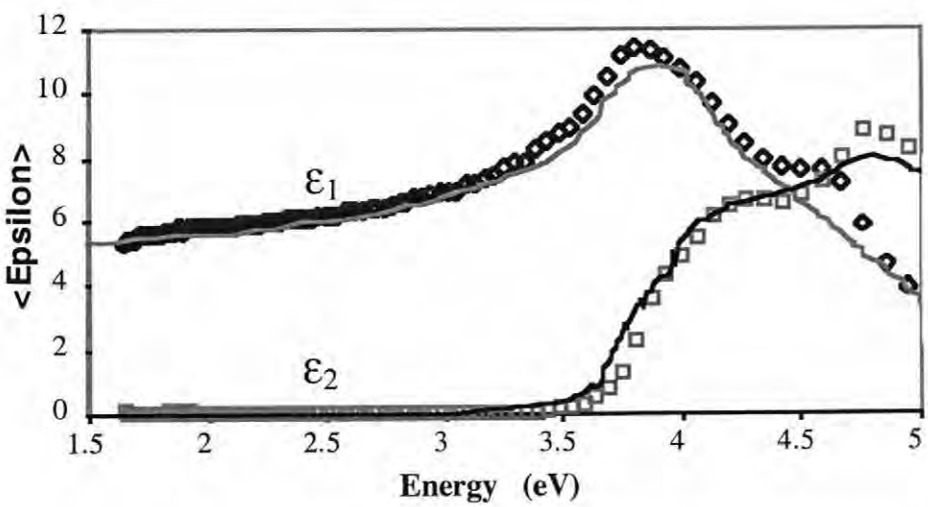

Figure 4–8: The complex dielectric functions for reference data (solid lines) determined by Cardona and data collected on iron doped $SrTiO_3$ samples (points). [31]

4.2 Modeling of SE Sensitivity to Discrete Reduced Surface Layers

In order to investigate the effectiveness of SE to monitor reduction in the samples, models with thin reduced surface layers were examined. The models were constructed for ideal samples without surface roughness. These models show the most ideal case where the sensitivity of SE would be the highest. These models also help determine the wavelengths at which surface reduction are best detected. The optical properties of the reduced and oxidized material determined in the previous section were used as reference data for the models.

To examine the sensitivity of spectroscopic ellipsometry two models were compared, one with a thin, reduced (high $[V_O^{\bullet\bullet}]$) layer on oxidized material, and a model of only bulk oxidized material (*Figure 4–9*). To calculate the sensitivity to surface reduction the difference in delta and psi for these two models were calculated using the following equations:

$$\partial\Delta = \Delta_{\text{Reduced Surface Layer}} - \Delta_{\text{No Surface Layer}} \qquad (4.1)$$

$$\partial\psi = \psi_{\text{Reduced Surface Layer}} - \psi_{\text{No Surface Layer}} \qquad (4.2)$$

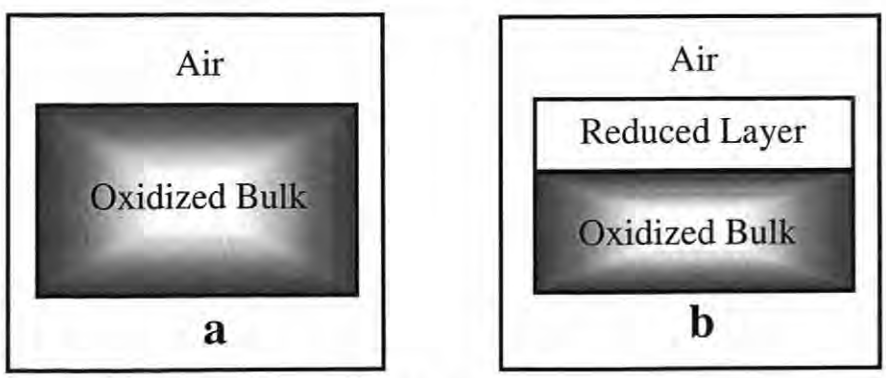

Figure 4–9: Model of samples used to calculate the sensitivity of spectroscopic ellipsometry to reduced surface layers. (a) virgin sample (b) partially reduced sample

With these calculations, a plot of the sensitivity of spectroscopic ellipsometry to surface reduction (or degraded) layers as a function of wavelength was created for two angles of incidence (70 and 80°). These data show the sensitivity of spectroscopic ellipsometry is highest in delta at approximately 325nm. For even a 4Å layer of reduced $BaTiO_3$ the change is 4.93° in delta at 325nm for an AOI of 70° (*Figure 4–10*). At an 80° AOI, further away from the Brewster's angle, the change was 0.32° in delta. This is smaller than the change at 70° (*Figure 4–11*), however the move away from the Brewster's angle should minimize experimental errors associated with AOI variances and low psi values.[24] Since the resolution of the measurements is 0.03° in delta and 0.01° in psi, the changes due to these surface layers are readily detectable.

The sensitivity of SE to a thin reduced layer of iron doped strontium titanate was calculated in the same manner as for barium titanate. The plot of the sensitivity of SE as a function of wavelength shows the sensitivity of spectroscopic ellipsometry is highest in delta at approximately 300nm. For even a layer of 4 Å of reduced iron doped $SrTiO_3$ the change is 1.88° in delta at 380nm for a 70° angle of incidence (*Figure 4–12).* With an angle of incidence of 80° the sensitivity decreases to 0.30°. Since the resolution of the measurements is 0.03° in delta and 0.01° in psi, the changes due to the degraded surface layer are still detectable. This sensitivity allows the monitoring of degradation associated with mobile oxygen vacancies in iron doped $SrTiO_3$ through SE.

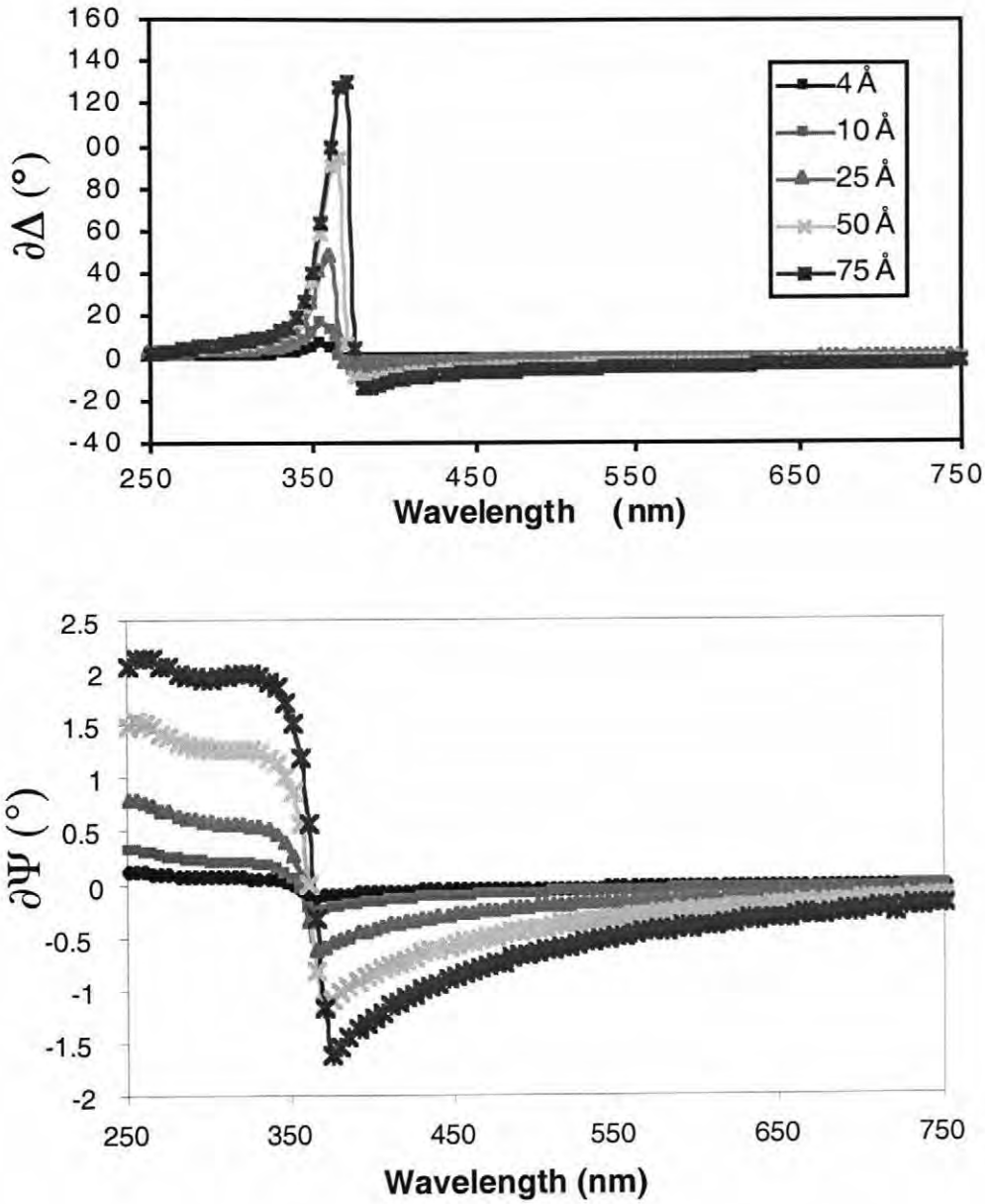

Figure 4–10: Modeled delta and psi data with different thicknesses of fully reduced $BaTiO_3$ on bulk $BaTiO_3$ at an AOI of 70°.

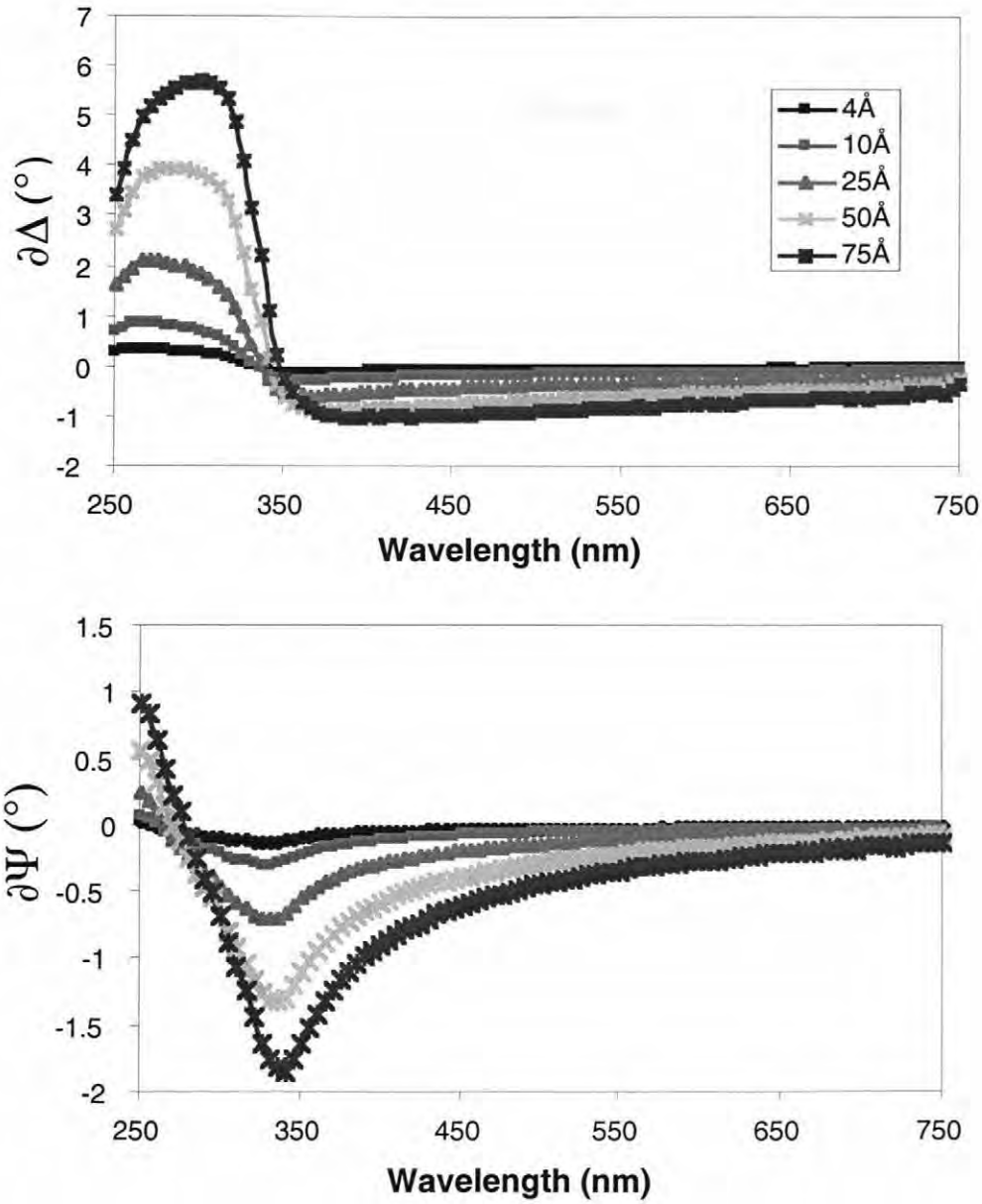

Figure 4–11: Modeled delta and psi data with different thicknesses of fully reduced $BaTiO_3$ on bulk $BaTiO_3$ at an AOI of 80°.

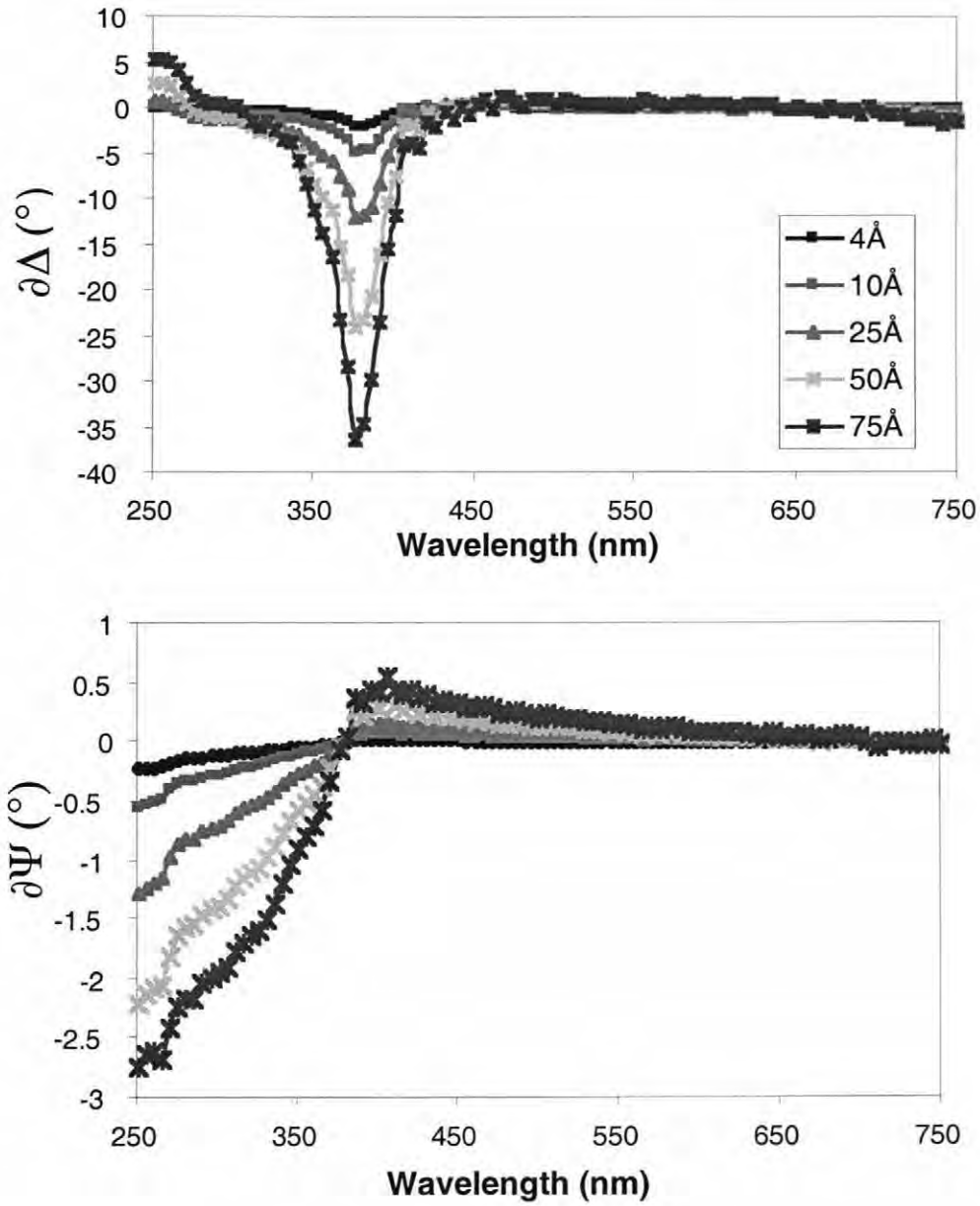

Figure 4–12: Sensitivity of SE to degraded surface layers of various thicknesses on iron doped $SrTiO_3$ at an AOI of 70°. The surface layer was fully reduced and the depth fully oxidized.

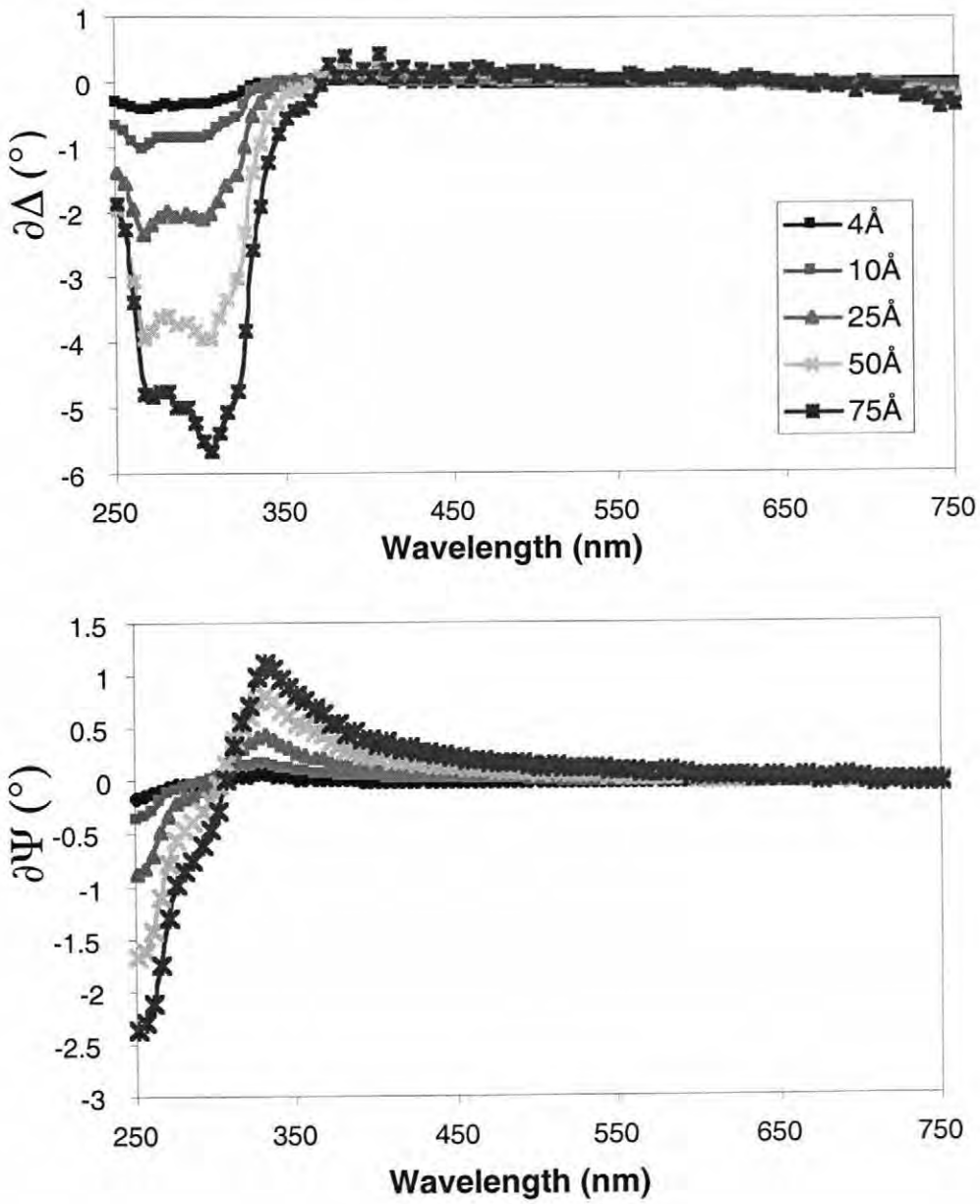

Figure 4–13: Sensitivity of SE to degraded surface layers of various thicknesses on iron doped $SrTiO_3$ at an AOI of 80°. The surface layer was fully reduced and the depth fully oxidized.

4.3 Modeling of SE Sensitivity to Concentration Gradients of Reduced Material

It is also important to determine the sensitivity of SE to a surface concentration gradient of $V_O^{\bullet\bullet}$ instead of a sharp interface. These models are more realistic representations of degraded layers in the material as found by previous work.[1,2,4,5,7,8,9] In this work, the concentration gradient was assumed to follow the shape of an error function (Equation 3.21). Here C_S and $\sqrt{Dt}$ were changed to model the effects of different surface compositions and gradient depth. (as described in Section 3.5).

It was found that for a concentration gradient with fully reduced surfaces, the sensitivity was high for 70° AOI, but much lower for an 80° AOI (*Figure 4–14, Figure 4–15*). The detectability at an AOI of 70° was 0.53° for a concentration gradient with a $\sqrt{Dt}$ of 10Å and a C_S of 1.0. However, at an 80° AOI the largest change in delta, 0.07°, is just detectable using spectroscopic ellipsometry. As expected, these changes are significantly smaller than for a model with a sharp interface. This is because the smaller change in the index of refraction across each of the layers does not cause as much reflection as a single large change in the index, as with a sharp interface.

A similar procedure was performed on $BaTiO_3$ to examine the changes with a graded surface layer (*Figure 4–16, Figure 4–17*). In both materials, the concentration gradient shows a smaller change in delta and psi than the discrete model. The models at 70° show a change of 3.93° for a $\sqrt{Dt}$ of 4Å. However the 80° AOI model shows a change of 0.21° for a $\sqrt{Dt}$ of 4Å. A small value, but still detectable by SE, providing the surfaces are smooth.

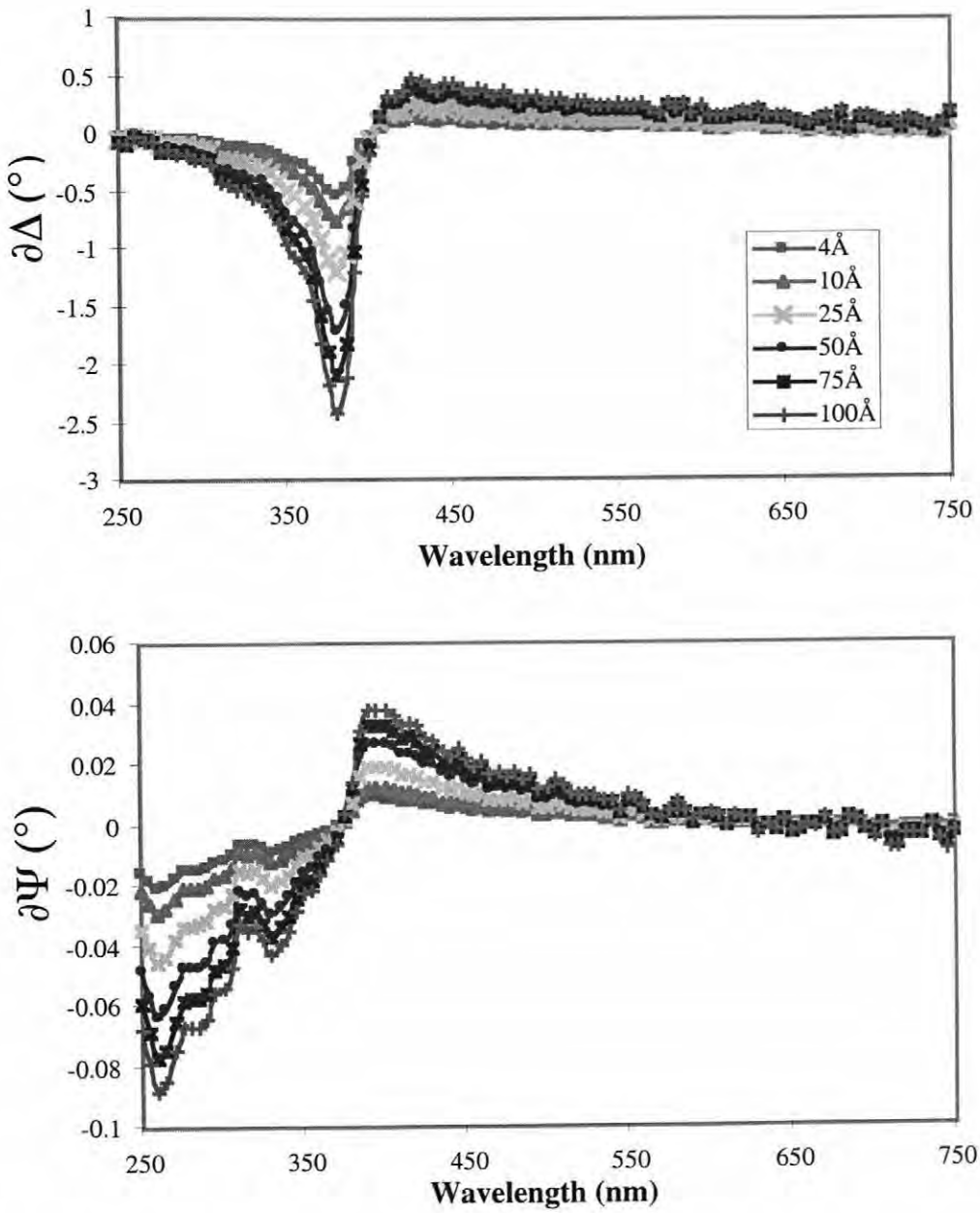

Figure 4–14: Changes in delta and psi for a concentration gradient of reduced material in iron doped $SrTiO_3$ with an AOI of 70°. This modeled data has a C_S of 1.0 and $\sqrt{Dt}$ was varied to find the sensitivity of SE to shallow concentration profiles. Legend gives $\sqrt{Dt}$.

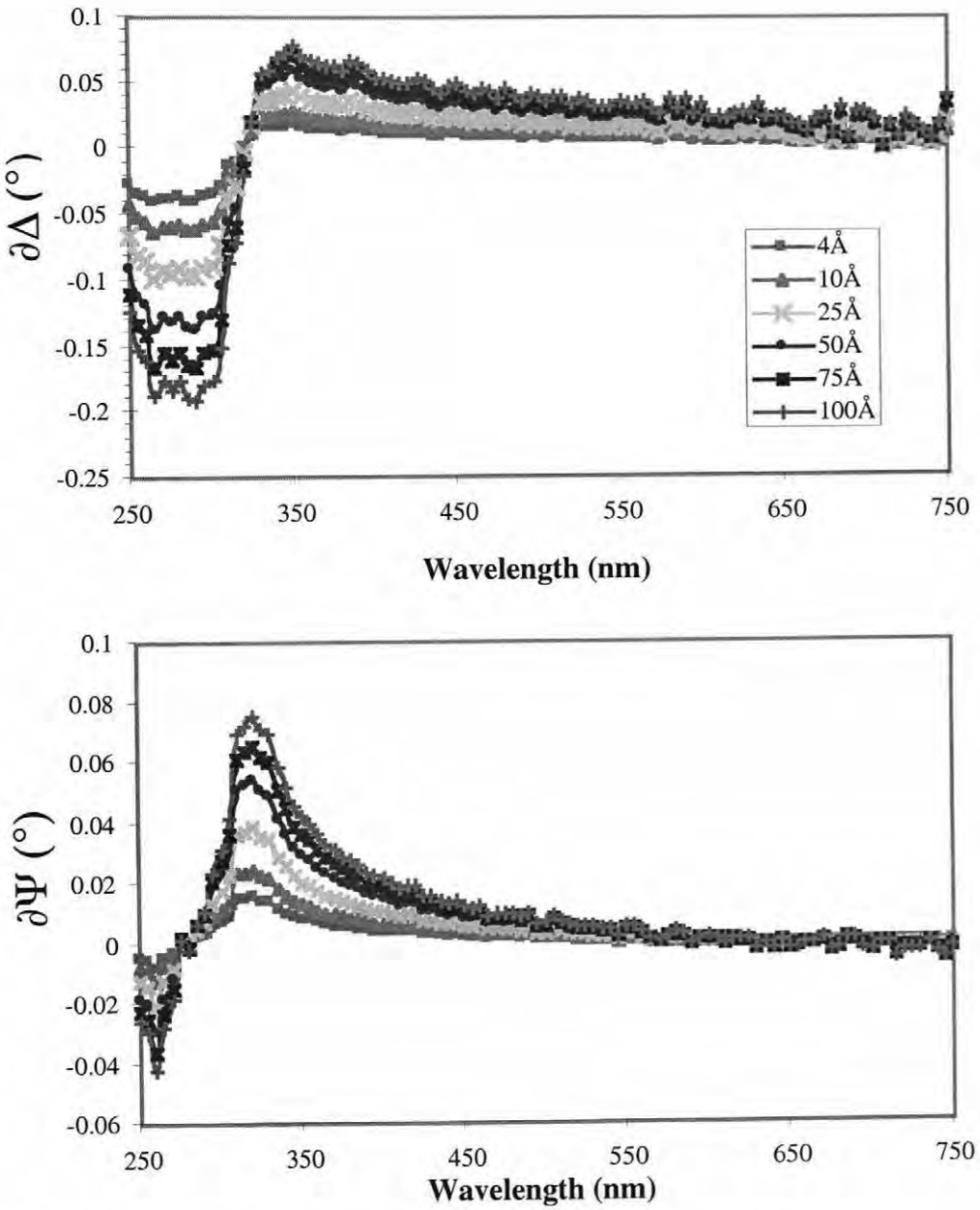

Figure 4–15: Changes in delta and psi for a concentration gradient of reduced material in iron doped $SrTiO_3$ with an AOI of 80°. This model was the same used in *Figure 4–14*. Legend gives √Dt.

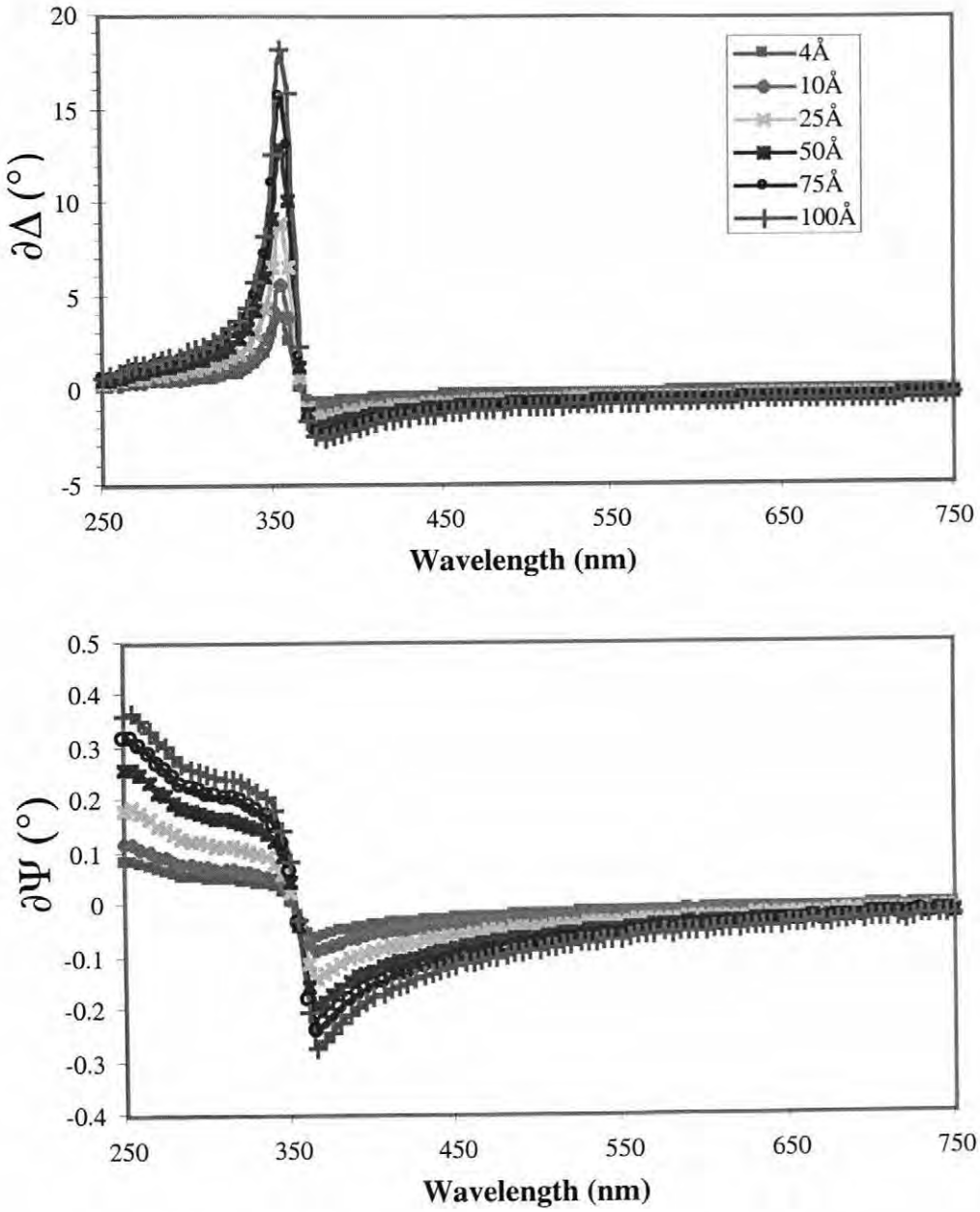

Figure 4–16: Changes in delta and psi for a concentration gradient of reduced material in $BaTiO_3$ with an AOI of 70°. This modeled data has a C_S of 1.0 and $\sqrt{Dt}$ was varied to find the sensitivity of SE to shallow concentration profiles. Legend gives $\sqrt{Dt}$.

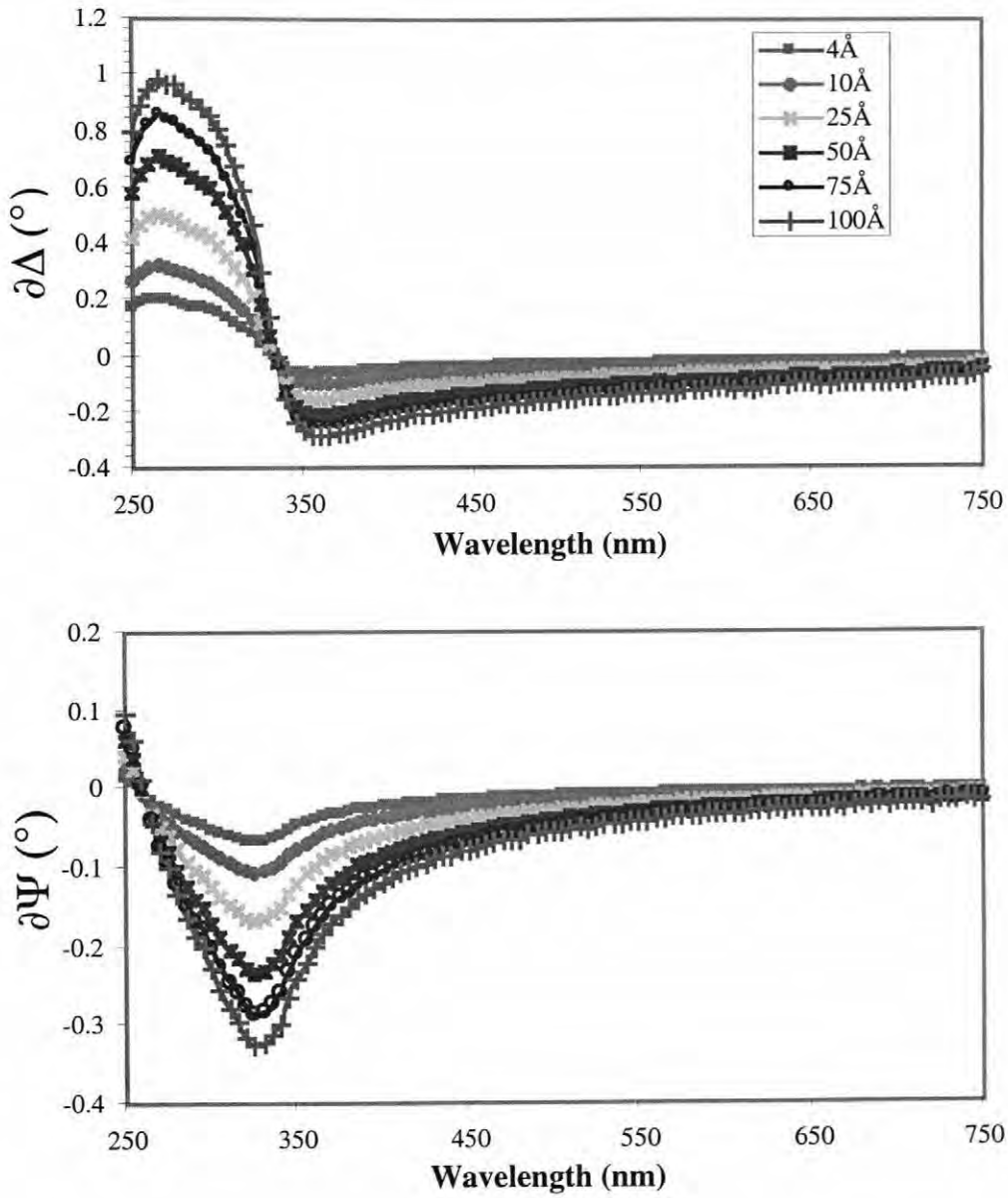

Figure 4–17: Changes in delta and psi for a concentration gradient of reduced material in $BaTiO_3$.This model was the same as used in *Figure 4–16* except with an 80° AOI. Legend gives √Dt.

The $BaTiO_3$ ceramic shows higher sensitivity to the degraded layers than the iron doped $SrTiO_3$. This can be attributed to the larger differences in the optical properties between reduced and oxidized states for $BaTiO_3$ than for iron doped strontium titanate.

The composition sensitivity of SE to graded layers was also examined. For these models the value of $\sqrt{Dt}$ was fixed at 10Å and the C_S was varied (*Figure 4–18, Figure 4–19*). These data show the accuracy with which the surface the concentration can be determined. For even shallow concentration profiles SE can detect very small changes in the composition on ideal samples. At an AOI of 70° a concentration gradient, with a $\sqrt{Dt}$ of 10Å and C_S of 1.0, ellipsometry could discern a change in composition of ~3% for $BaTiO_3$ and 10% for iron doped $SrTiO_3$. (The C_S of 100% refers to a fully reduced material on the surface) The high concentration resolution of SE allows for accurate depth profiling of these materials. However, at 80° AOI the sensitivity are decreased. For models with the $\sqrt{Dt}$ set at 100Å the sensitivity in Δ was limited to 3-5% for $BaTiO_3$ and 15-20% for iron doped $SrTiO_3$. These values will reduced the accuracy of the depth profiling at 80°. Consequently, to improve the sensitivity to degraded surface layers, it will be important to work near the Brewster's angle.

To better understand the resolution of SE in the real world, a $[V_O^{\cdot\cdot}]$ concentration gradient was modeled for both $BaTiO_3$ and iron doped $SrTiO_3$ samples with roughness layers of 40Å, with the volume fraction of air fixed at 50%. The roughness significantly reduces the detectability of reduced surface layers. The maximum change in delta decreases from 18° to 0.5° for $BaTiO_3$ with a $\sqrt{Dt}$ of 100Å (*Figure 4–20*) for an AOI

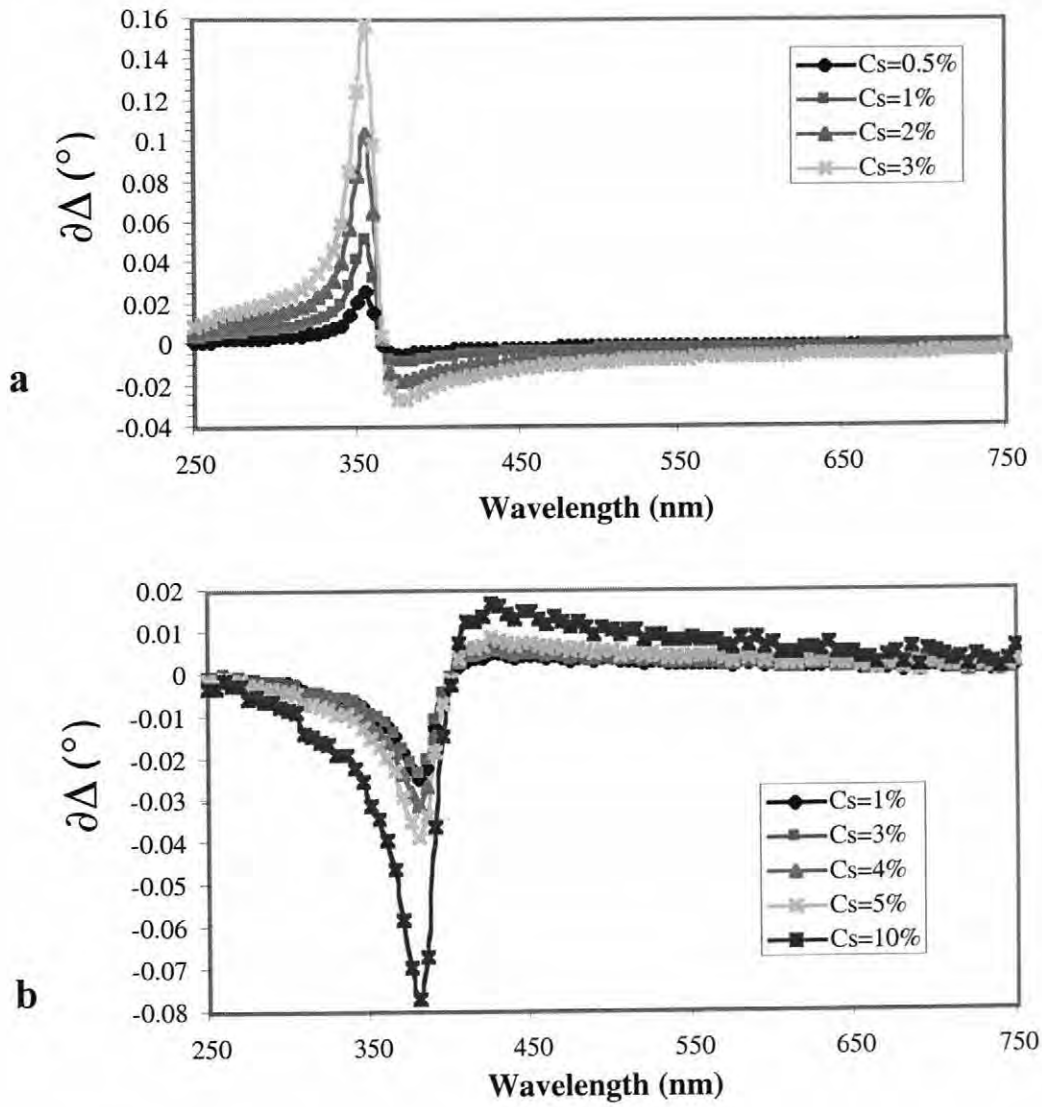

Figure 4–18: Change in delta due to differences in C_S with $\sqrt{Dt}$ held at 10Å for (a) $BaTiO_3$ and (b) iron doped $SrTiO_3$. Angle of incidence is 70°

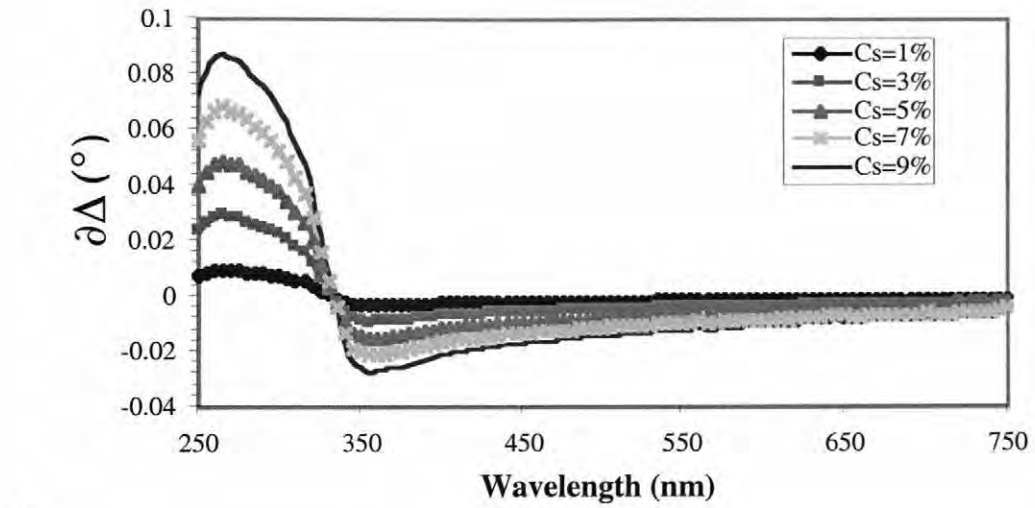

a

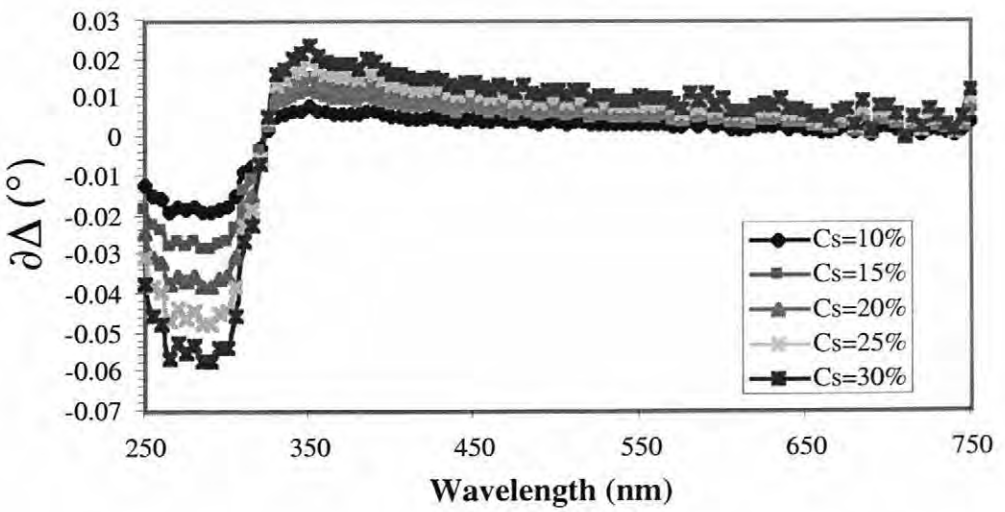

b

Figure 4–19: Change in delta due to differences in C_S with $\sqrt{Dt}$ held at 100Å for (a) $BaTiO_3$ and (b) iron doped $SrTiO_3$. Angle of incidence is 80°.

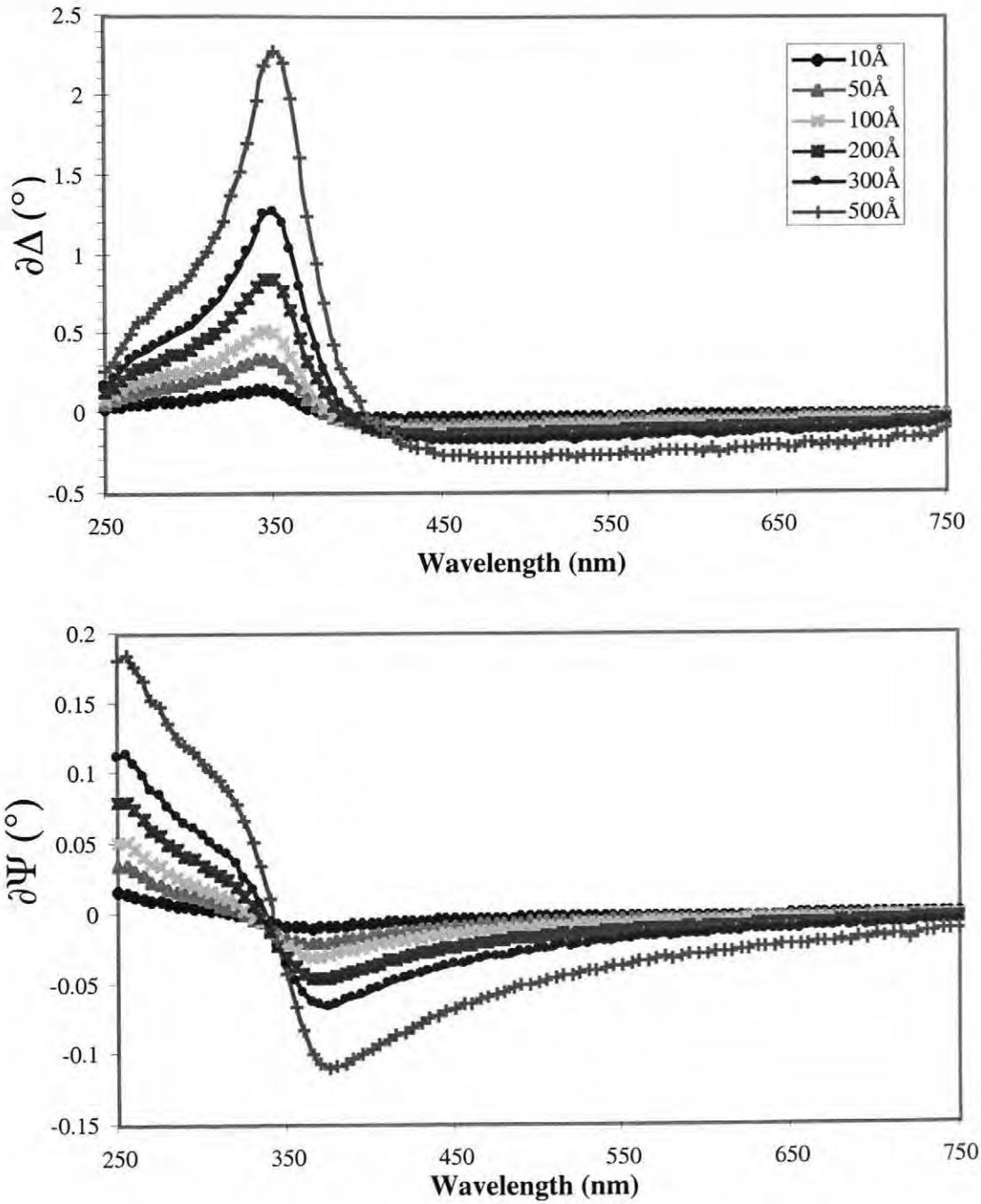

Figure 4–20: Changes in delta and psi for a graded layer of reduced material on $BaTiO_3$ with a 40Å roughness layer of 50% air and 50% reduced $BaTiO_3$ at an angle of incidence of 70°. This model changed $\sqrt{Dt}$ while C_S was held at 1.0.

of 70° and from 1.0° to 0.12° with an AOI of 80° (*Figure 4–21*). The gradient is readably detectable at 70° AOI, but is not easily detected at 80° AOI. This change was similar in the iron doped $SrTiO_3$ with a 100Å layer the maximum sensitivity decreased from 2.5° to 0.08° in delta for 70° AOI (*Figure 4–22*) and 0.18° to 0.02° for an AOI of 80° (*Figure 4–23*). At 70° AOI the gradient is still detectable, but verges on the resolution of the ellipsometer. However, at 80° AOI the $\sqrt{Dt}$ must increase to at least 200Å before it can be detected.

To show the sensitivity limits of SE to iron doped $SrTiO_3$ and $BaTiO_3$ a map was created (*Figure 4–24*, *Figure 4–25*). These maps show the limit at which the change in psi and delta could be detected. The limits of detectability were set for the maximum sensitivity of the ellipsometer, which was 0.03° in delta and 0.01° in psi. A roughness layer of 40Å was also used to make the models more realistic. These maps show that the sensitivity is high for both materials and should be readily detectable in most situations at 70° AOI. At 80° AOI the sensitivity lower than for an AOI of 70° for delta but is similar for psi. For iron doped $SrTiO_3$ at an AOI of 80° the models suggest the ellipsometry can not resolve concentration gradients with a C_S less than 3%. As expected, with shallower concentration gradients the surface must be more reduced for SE to detect the changes. The map also shows the limits of resolution of concentrations. With deeper concentration gradients the surface concentration can be determined with more accuracy.

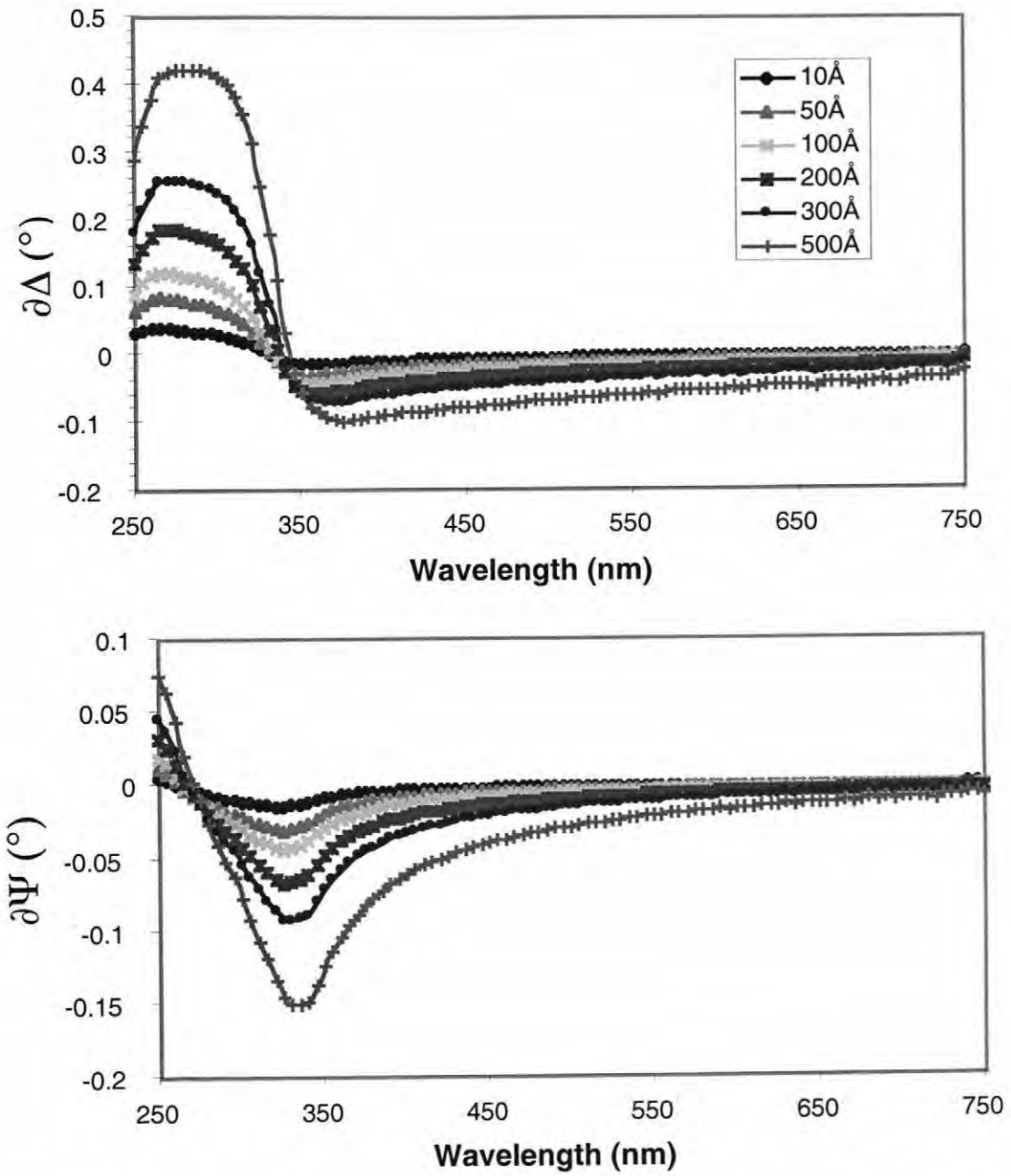

Figure 4–21: Same modeling procedure for $BaTiO_3$ as used for *Figure 4–20* except with an AOI of 80°.

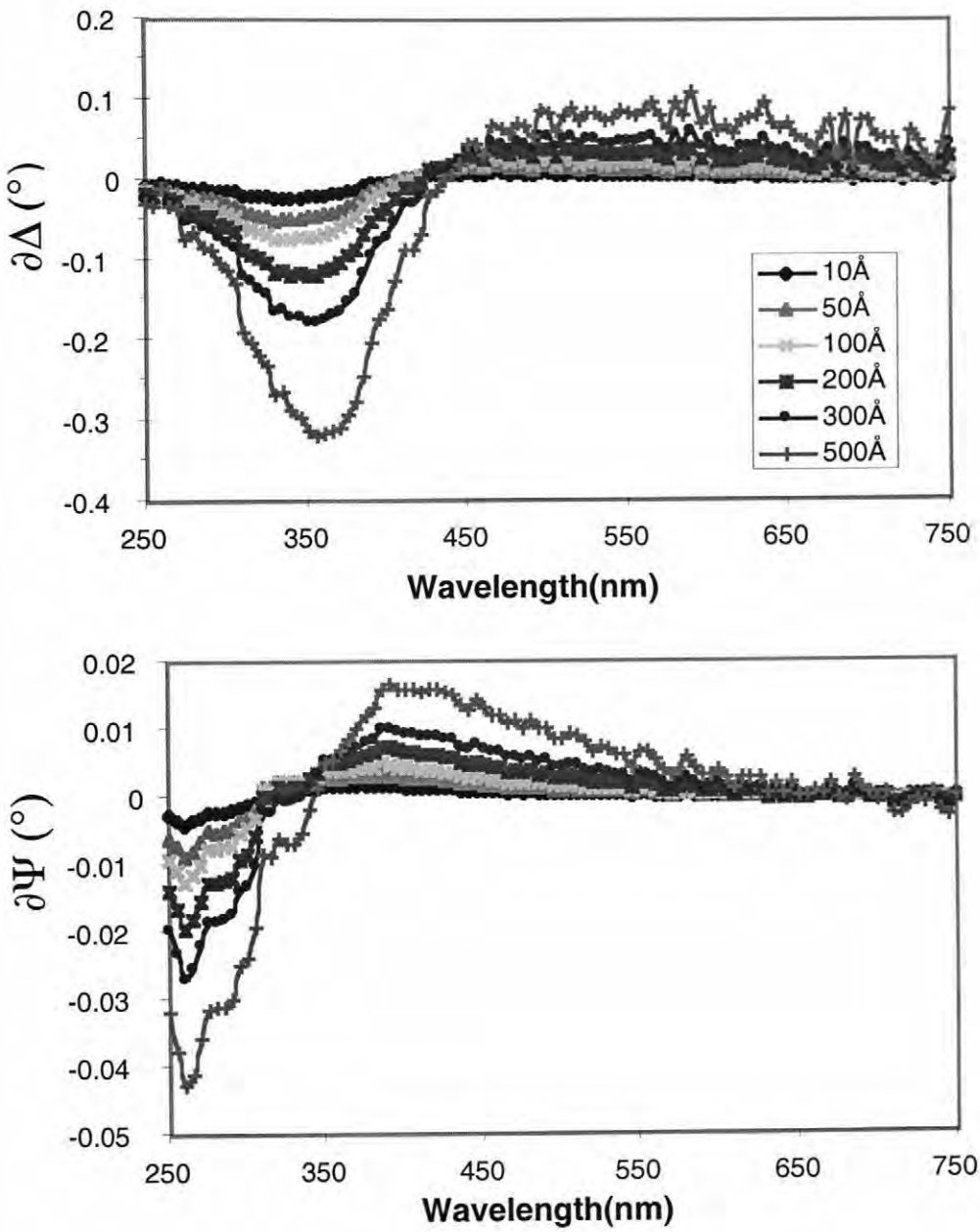

Figure 4–22: Changes in delta and psi for a concentration gradient of reduced material in iron doped $SrTiO_3$ with a 40Å roughness layer (of 50% air and 50% reduced iron doped $SrTiO_3$). These models use and angle of incidence of 70°.

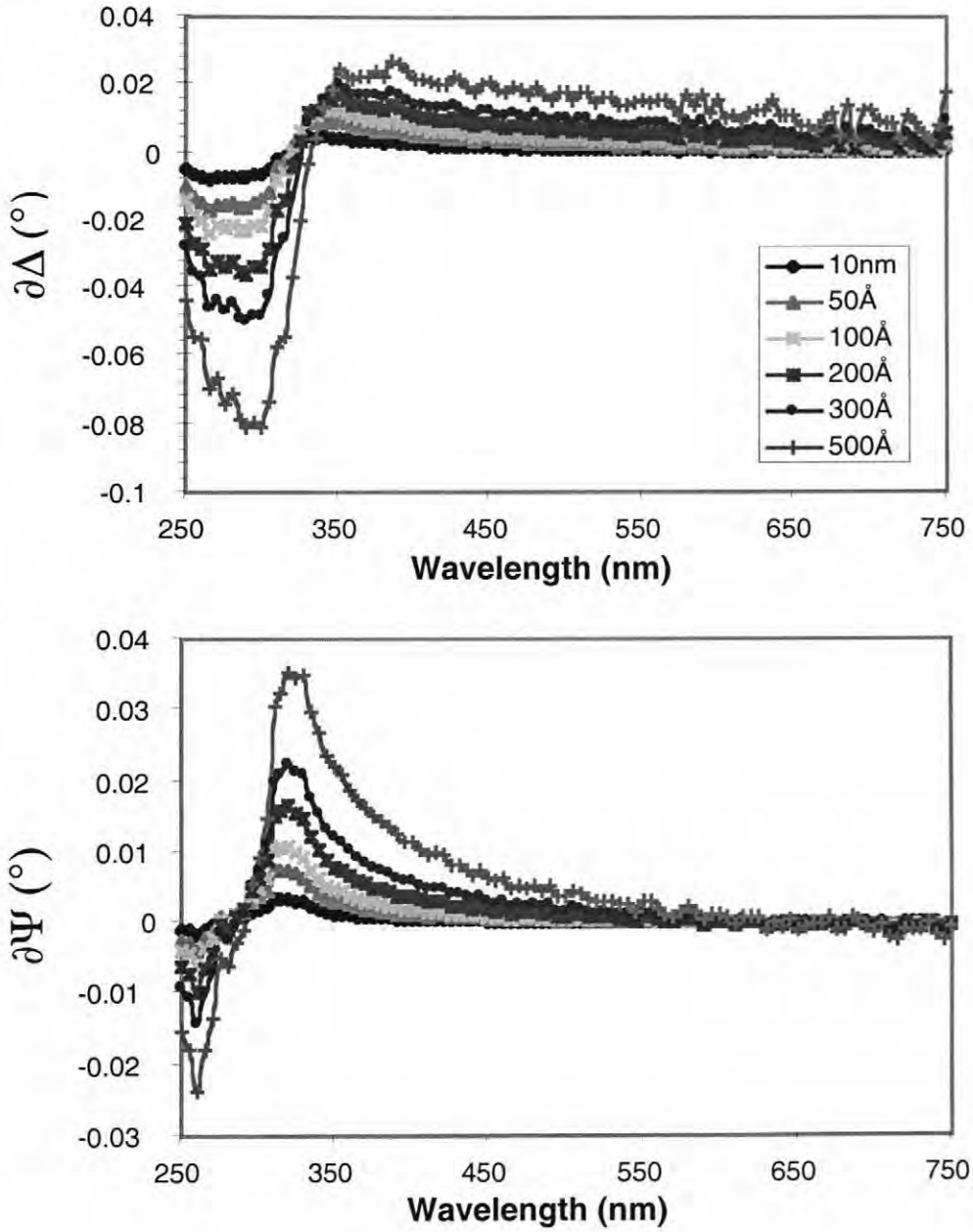

Figure 4–23: Changes in delta and psi for a concentration gradient of reduced material in iron doped $SrTiO_3$ for the same model used for *Figure 4-22* except with an AOI of 80°.

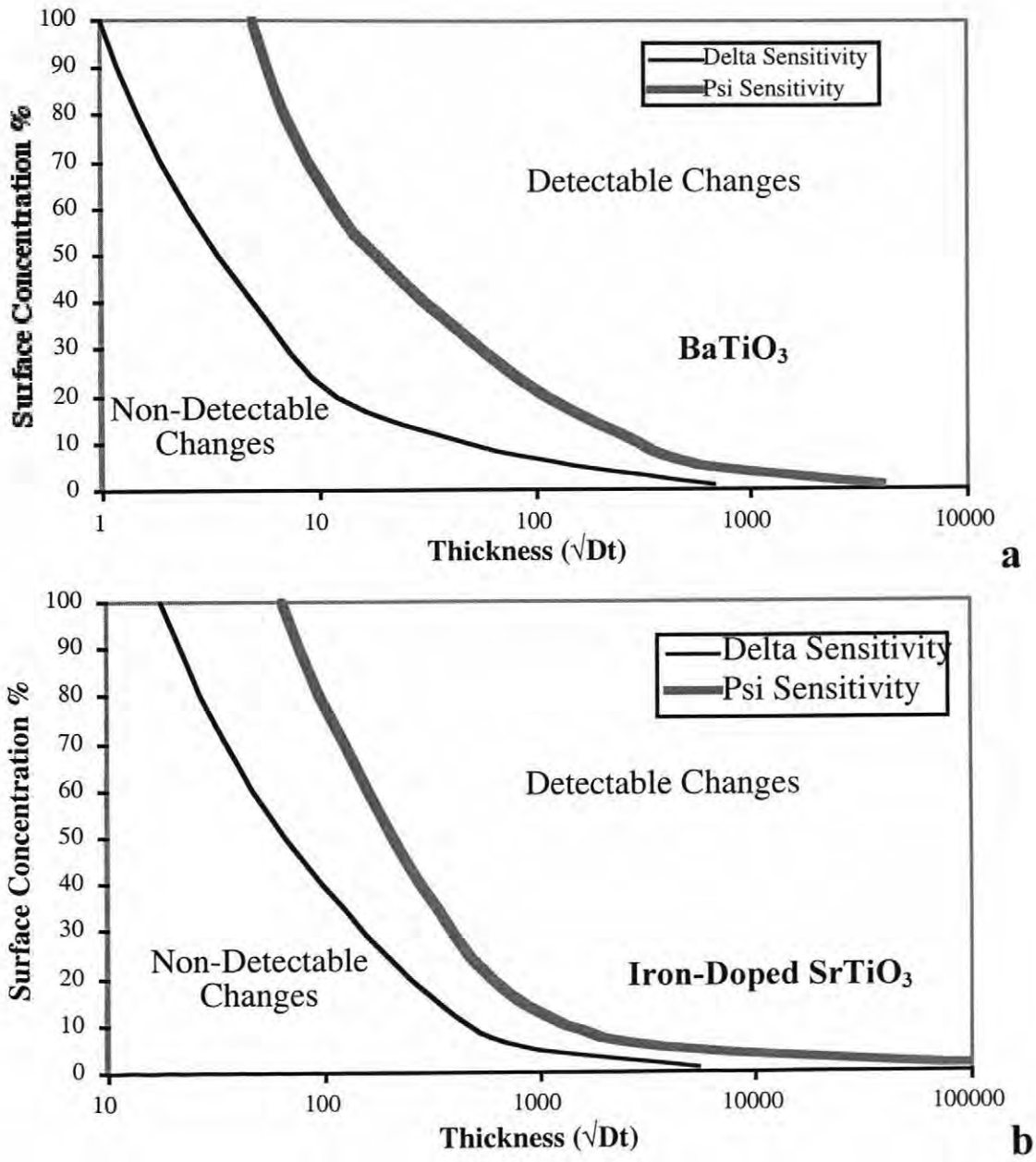

Figure 4–24: Sensitivity maps showing the sensitivity limits of SE to a concentration gradient of degraded material for (a) $BaTiO_3$ and (b) iron doped $SrTiO_3$ at 70° AOI.

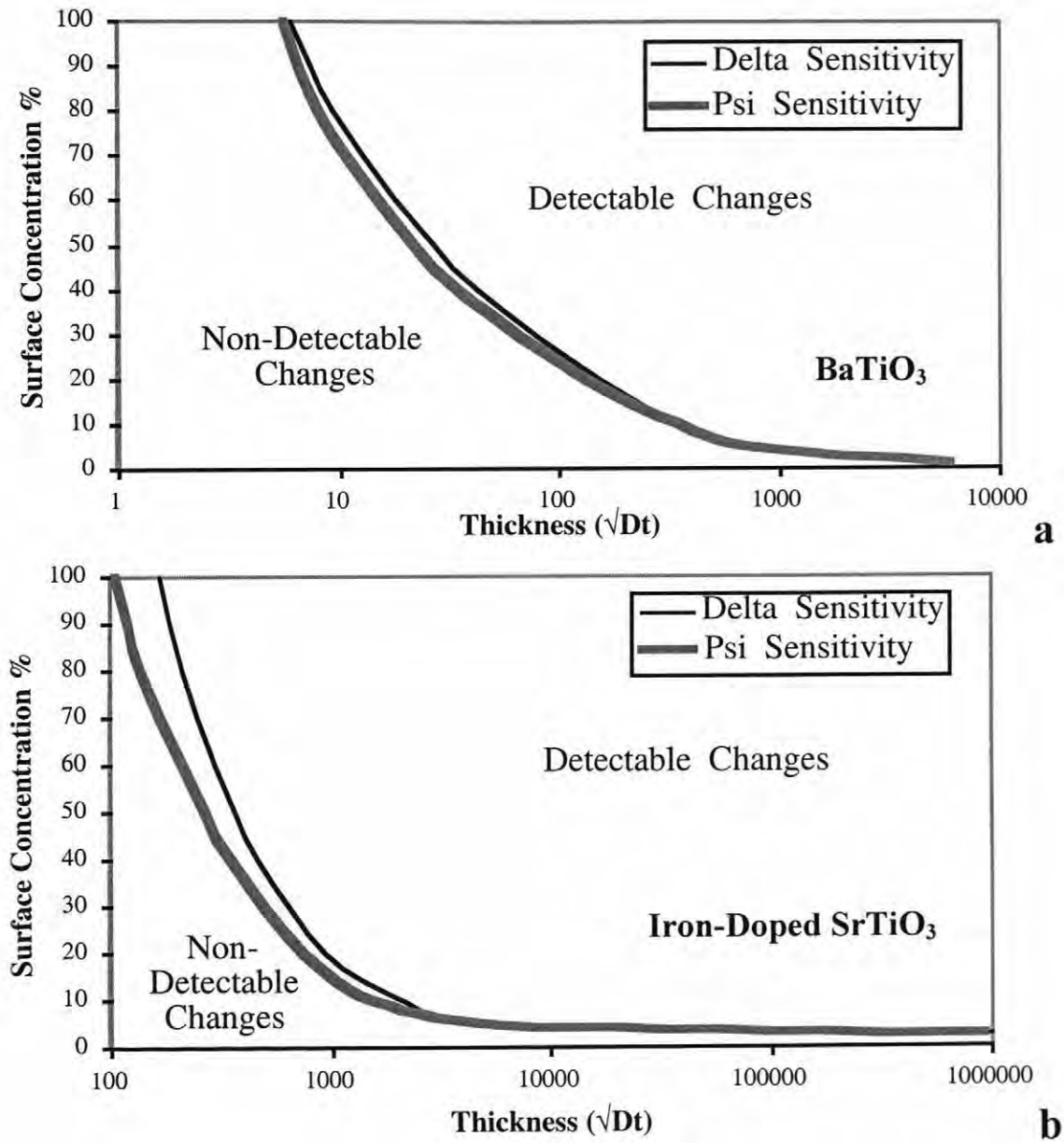

Figure 4–25: Sensitivity maps showing the sensitivity limits of SE to a concentration gradient of degraded material for (a) $BaTiO_3$ and (b) iron doped $SrTiO_3$ at 80° AOI.

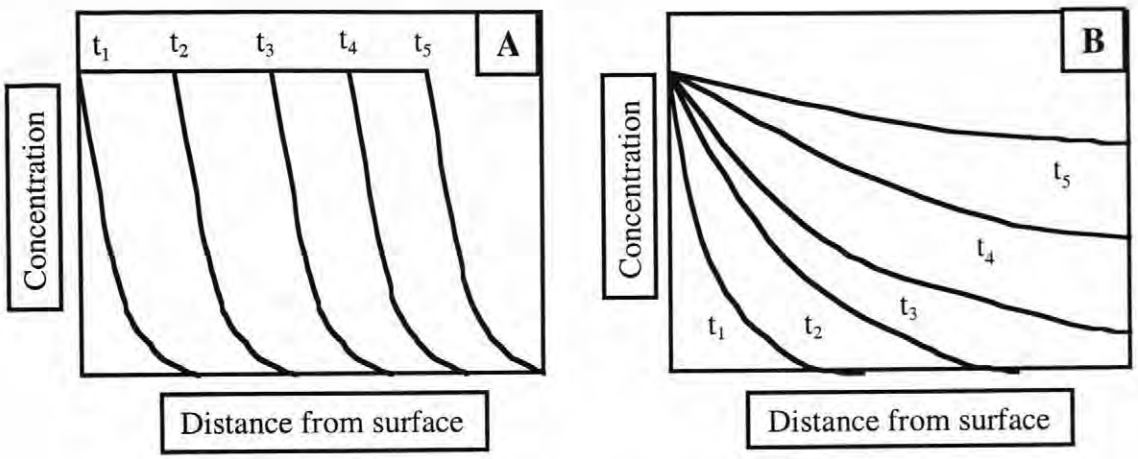

Figure 4–26: Schematic of two degradation models. (A) discrete model (B) concentration gradient model. Time is increasing from t_1 to t_5.

4.4 Delta-Psi Trajectories for Accumulation of $V_O^{\cdot\cdot}$ Near the Surface

A color front associated with changes in the oxygen content, moves through the material from the cathode when a dc bias is applied. To examine how the optical properties would change as a result of different concentration profiles a delta-psi trajectory was created. These models were examined at 350nm to maximize the sensitivity to changes in the oxygen content.

Two models were calculated to determine how the optical properties change (*Figure 4–26*). The difference between the behavior of these models should allow for the determination of how the oxygen vacancies move through the material. The first model describes the concentration gradient created by rapid diffusion through grains boundaries with slower diffusion through the grains (*Figure 4–26*A). This mechanism was treated by

using a layer of fully reduced material over a shallow concentration gradient to fully oxidized material. The second model represents diffusion through the grains and was approximated by a concentration gradient following an erf function (*Figure 4–26*B). These two scenarios show different delta-psi trajectories as a function of time due to the difference in the depth profile of the optical properties (*Figure 4–27, Figure 4–28*). In the models the initial state was the same: fully oxidized materials. The models also converge to the same point: fully reduced material over the optical penetration depth. Though the initial and final states were the same for the models the paths between these states are different. When a constant surface concentration of different thickness is assumed, the calculation shows interference fringes as time progresses. In contrast, the concentration gradient model shows a smoother transition to the final state. The major difference for the 70° AOI and 80° AOI is the wavelength that the model was examined. The wavelength of maximum sensitivity to changes (determined above) was used for both models but this wavelength was shorter for the 80° AOI models. At these shorter wavelengths the material was much more absorbing, therefore there are fewer interference fringes.

These trajectories can also be used to determine the depths at which SE can no longer distinguish between a fully reduced sample and a sample with a concentration gradient of reduced material. In iron doped strontium titanate this limit is reached when the concentration gradient reaches a $\sqrt{Dt}$ of 200μm for an AOI of 70° and 100μm for an 80° AOI. The discrete model appears fully reduced when the front reaches 40μm and 10μm for an AOI of 70° and 80°, respectively. For $BaTiO_3$ at an AOI of 70° the final

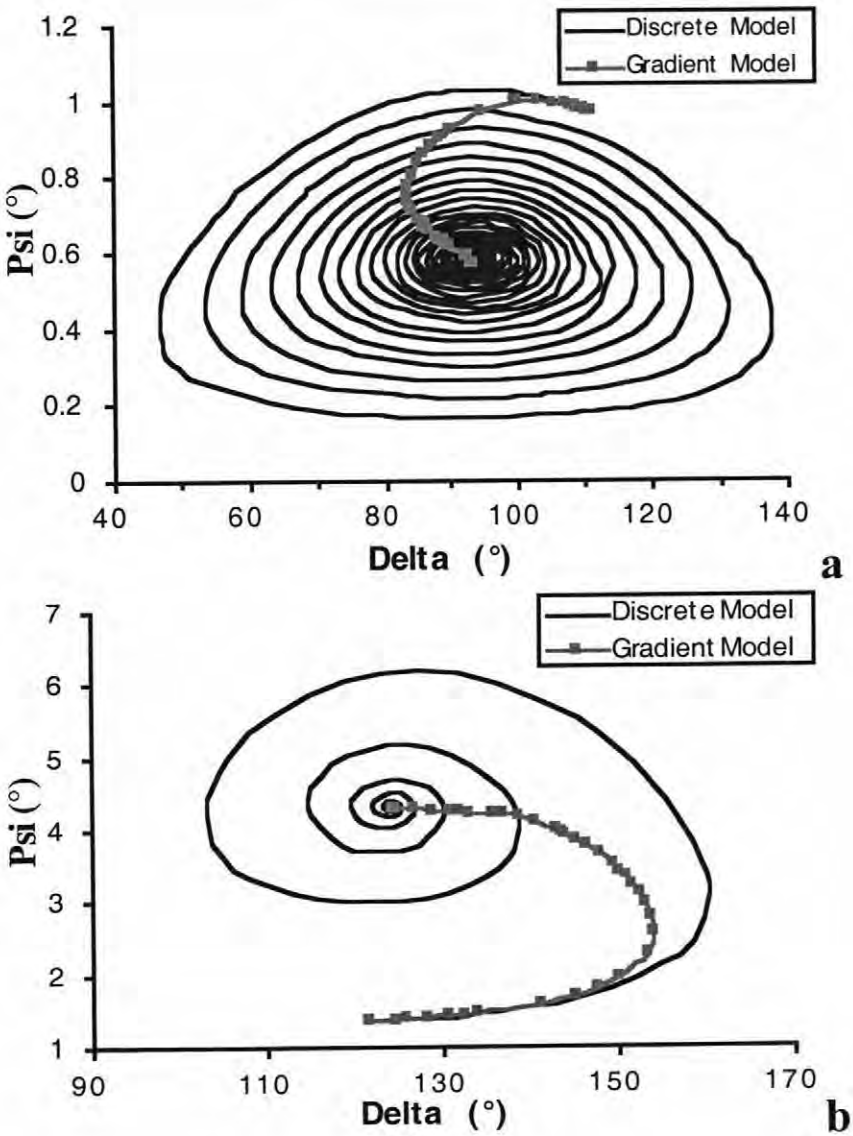

Figure 4–27: Delta-Psi trajectories for discrete and concentration gradient models. (a) iron doped strontium titanate (b) barium titanate. Wavelength was 350nm for $BaTiO_3$ and 380nm for iron doped $SrTiO_3$. Angle of incidence = 70°.

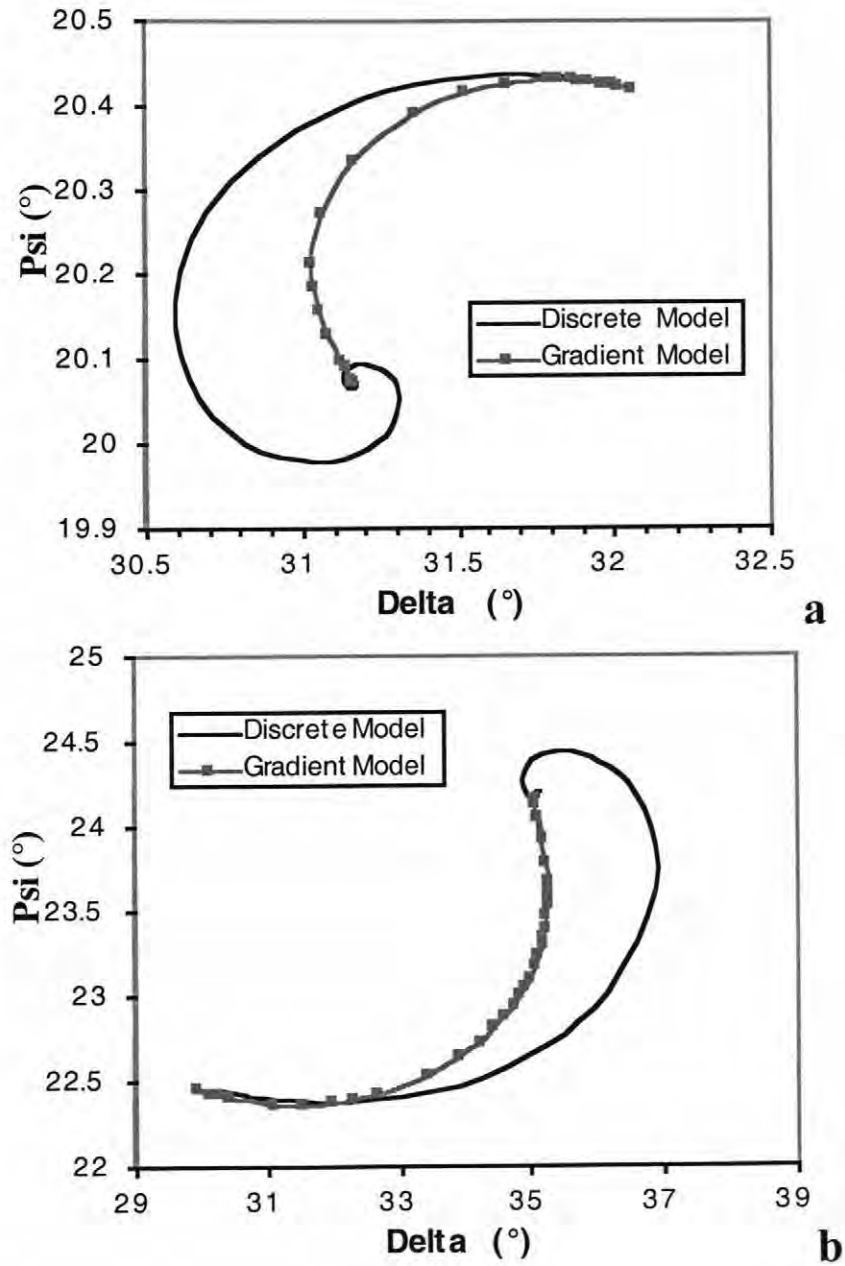

Figure 4–28: Delta-Psi trajectories for discrete and concentration gradient models. a) iron doped strontium titanate b) barium titanate. The models were examined at 265nm for $BaTiO_3$ and 290nm for iron doped $SrTiO_3$. Angle of incidence = 80°.

stage corresponds to a depth of 100μm for the concentration gradient and 5μm for the discrete model. With an AOI of 80° the final stage is reached at 90μm and 1μm for the concentration gradient and discrete model respectively. In practice, these numbers will probably be considerably smaller due to the short coherence time for the light from the Xe source.[24] In both materials the method of degradation front progression should be able to be differentiated by SE as a result of these differences.

Chapter 5

MONITORING ELECTRIC FIELD INDUCED DEGRADATION

The purpose of these experiments is to track dc field induced degradation in capacitor materials via spectroscopic ellipsometry. Optical measurements can be used to follow the changes in barium titanate and iron doped strontium titanate due to the electrocoloration during the degradation process. Samples were heated to 130-150°C to accelerate the degradation under a dc electric field of 1.25-1.35kV/cm. It was found that the $BaTiO_3$ ceramic did not degrade uniformly on the surface; rather it degraded in small areas due to the grain structure. This complicated spectroscopic ellipsometry measurements due to the low lateral resolution of several square millimeters. To rectify this situation, single crystals of iron doped $SrTiO_3$ were investigated. This material did not exhibit the localized degradation and allowed for uniform degradation on the sample surface.

5.1 *In-situ* Degradation

Iron doped $SrTiO_3$ single crystal (100) samples were mounted on a vertical hot-stage on the ellipsometer using silver paint. The samples were electroded with sputter deposited thin platinum electrodes on the front, and thick Pt electrodes on the back. The

samples were aligned on the ellipsometer and heated to 130 to 150°C. A 1.25kV/cm or 1.35kV/cm dc field was applied to the sample., using a PS350 Princeton electric power supply. Contact was made to the sample by lowering an electrode to the surface of the sample. A negative voltage was applied to the surface of the sample and the back of the sample was grounded. This was done because larger changes were found at the cathode of the samples than at the anode. The samples were held at temperature and dc field until the leakage current increased to 4.0mA. This limit was imposed to prevent permanent degradation of the sample.

5.1.1 Semitransparent Pt Electrode

In-situ monitoring of degradation by SE required that light be transmitted through the electrode. Thin Pt electrodes were sputter deposited, at 0.05mbar and a current of 63mA, to create a very thin electrode that could transmit light. This was tested on glass samples. Figure *5–4* shows delta and psi as a function of wavelength with samples of glass that have Pt layers of different thickness. The data was accurately modeled using a model with several layers: a layer of mixed Pt and glass was used to account for the roughness of the glass, a layer of Pt, and a layer of Pt and air to account for surface roughness of the Pt (*Figure5–2*). This model was able to predict the experimentally determined tan(Δ) and tan(Ψ) to within 0.001-0.002 (*Figure 5–3).* This accuracy is, approximately, the limit of the ellipsometer. The thickness of the sputtered Pt electrodes is shown in Table *5–1*. It can be seen that the uncertainty in the Pt thickness increases with increasing electrode thickness.

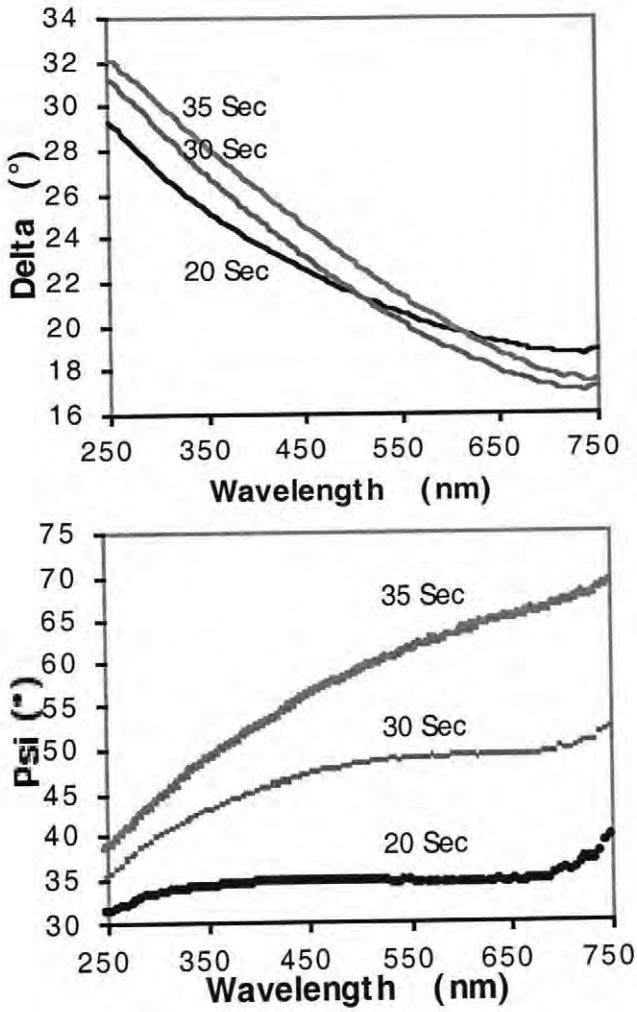

Figure 5–1: Spectroscopic ellipsometry data for Pt electrodes for various sputtering times on soda lime glass. Samples were measured at 70° angle of incidence.

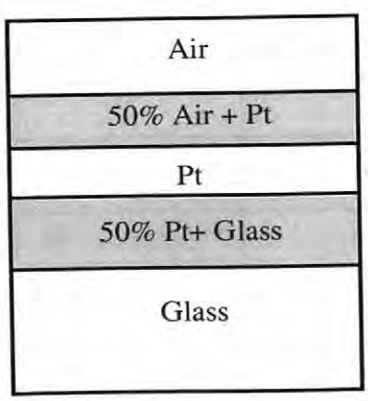

Figure 5–2: Schematic used for modeling of Pt on soda lime slica glass.

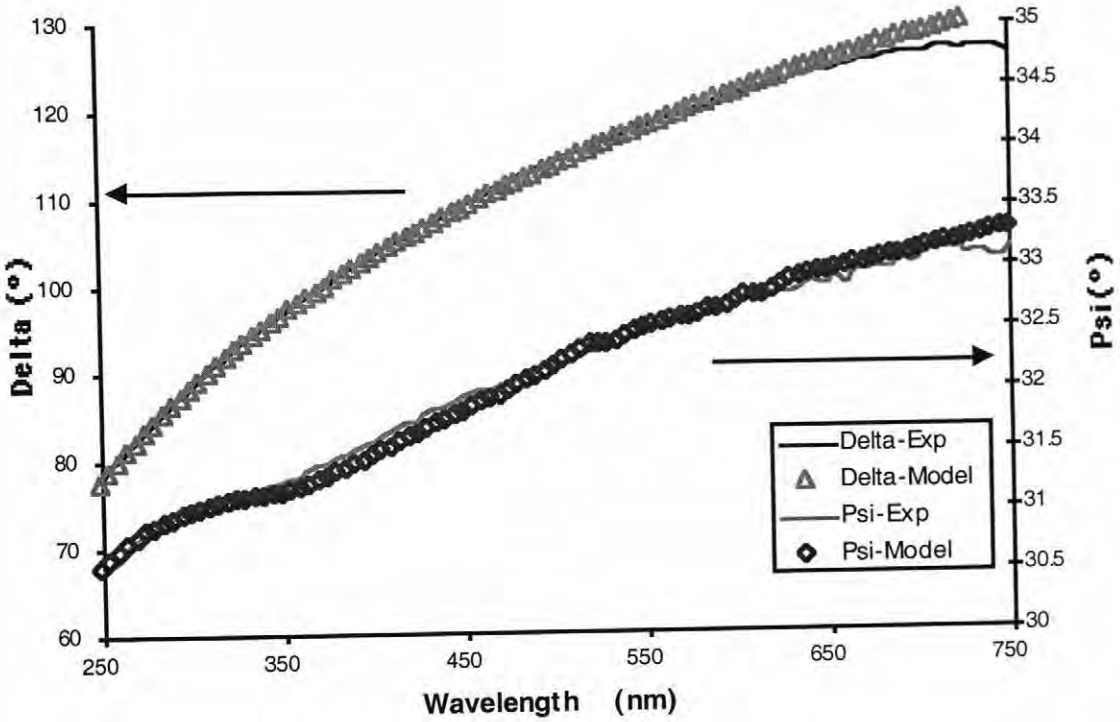

Figure 5–3: Plot of modeled and experimental data for Pt on glass showing the accuracy of the model.

Table 5–1: Thickness of Pt electrode for different sputtering times.

Sputtering Time (sec)	Pt Thickness (Å)
15	104 ± 54
20	168 ± 67
30	243 ± 83
35	390 ± 110

It was found that the effective optical properties of the Pt electrodes change during degradation, probably due to morphology changes. This reduces the sensitivity of the ellipsometer to concurrent changes in the dielectric and adds error to the data interpretation. To reduce the error and maximize the sensitivity to dielectric degradation, 100Å, 160Å, 240Å thick platinum electrodes were examined. The electrodes were heat treated at 250°C for 1h before the experiment to help stabilized the electrode. The samples were mounted on the hot stage in the ellipsometer using silver paint and heated to 130°C at a ramp rate of 2.0°C/min. Ellipsometric data were collected every 30min for a period of 3h to monitor changes in the electrode (*Figure 5–4*).

A major change in these electrodes at 130°C is the roughness. There is an initial change in the electrode as it is heated to 130°C from room temperature. This causes the delta and psi curves to move up. The thinner electrodes have smaller time dependence of

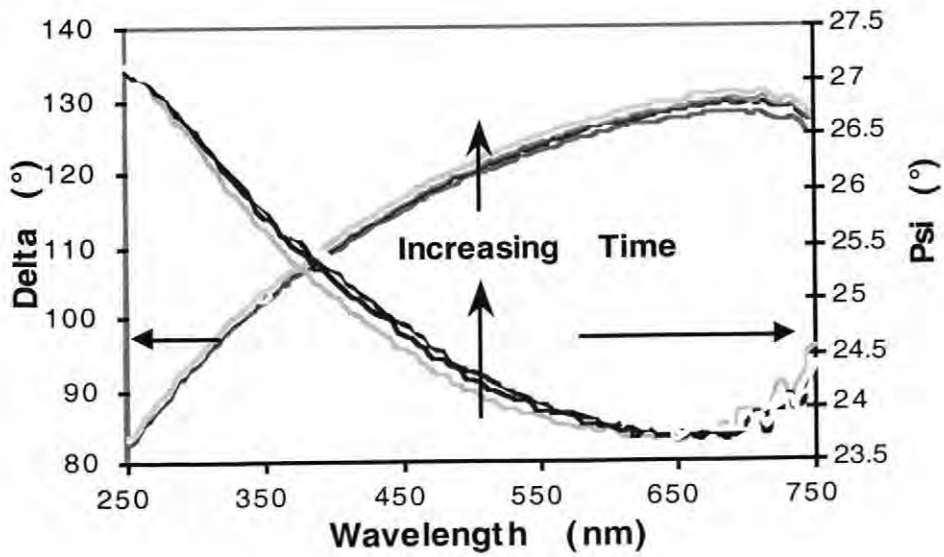

Figure 5–4: Changes in delta and psi as a function of time during an anneal at 130°C for 160nm thick Pt electrode on glass. The changes are associated with changes in roughness. After 1h the sample changes very little.

the ellipsometric parameters delta and psi during an anneal and are more transparent. This makes the thinner electrodes better for use in the degradation study. The initial changes that occur on heating to initial changes are less than 0.5° and quickly reduce to less than 0.05°, after 1h. This is close to resolution limit for the ellipsometer. The 160nm electrode has larger changes initially but does converge to the same changes of approximately 0.05°. The stabilization suggests that the samples should be allowed to stabilize at 130°C for at least 1h before electrical degradation is initiated.

5.1.2 Degradation Under Pt Electrodes

An iron doped strontium titanate single crystal was covered with thin Pt electrodes and degraded (see Chapter 3 for setup). The sample was degraded under a dc electric field of 1.25 kV/cm and a temperature of 130°C. Thin platinum electrodes were used to apply the field. The sensitivity through the platinum electrodes was less than for the calculated sensitivity for degraded crystals (see Chapter 4). However, the change due to degradation was detectable. The changes in psi show an increase with time until a rapid degradation started. This corresponds well to an increase in the current (*Figure 5–5*). The onset of rapid degradation is also reflected in the rapid change in the optical properties. The data shows that spectroscopic ellipsometry is sensitive enough to detect degradation.

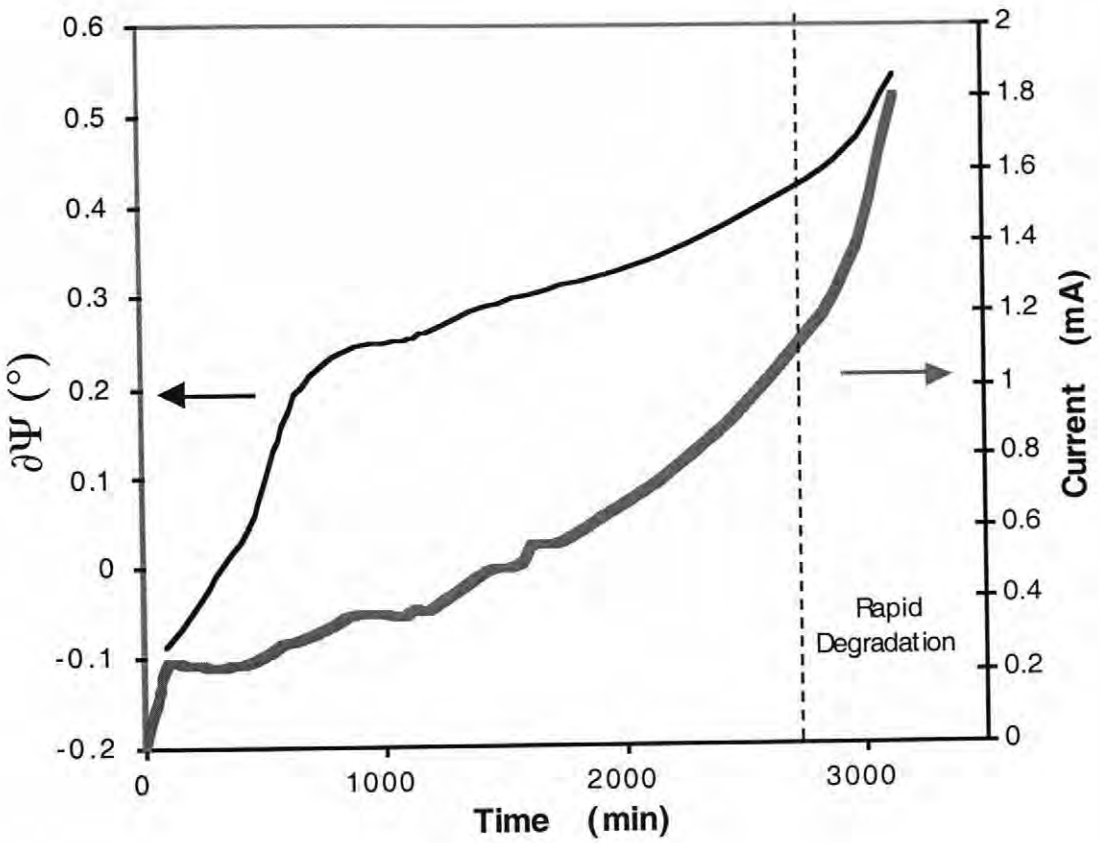

Figure 5–5: Cumulative change in Psi at λ=380nm and increase in current at 130°C under 1.25kV/cm E-field for an iron doped $SrTiO_3$ single crystal. Measured with an angle of incidence of 80°.

Unfortunately it was very difficult to obtain run to run repeatability in the measurements. This is probably due to a combination of variability in the Pt electrodes, electrode stability, and light absorption in the top electrode. As a result, the SE data collected during *in-situ* degradation under a dc electric field did not enable extraction of a diffusion coefficient for oxygen vacancies. Figure *5–6* shows the modeled results on the sensitivity of SE to reduced surface layers with a 200Å thick electrode. It can be seen

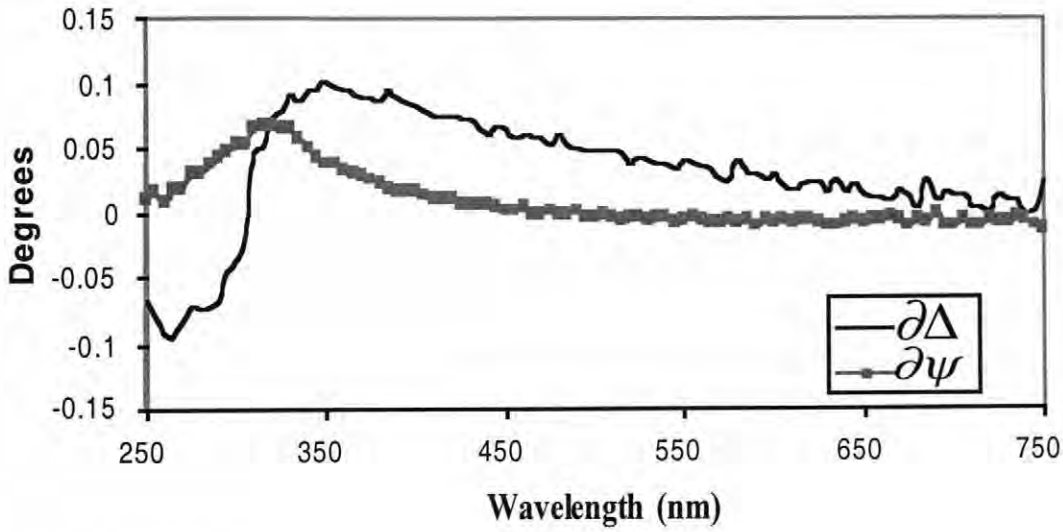

Figure 5–6: Modeled sensitivity of SE to a 100Å reduced layer in barium titanate under a 200Å thick Pt electrode. Angle of incidence of 70°.

that the top semi-transparent Pt electrode significantly reduces the sensitivity to changes in the underlying dielectric.

To help alleviate this problem, several oxide electrodes were examined. It was found that $SrRuO_3$ deposited by pulsed laser deposition, was not sufficiently transparent when the electrode was thick enough to allow uniform degradation. As a result, this did not allow SE to resolve changes under the electrode. Indium tin oxide (ITO) was also examined. This material is more transparent than $SrRuO_3$. However, ITO has an electronic transition near 400nm.[32,33] Again, this lowers the sensitivity to changes under the electrode. The resulting sensitivity to reduced layers was approximately the same as with thin platinum (Figure *5–7*).

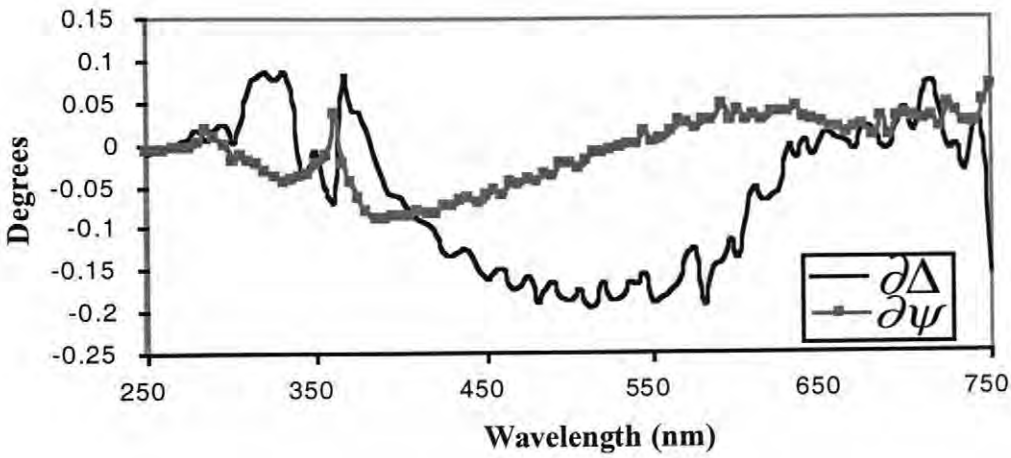

Figure 5–7: Modeled sensitivity of SE to a 100Å reduced layer (constant composition) in barium titanate under a 200Å thick ITO electrode, with an angle of incidence of 70°.

5.2 *Ex-situ* Degradation

To alleviate the problems associated with light absorption in the electrodes, a Cr/Au top electrode was utilized that could be removed for measurements. This allowed for the degradation of the iron doped $SrTiO_3$ sample. Then the electrode was etched away and the surface was examined using SE. Cr was used as a bonding layer because Au would diffuse rapidly at elevated temperatures due to poor adhesion to the oxide surface. The Cr electrodes were deposited by e-beam evaporation with a deposition rate of 1.4Å/sec to a thickness of approximately 100Å and the Au was thermally evaporated at 1.6Å/sec to approximately 1000Å thick. A (approximately 1000Å) Pt bottom electrode was sputtered at 0.05mbar and a current of 63mA. In these experiments the sample was

degraded *ex-situ*. The samples were degraded under a dc field 1.35kV/cm at elevated temperatures (130-150°C) (see Chapter 3 for setup). Then the Au and Cr electrodes were removed using a gold etchant (Transene, Danvers MA) and subsequently a mixture of 6%HNO_3: 16%$(NH_4)_2Ce(NO_3)_6$: 78%H_2O (Transene, Danvers MA) etch to remove the Cr.

With the electrode removed the sample was analyzed. These ellipsometric data were then modeled to determine the surface roughness. It was found that the Cr etchant increased the surface roughness of the samples. Because this has a strong impact on the SE data, the surface roughness was first modeled using a layer of surface roughness over a discrete layer of reduced material on an oxidized bulk. This roughness was further optimized with a model using a concentration gradient from reduced material to an oxidized bulk. The use of both models was necessary because the concentration gradient was strongly correlated to the roughness layer and both could not be varied at the same time. From this modeling the roughness of the sample could be obtained using the reference optical properties for oxidized and reduced iron doped $SrTiO_3$. The etching increased the roughness of the samples from 30-40Å to approximately 100Å in thickness. With the roughness accounted for, the data could be inverted to obtain the actual optical properties of the samples seen in Figure *5–8*.

The experiments reveal changes in the optical properties for degraded samples. For some of the samples (e.g. the times of 45 and 50 min) this data show that the peak in delta is shifted to shorter wavelengths (*Figure 5–8*a). This was reproducible and not a wavelength measurement error. This shift could not be modeled with any combination

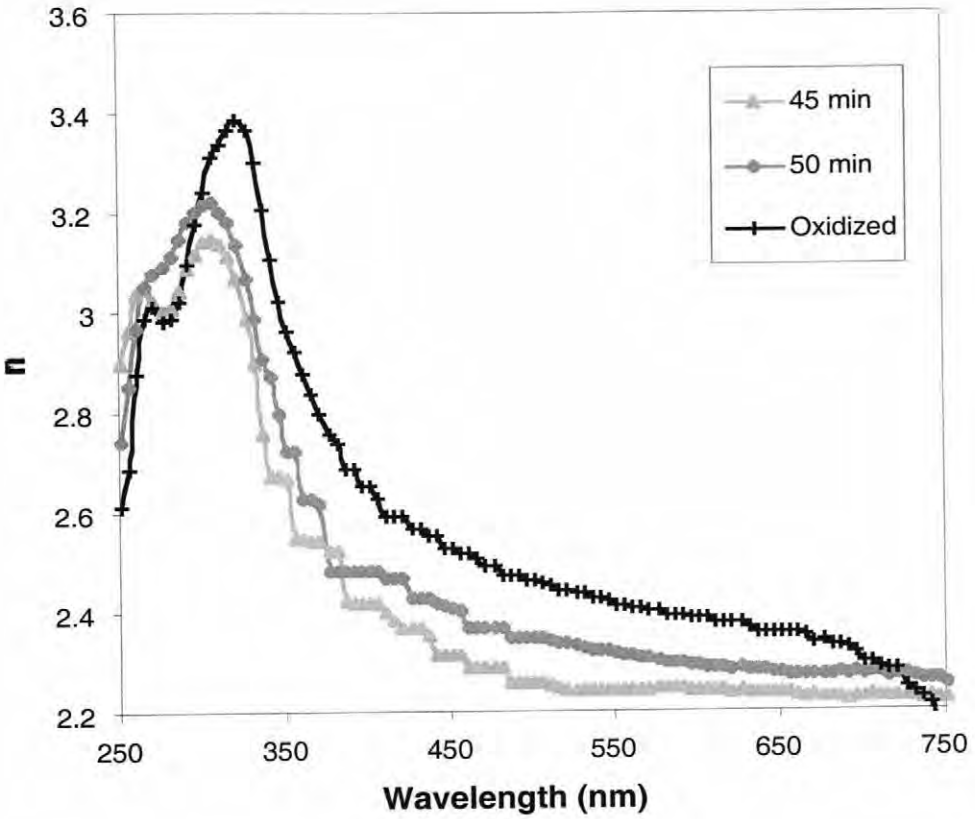
3.6
3.4
3.2
3
2.8
2.6
2.4
2.2
n
250
350
450
550
650
750
Wavelength (nm)
45 min
50 min
Oxidized

a

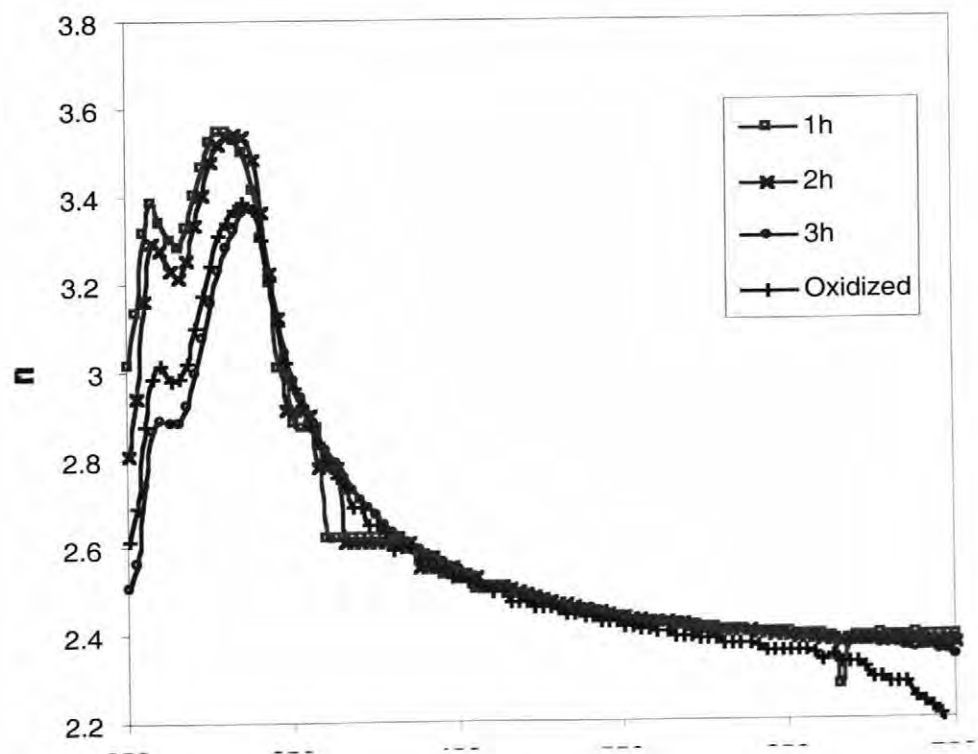
3.8
3.6
3.4
3.2
3
2.8
2.6
2.4
2.2
n
1h
2h
3h
Oxidized

of reduced and oxidized material or surface roughness. This anomaly suggests a surface layer, there is a possibility that it is associated with the chemical changes due to the Cr etchant or with incompletely removed Cr. Alternatively, the shift in the peak position might also be related to changes in the electronic structure of the material. This might be the result of charge injection and creation of a higher conductivity layer in material. In an attempt to describe this, the surface was treated using a Drude model. However, the resulting model did not fit the experimental delta and psi spectra well. The substantial differences at long wavelengths for the shorter times suggests that there are still some residual roughness-induced errors in the determined properties.

For times greater than 1h the peak is not shifted and the optical properties can be modeled as a reduced layer (high $[V_O^{\cdot\cdot}]$) on top of an oxidized layer (low $[V_O^{\cdot\cdot}]$). A concentration gradient of reduced material was used to give the best fit. The data did allow for the extraction of a diffusion depth ($\sqrt{Dt}$) with σ values around 0.02. However, the 90% confidence limits on depth of the concentration gradient were on the order of the diffusion depths themselves. The most probable reason for these large limits is the effect of the surface roughness. The index of refraction change from air to the sample is from 1 to about 2.3-3.4, whereas the maximum index change between the reduced and oxidized state is less than 0.15. There was some surface roughness variation between samples after etching. This change in the surface obscures the relatively small changes due to degradation, leading to large uncertainties in the model *(Table 5–2)*.

There are also uncertainties in the uniformity of the degradation. As mentioned before, the ceramic samples could not be used due to non-uniform degradation. This

Table 5–2: Table of √Dt and associated 90% confidence limits for electrically degraded iron doped $SrTiO_3$.

Time (h)	√Dt (Å)	90% Limit (Å)
0.17	70000	1.16E+04
1.00	177700	9.67E+05
2.00	296300	2.13E+06
3.00	323900	3.28E+06
6.00	917800	1.52E+07

problem was not visible in the single crystal iron doped $SrTiO_3$. To minimize this possibility of non-uniformity, the largest beam size that would fit on the sample was utilized. This served to average the optical properties over several millimeters to avoid local anomalies.

Temporarily ignoring the depth uncertainties, the trend showed by the degraded depths was reasonable. It showed that the damage layer grew with time (*Figure 5–9*). The data showed a near linear increase in the √Dt with a fitted R^2 value of 0.95. Unfortunately, the large uncertainty in the determined depth makes this conclusion suspect. Further information of the diffusion kinetics of the $V_O^{\bullet\bullet}$ was not obtainable with these large uncertainties.

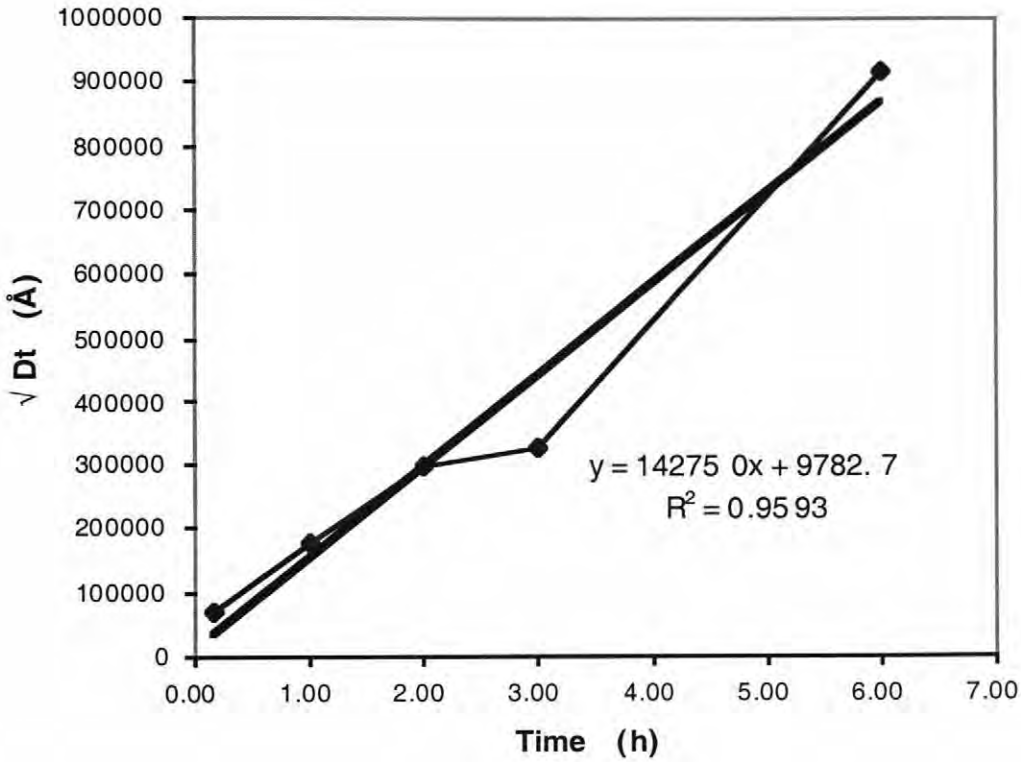

Figure 5–9: Plot of √Dt for iron doped $SrTiO_3$ samples degraded for different times at 150°C under a dc field of 1.35kV/cm, with an angle of incidence of 70°.

Chapter 6

CONCLUSIONS AND FUTURE WORK

6.1 Conclusions

In this work the reference optical properties for several dielectric materials were determined from the near IR to the near UV. With these properties it was possible to determine the sensitivity limits of spectroscopic ellipsometry to the presence of reduced surface layers. The models for iron doped strontium titanate and barium titanate show that the sensitivity of ellipsometry is high enough to distinguish discreet reduced layers on the order of 1 to 4 unit cells thick. These models of the SE data show sensitivities high enough to detect shallow (<<100Å) concentration gradients in ideally smooth iron doped strontium titanate single crystals and polycrystalline barium titanate. This should allow for the observation of field-induced degradation and depth profiling of oxygen vacancy concentration gradients on an angstrom scale. The sensitivity is degraded for rough surfaces.

SE has been used to follow field-induced degradation in iron doped strontium titanate single crystals coated with semi-transparent platinum electrodes. However, it was found that platinum electrodes decrease the sensitivity of SE to degraded layers enough to hamper the determination of a diffusion coefficient. In_2O_3: Sn (ITO) and $SrRuO_3$ are

not appreciably better for SE measurements. The $SrRuO_3$ was not transparent enough in the high sensitivity range when thick enough to provide uniform degradation. ITO has an optical transition near 400nm, close to the maximum sensitivity to reduction in strontium titanate and barium titanate. This reduces the sensitivity dramatically and offers no improvement over Pt electrodes.

Experiments with removable electrodes showed that the oxygen vacancy concentration increased with increasing time under dc electric fields. This was determined by modeling the ellipsometry data. The modeling was hampered by the large uncertainties in the fitted parameters. The 90% confidence limit on the modeled diffusion thickness was on the same order as the thickness itself. This large uncertainty most likely stems from problems with the surface roughness. The index change between air and iron doped strontium titanate was large whereas the difference between the reduced and oxidized strontium titanate was less than 0.15. Thus, small changes in roughness, which occurred on removal of the Cr/Au electrode, causes a much larger change than the degradation. This obscures the changes due to degradation and yields large uncertainty in the models.

6.2 Future Work

There are several areas where further work is suggested. They include continuing work in optical monitoring of field-induced degradation for ferroelectrics, and utilizing real-time spectroscopic ellipsometry to follow oxidation and reduction in perovskites. Two approaches are suggested as possibilities to enable degradation measurements: The

first is to use a large band gap transparent electrode material, such as the delafossites.[35] This will alleviate problems associated with the highly reflective metal electrodes and move the absorption edge to higher energies away from the maximum sensitivity point.

Ex-situ degradation experiments would benefit from electrodes that could be removed with no surface damage to the dielectric. The Cr/Au electrodes used require $(NH_4)_2Ce(NO_3)_6+HNO_3+H_2O$ to remove chrome. This etches the surface of the iron doped strontium titanate samples and increases the roughness. New electrodes should be examined to find ones that are removable without perturbing the surface.

The use of lower temperatures could also be explored. The lower temperatures would increase experiment times appreciably (see Chapter 2.1). Using higher fields might offset this, but care must be taken to ensure the same electronic behavior is present under these higher fields as with the lower fields used in capacitors. If lower temperatures could be employed, electrodes such as indium, that could be removed by heating, liquid electrodes or Ni or Ag paste electrodes that could be removed by acetone could be examined. These all have problems with use at elevated temperatures, but could be removed without affecting the surface if low enough temperatures could be employed.

Use of barium titanate single crystals would increase the sensitivity. These samples should exhibit larger changes due to degradation, as exhibited by the ceramic barium titanate. With these larger changes, the tracking of degradation should be simplified. This could alleviate some of the other problems encountered. These crystals could also be doped to determine the effects of each dopant on the oxygen vacancy

mobility. This might help correlate the properties of the magic dopants to their effects on the oxygen vacancy mobility.

Another route to examine the degradation in these materials is to look at the changes due to the Kerr effect. Potter has measured these electro-optic changes in PZT using ellipsometry.[41] This requires equipment that has been altered to specifically examine these small changes in the optical properties. [41] Through examining the Kerr effect the relative changes in the optical properties could be observed. The correlating field strengths could then be calculated, as done by Gotto for iron doped $BaTiO_3$ using a polarizing microscope.[10] The ellipsometric data could then be modeled to extract the depth profile of the electric field concentration with better depth resolution that is currently available. The index changes due to the electro-optic effects are small and would require an acceptable top electrode.

Spectroscopic ellipsometry could also be used to study degradation in ceramics with instruments that have very good lateral resolution (i.e. a microimaging ellipsometer).[36] This would help with examining the kinetics of production ceramics to help optimize their properties. If very thin ceramics that were only two grains thick were examined, then the evolution of the oxygen vacancy profiles across grain boundaries could be investigated. This information would be useful in determining the rate limiting step and role of grains in the degradation process.

Real-time SE could also be used to follow the oxidation and reduction of dielectric materials. These can be examined using a controlled atmospheric chamber on an ellipsometer. The evolution of the oxygen vacancy concentration profiles during

reoxidation is important for capacitor manufacturers where reoxidation is necessary for sintering with base metal parts. From this information the kinetics of oxygen incorporation into the materials and reduction of the material could be determined. The source of the different activation energies for oxidation and reduction could also be examined. This kinetic data is not currently available and will allow for better understanding and optimization of the reoxidation treatment.

The oxidation and reduction reactions at interfacial layers between metals and films can also be examined. There is still some doubt as to when, or even if, base metal electrodes in MLC are oxidized during the reoxidation process.[2,8,9,37] With ellipsometry the information on any interfacial layers during the reoxidation process can be obtained. This is not easily done with other techniques due to the destructive sample preparation or knock in problems incurred during measurements, such as Transmission Electron Microscopy and Secondary Ion Mass Spectroscopy. This information can be used to obtain the kinetics of the interfacial reaction by looking at the growth of this interface in real time. These data can be utilized to optimize the metal/film during the reoxidation process.

The electrode interfaces in thin film dielectrics, such as barium strontium titanate, have also been a problem with degradation. An interfacial area has been reported to exist where degradation begins.[38] This is usually the bottom layer and has been explained by the increased stresses at the interface between the bottom electrode and film.[39] The interfaces could be examined using ellipsometry to examine the characteristics of this layer. A concentration profile of the oxygen vacancies should show an enhanced

diffusion rate near this interface if there is a large effect of the stress from the lattice mismatch. If there is an interface layer with different optical properties it should also be detected and could be modeled using ellipsometric data.

Similar experiments could be performed to examine the interface between oxide electrodes and films. The oxide electrodes often have defects, including oxygen vacancies.[33] It is possible for these defects to migrate into the dielectric materials. These could be examined using spectroscopic ellipsometry. The evolution of the reduced layers at the interface could be examined. If this information was compared to similar experiments with non-oxide electrodes, the effects of diffusion of the oxygen vacancies on degradation could be determined. If these interfacial layers exist their growth could also be monitored to extract kinetic data on the growth.

The source of coloration in the $BaTiO_3$ and iron doped $SrFeO_3$ has not been verified. It seems clear from several sources that the coloration is linked to the oxygen vacancy front. [1,2,4,5,7,8,10,12,21,22,23] However, the exact manner in which this occurs has not be determined experimentally. The blue coloration in $BaTiO_3$ seem to be due to the ionization of Ti^{4+} atom to Ti^{3+}.[1,4,7,8,21] The red-brown to clear coloration change in iron doped material has also be explained as a change from Fe^{4+} to Fe^{3+}.[2,4,5,10,12,21,22,23] This needs to been examined using Electron Spin Resonance or Mossbauer Spectroscopy to look at the changes associated with the degradation. These data could be used in conjunction with crystal field theory to determine the source of the coloration.

REFERENCES

1. K. Lehovec and G.A. Shrine, "Conductivity Injection and Extraction in Polycrystalline Barium Titanate," J. Appl. Phys. 33 2035-2044 (1962).

2. R. Waser, T. Baiatu, and K. Hardtl, "DC Electrical Degradation of Perovskite-Type Titanates: I, Ceramics," J. Am. Ceram. Soc., 73 (6) 1645-1653, (1990).

3. A.J. Moulson and J.M. Herbert, Electroceramics: Materials, Properties, Applications, Chapman Hall, London, 1995.

4. D. Anderson, "Electrical Resistance Degradation in Barium Titanate Dielectrics," Ph.D. Thesis, Pennsylvania State University, 1988.

5. J. Sheng, T. Fukami, and J. Karawawa, "Direct Current Electrical Degradation of Iron Doped Titania Ceramics" J. Mat. Res. 13 (7), 1761-1764, 1998.

6. D.D. Glower and R.C. Heckman, "Conduction-Ionic or Electronic- in Doped $BaTiO_3$," J. Chem. Phys 41, 877-879 (1964).

7. C Schaffrin, "Oxygen Diffusion in $BaTiO_3$ Ceramics," Phys. Stat. Solidi 35, 79-88 (1976)

8. W.R. Buessem, R.M Gruver, C.W. Dickey, et al., Linden Laboratories Inc., Third Quarterly report, Contract No. DA-36-039 AMC-00107E, Continuation of DA-36-039 SX-78912, Feb 15, 1963-May 15 1963, to U.S. Army Corps. Engr. Labs, Fort Monmouth, N.J. report No. 19, Sept 15 1963.

9. W.R. Buessem, R.M Gruver, C.W. Dickey, et al., Linden Laboratories Inc., Report No., Contract No. Da36039 AMC-00107 (E), Continuation of DA-36039 SC78912, Aug. 15, 163 Jan15 1964, to U.S. Army Signal Corps Eng. Labs. Fort Monmouth, NJ, Report No. 20 Feb 15 1964.

10. Y.Gotto and S. Kachi, "Studies on the Mechanism of Electronic Conduction in Fe-Doped $BaTiO_3$ Single Crystals by Applying Kerr Effect," J. Phys. Chem. Solids 32, 889-895 (1971).

11. S. Triebwasser, "Space Charge Fields in $BaTiO_3$," Phys. Review. 118, 100-105 (1960).

12. R. Waser, T. Baiatu, and K. Hardtl, "DC Electrical Degradation of Perovskite-Type Titanates: II, Single Crystals," J. Am. Ceram. Soc., 73 (6) 1654-1662 (1990).

13. T. Baiatu, R. Waser, and K. Hardtl, "DC Electrical Degradation of Perovskite-Type Titanates: III, A Model of the Mechanism" J. Am. Ceram. Soc., 73 (6) 1663-1671, (1990).

14. J. Nowotny and M. Rekas "Defect Chemistry of $BaTiO_3$," Sol. State Ionics 49 135-154 (1991).

15. N.H. Chan, R.K Sharma and D.M. Smyth, "Nonstoichiometry in Undoped $BaTiO_3$" J. Am. Ceram. Soc., 64 556-562 (1981).

16. S.A. Long and R.N. Bluementhal "Ti-Rich Nonstoichiometric $BaTiO_3$: II, Analysis of Defect Structure," J. Am. Ceram. Soc. 54 577-583 (1971).

17. Y. Tsur and C.A. Randall, "Defect Chemistry of $BaTiO_3$ for Base Metal Electrode Capacitors," Talk at Center for Dielectric Studies Meeting, Fall 1999, University Park Pa.

18. G.A. Cox and R.H. Tredgold, "Time Dependence of the Electrical Conductivity in Strontium Titanate Single Crystals," Brit. J. Appl Phys, 16, 427-430 (1665).

19. G.A. Cox and R.H. Tredgold, "On the Electrical Conductivity of Calcium Titanate Crystals," Brit. J. Appl Phys, 18, 37-40 (1967).

20. J.F. Scott, "Dielectric-Breakdown in High-Epsilon Films for ULSI DRAMS: Leakage Current Precursors and Electrodes," Int. Ferro, 9, 1-12 (1995).

21. J. Blanc and D.L. Staebler, "Electrocoloration in $SrTiO_3$: Vacancy Drift and Oxidation-Reduction of Transition Metals," Phys Rev. B 4, 3548-3557 (1971).

22. J.B. MacChesney, R.C. Sherwood, J.F. Potter "Electric and Magnetic Properties of the Strontium Ferrates," J. Chem. Phys, 43 (6) 1907-1913 (1965).

23. V.T. Kunin, A.N. Tsikin and N.A. Shturbina, " Variation of Electrical Conductivity and of Color in $SrTiO_3$ Single Crystals in a Constant Electrical Field," Sov. Phys. Solid State, 11, 598-599 (1969).

24. L. Benguigui, "Electrical Phenomena in Barium Titanate Ceramics," J. Phys Chem Solids, 34, 427-430 (1965).

25. F.A. Kroger and H.J. Vink, Solid State Physics Vol 3, edited by F. Seitz and D. Trunbull, Academics Press, New York, 307-435 (1956).

26. D.M. Smyth, "Thermodynamic Characterization of Ternary Compound. I. The Case of Negligible Defect Association," J. Solid State Chem. 16,. 81-83 (1976).

27. B. J. Gibbons, "Real-Time Spectroscopic Ellipsometry and its Application to the Processing of $YBa_2Cu_3O_{7-\partial}$ Films by Molecular Beam Epitaxy," Ph.D. Thesis, Pennsylvania State University, 1998.

28. P. Chindaudom and K. Vedam, "Optical Characterization of Inhomogeneous Transparent Films on Transparent Substrates by Spectroscopic Ellipsometry," Optical Characterization of Real Surfaces and Films ed. M.H. Francombe and J.L. Vossen, Academic Press San Diego, 43-52 1994.

29. H. Thompkins, A User's Guide to Ellipsometry, Academic Press Inc. San Diego, 1993.

30. I. An, "Development of Real-time Spectroscopic Ellipsometry and its Application to the Growth and Modification of Amorphous Silicon Thin Films," Ph.D. thesis, The Pennsylvania State University, 1992.

31. B. Hong, "Development of Real Time Spectroscopic Ellipsometry and its Application to the Growth of Diamond Thin Films by Microwave Plasma-Enhanced Chemical Vapor Deposition," Ph.D. thesis, The Pennsylvania State University, 1996.

32. D.E. Aspnes, "Spectroscopic Ellipsometry of Solids," in Optical Properties of Solids, New Developments, edited by B.O. Seraphin (North-Holland Publishing Company, Amsterdam, NL, 1976), 799.

33. J.M.M. DeNijs, A.H.M. Holtslag, A. Hoeksta and A. Van Silfhout, "Calibration Methods for Rotating-Analyzer Ellipsometer," J. Opt. Soc. of Am. A, 5 (6), 1466 (1988).

34. J. Koh, "The Sensitivity Limits of Spectroscopic Ellipsometry for the Characterization of the Optical Properties," M.S. thesis, The Pennsylvania State University, 1995.

35. M. DiDomenico, Jr. And S.H. Wemple, "Optical Properties of Perovskite Oxides in their Paraelectric and Ferroelectric Phases," Phys. Rev. 166 (2) 565-576 (1968).

36. M. Cardona, "Optical Properties and Band Structure of $SrTiO_3$ and $BaTiO_3$," Phys Rev., 140 A651-A655 (1965).

37. K.S. Ramaiah, V.S.Raja, A.K. Bhatnagar, R.D. Tomlinson, R.D. Pilkington, A.E. Hill, S.J. Chang, Y.K. Su, and F.S. Juang, "Optical Structure and Electrical

Properties of Tin Doped Indium Oxide Thin Film Prepared by Spray-Pyrolysis Technique," Semicond. Sci. Technol., 15 676-683 (2000).

38. B. Bessais, H. Ezzaouia and R. Bennaceur, "Electrical Behavior and Optical Properties of Screen-Printed ITO Thin Films," Semicond. Sci. Technol. 8 1671-1678 (1993).

39. T. Otabe, K. Ueda, A. Kudoh, H. Hosono, and H. Kawazoe, "n-type Electrical Conduction in Transparent Thin Films of Delafossite-Type $AgInO_2$," Appl. Phys Lett 72 (9): 1036-1038 (1998).

40. D. Beaglehole, "Performance of a Microscopic Imaging Ellipsometer" Rev. Sci. Inst. 59 (12) 2557-2559 (1988).

41. B.G. Potter, D. Dimos, M.B. Sinclaire and S. Lockwood "Evaluation of Electro-Optic Phenomena in Ferroelectric Thin Flims Using Ellipsometric Techniques," Integr. Ferro. 11 (1-4) 59-68 (1995).

42. R. Ueyama, N. Seki, K. Kamada, M. Harada, and T. Ueyama, "Preparation and Evaluation of Highly Monodispersed Ni Powders for Base Metal Internal Electrode of Multilayer Ceramic Devices" J. Cer. Soc Jap. 107 (7) 652-656 (1999).

43. J.C. Shin, J. Park, C.S. Hwang and H.J. Kim, "Dielectric and Electrical Properties of Sputter Grown (Ba, Sr)TiO_3 Thin Films," J. Appl. Phy, 86 (1) 506-513 (1999).

44. F. Yan, P. Bao, X.B. Chen, J.S. Zhu and Y.N Wang, "The Resistance Degradation of ($Ba_{0.5}$, $Sr_{0.5}$)TiO_3 Thin Films," Integr. Ferro., 33 379-388 (2001).